An Observational Study of Molecular Clouds at High Galactic Latitude

高銀緯領域における分子雲の観測的研究

山本 宏昭

名古屋大学
大学院理学研究科
素粒子宇宙物理学専攻

2005 June

An Observational Study of Molecular Clouds at High Galactic Latitude

Hiroaki Yamamoto

Department of Astrophysics
Nagoya University

2005 June

Acknowledgments

First of all, I would like to express my hearty thanks to Yasuo Fukui, my supervisor, for his invaluable comments on this work. I appreciate his great encouragement in various aspects during my research.

I would like to acknowledge Hideo Ogawa, Akira Mizuno, Toshikazu Onishi, Yoshinori Yonekura, Norikazu Mizuno and developers of the NANTEN telescope. Their excellent efforts on constructing the best SIS receivers and the NANTEN telescope and maintaining those made observations efficiently.

I would like to express my gratitude to all the member of the laboratory for a kind help in various aspects; Akiko Kawamura, Yoshiaki Moriguchi, Masanori Nakagawa, Hiroshi Sasago, Tetsuhiro Minamidani, Kentaro Yamaoka, Shingo Ito, Naoya Ohmuro, Tomotake Takeuchi, Akiko Hayashi, Tokuichi Kawase, Takenori Sueoka, Hidetaka Sugiyama Kazushi Torii, Motosuji Fujishita, Atsushi Higuchi, Yoji Mizuno, Joanne Dawson, Hinako Iritani, Yoichiro Uto, Maikeru Kawase, Natsuko Kudo and Yosuke Miyamoto. I acknowledge Reiko Abe, Nami Higuchi, Manami Izuhara, and Asako Kato for their encouragement in various aspects.

I greatly appreciate the hospitality of all the staff members of LCO of the Carnegie Institution of Washington. The NANTEN projects is based on a mutual agreement between Nagoya University and the Carnegie Institution of Washington. I acknowledge many Japanese public donors and companies who contributed to the realization of this projects. This work was financially supported in part by Grants-in-Aid for Scientific Research from the Ministry of Education, Science, Sports, and Culture of Japan. I am financially supported by Japan Society for Promotion of Science.

Finally, I thank all my friends and family for helping and encouraging me in various aspects throughout my research and life.

Abstract

We have carried out the high Galactic molecular clouds observations with the NANTEN telescope in order to reveal the distribution and physical properties of molecular clouds at high Galactic latitude. The three types of an observation have been executed at high Galactic region.

Firstly, a survey for high Galactic latitude molecular clouds was carried out toward the 68 of far-infrared-excess clouds of Reach et al. (1998) by using ^{12}CO (J=1–0) line. CO emission was detected from 32 infrared excess clouds, corresponding to the detection rate of 47%. The CO detection rates for the cold and warm infrared excess cloud whose dust temperature are lower and higher than 17 K is 72% and 33%, respectively. This indicates that the cold clouds are well shielded from external UV radiation, resulting in a high CO abundance and a low temperature of the clouds. The infrared-excess clouds with no CO emission are most likely to be molecular hydrogen clouds because the temperature is similar to, or lower than, that of the surrounding H I gas. The molecular gas without CO emission seems to occupy more than 90% of the area of the infrared-excess clouds.

Next, we carried out a CO survey of high Galactic latitude molecular clouds toward an H I filament including MBM 53, 54, and 55. We covered the whole area of the H I filament in ^{12}CO (J=1–0) with a 4′ grid spacing. The filament consists of many clumpy molecular clouds. 110 ^{12}CO clouds are identified and total mass is estimated to be $\sim 1200 M_{\odot}$. ^{13}CO (J=1–0) observations were carried out toward the region of high ^{12}CO intensities in order to measure the optical depth of molecular gas. There is no detection in C^{18}O (J=1–0) line in the observed region. This indicates that there are no clouds dense enough to lead star-formation in the near future. These observations spatially resolved the entire gas distribution of MBM 53, 54, and 55 for the first time, and we have found a massive cloud, HLCG 92−35 whose mass is $\sim 330\ M_{\odot}$, corresponding to 1/4 of the total mass. This CO cloud occupies the Galactic western half of a circular H I cloud toward (l, b) $\sim$ (92°, −35°), and the H I to CO mass ratio is estimated to be the largest in the observed region. Far-infrared-excess clouds toward HLCG 92−35 are the largest in the observed region. The ratio of the luminosity of the infrared excess to CO mass is also significantly larger than those of the other clouds, by a factor of $\sim$5. These facts indicate that HLCG 92−35 is a CO-forming molecular cloud, which is younger than the MBM clouds in terms of molecular cloud formation. Some past explosive event has been suggested by Gir et al. (1994) toward the H I filament. Toward HLCG 92−35, the molecular gas distributed along the western edge of the H I cloud, which implies that

the molecular gas may be formed by a compression of expanding H I shell.

Finally, we carried out large scale CO observations toward a loop-like structure in far infrared whose angular extent is about 20×20 degrees around (l, b) ∼ (109°, −45°) in Pegasus whose diameter corresponds to ∼26 pc at a distance of 100 pc, the same as that of a star HD886 (B2IV) at the center of the loop. We covered the loop-like structure in the ^{12}CO (J=1–0) emission at 4′–8′ grid spacing and in the ^{13}CO (J=1–0) emission at 2′ grid spacing for the ^{12}CO emitting regions. The ^{12}CO distribution is found to consist of 78 small clumpy clouds whose mass ranges from 0.04 $M_{\odot}$ to 11 $M_{\odot}$. Interestingly, about 83% of the ^{12}CO clouds have very small masses less than 1.0 $M_{\odot}$. ^{13}CO observations revealed that 19 of the 78 ^{12}CO clouds show significant ^{13}CO emission. ^{13}CO emission was detected the region where the molecular column density of ^{12}CO clouds is greater than 5×10^{20} cm^{-2}, corresponding to Av of ∼1 mag. We find no indication of star formation in these clouds in IRAS Point Source Catalog and 2MASS Point Source Catalog. The very low mass clouds identified are unusual in the sense that they have very weak ^{12}CO Tpeak of 0.5 K–2.7 K and that they aggregate in a region of a few pc with no main massive clouds; contrarily to this, similar low mass clouds less than 1 $M_{\odot}$ are seen in the other regions previously observed including high Galactic latitude are all associated with more massive main clouds of ∼100 $M_{\odot}$. A comparison with a theoretical work on molecular cloud formation (Koyama & Inutsuka 2002) suggests that the very small clouds may have been formed in the shocked layer through the thermal instability. The star HD886 (B2IV) may be the source of the mechanical luminosity via stellar winds to create shocks, forming the loop-like structure where the very small clouds are embedded.

Contents

Chapter 1

Introduction

1.1 Molecular Clouds in the Interstellar Medium

The interstellar medium mostly consists of atomic and molecular hydrogen (hereafter H I and H_2). Since the 21cm line of H I was discovered (Ewen & Purcell 1951; Muller & Oort 1951; Pawsey 1951), it has been used for years to study the distribution and kinematics of interstellar clouds (e.g., Heiles 1979; Hartmman & Burton 1997). On the other hand, molecular clouds in interstellar space mostly consist of H_2. But H_2 can not be directory observed because it has no permanent electric dipole moment and dose not radiative at useful wavelength and intensity. In order to search for molecular clouds, the radiation of $^{12}C^{16}O$ (hereafter ^{12}CO) molecules and their isotopes at radio wavelengths has been generally used. CO molecules are the most suitable tracer of H_2 from follwing regions, 1) they have a permanent electric dipole moment, 2) they are the second abundant molecules in the interstellar medium and 3) they relatively stable compared with other molecules. ^{12}CO (J=1–0) traces H_2 whose density is greater than $\sim 10^2$ cm^{-3} and has been used to search for diffuse molecular clouds. ^{12}CO has also been used to investigate the large scale distribution of molecular clouds in the Milky way (Dame et al. 2001; Solomon et al. 1987; Matsunaga et al. 2001). Dame et al. (2001) revealed the whole distribution and kinetics of molecular clouds around the Galactic plane ($|b| \leq 10°$) in the Milky way with two 1.2 m telescopes. $^{13}C^{16}O$ (hereafter ^{13}CO)(J=1–0) and $^{12}C^{18}O$ (hereafter $C^{18}O$)(J=1–0) trace higher density regions of molecular clouds than ^{12}CO. $C^{18}O$ has been generally used to search for the dense molecular clouds which appear to be forming proto-stars (e.g., Onishi et al. 1998, 1999; Mizuno et al. 1999; Hara et

al. 1999; Tachihara et al. 2000). Most astronomical phenomena such as H II regions or supernovae, occur within the Galactic plane and molecular clouds are greatly affected by those phenomena. For these reasons, many molecular observations have been performed toward near-by star forming regions and/or low Galactic latitudes where the Galactic plane is covered.

1.2 Introduction to High Galactic Latitude Region

Generally speaking, The region at $|b| \gtrsim 20°$ is known as the high Galactic latitude region. This region covers ~66% of the whole sky and it is ~7.6 times larger than the region of Galactic plane ($|b| \lesssim 5°$). Since the gaussian scale height of molecular clouds is estimated to be ~100 pc (Magnani et al. 2000), astronomical objects at high Galactic latitude should be close to the Sun. The possibility of overlapping with other objects along the line of sight is low. Molecular clouds at high Galactic latitude (hereafter HLCs) have a lower density compared with dark clouds where the optical obscuration is significantly large and they are often called translucent clouds or diffuse clouds (e.g., van Dishoeck & Black 1988). Therefore some HLCs are considered to be the transition phase from atomic to molecular gas. Most HLCs are not sites of active star formation, although a few of them contain T-Tauri stars (e.g., Magnani et al. 1995; Pound 1996; Hearty et al. 1999). Since HLCs are far from far-UV sources, most of them are probably exposed to the average interstellar far-UV field stars (see van Dishoeck & Black 1988; Draine 1978).

1.3 Past Observations and Studies at High Galactic Latitude

Given the very small distance of HLCs, it is a challenging task for observers to make a complete survey for HLCs over a large portion of the sky. ^{12}CO(J=1–0) emission has been used to search for HLCs because its line emission is strongest among the thermally or sub-thermally excited mm lines of interstellar molecular species. It is, however, difficult to cover the large area subtended by some HLCs as large as tens square degrees with existing mm-wave telescopes in a reasonable time scale because of the general weakness of the ^{12}CO emission, typically $\sim$ a few

K. HLCs have therefore been searched for by utilizing various datasets at other wavelengths. Pioneering works on HLCs were performed by Blitz et al. (1984) and Magnani et al. (1985). They selected their targets by looking for apparent optical obscuration on the Palomar Observatory Sky Survey (POSS) prints and the Whiteoak extension to the POSS. They detected 57 molecular clouds in 35 complexes at $|b| \geq 25°$. They found that these clouds show weak CO emission (typically a few K) and that they do not seem to be gravitationary bound. From their cloud to cloud velocity dispersion, they summarized that these molecular clouds are within 100 pc of the Sun. Keto & Myers (1986) performed CO observations toward faint obscuration or reflection by using one hundred and fifty one prints from the European Southern Observatory (ESO) sky survey. They suggested that HLCs have a mass at least 10 times less than that needed to bind them by self-gravity. Far-infrared data have also been used as a probe for molecular gas, and there have been observations toward infrared clouds, some of which are probably candidates for molecular clouds (e.g., Reach, Koo, & Heiles 1994). Far-infrared excess over H I (Blitz et al. 1990) can be used as an another probe. Blitz et al. (1990) detected ^{12}CO toward only 13% of the sample. Magnani et al. (1996) summarized the surveys of HLCs and have catalogued more than 100 objects as of this moment. As another approach for searching for HLCs, an unbiased survey in ^{12}CO (J=1–0) at high Galactic latitude has been performed by Hartmann et al. (1998) in the northern Galactic hemisphere and Magnani et al. (2000) in the southern Galactic hemisphere. These observations were carried out using the 1.2 m millimeter-wave telescope at Cambridge, MA, where they observed the whole area above $|30°|$ in elevation from the telescope with a locally Cartesian grid of 1°, resulting in a small sampling factor of a few %. In Magnani et al. (2000), if all of the clouds in Magnani et al. (1996) within the bounds of the surveyed region are included, then 26 of 41 clouds were detected for a detection ratio of 0.63. Bhatt (2000) summarized above two survey results. These surveys of HLCs show that the distribution of HLCs is not uniform at high Galactic latitude, and there are some groups or complexes of HLCs, whose angular extent is $\sim$10 degrees or larger. The past observations of such complexes of HLCs with high angular resolution have been limited to a few regions including the Polaris flare (Heithausen & Thaddeus 1990) and the Ursa Major (Pound & Goodman 1997). Pound & Goodman (1997) showed the arc-like structure of the molecular cloud system and they suggested that the origin of such structures could be some explosive events.

Observations with high resolution have been also performed toward some already known HLCs (e.g., Pound et al. 1990). Observations of high J transitions of CO have been performed toward some HLCs (e.g., Falgarone et al. 1998; Ingalls et al.

2000) and observations of C I ($^3P_1$–$^3P_0$) have also been performed toward some HLCs (e.g., Ingalls et al. 1997; Stark & van Dishoeck 1994; Bensch et al. 2003). Ingalls et al. (2000) found that from observations of J=4–3, 3–2, 2–1 and 1–0 transitions of CO, the CO gas temperature must not be greater than 30 K and the most probable solution of an LVG model is a high-density and low-temperature (HDLT) solution, with volume density of $10^{4.5\pm0.5}$ cm^{-3} and kinetic temperature of $\approx$ 8 K. Reach et al. (1995) observed J=3–2, 2–1 and 1–0 transitions of CS, and the J=1–0 transitions of HCO^+ and HCN toward some dense HLCs. The CH observations of the $2\Pi_{1/2}$ F=1–1 hyperfine transition have been performed toward MBM 16 and 40 by Magnani et al. (1998).

Other wave length observations have also been performed at high Galactic latitude. IRAS Sky Survey Atlas (ISSA) covered the whole high Galactic latitude region. Cleary, Heiles & Haslam (1979) revealed the HI distribution at $\delta \leq -30°$ and Hartmann & Burton (1997) revealed it of the entire sky accessible from Dwingeloo radio telescope of the Netherlands Foundation for Research in Astronomy. Schlegel et al. (1998) created reprocessed 100 μm maps of the whole sky using the COBE/DIRBE and IRAS/ISSA maps and removing the zodiacal foreground and confined point sources. The distribution of far-infrared excess over H I, which is a good index of molecular hydrogen, toward a fair region of the whole sky was revealed by Reach et al. (1998). These results suggest that the distribution of dust, H I and H_2 are not also uniform around the Sun and there are some large filamentary or loop-like structures which may be undergoing the effect of the past and/or present activities of astronomical objects.

Boulanger et al. (1996) correlated the far-infrared emission with H I at high Galactic latitude. They found that there is a good correlation between far-infrared emission and H I at all wavelengths from 100 μm to 1 mm for H I column densities smaller than 5×10^{20} cm^{-2}. Their data is well fitted by a single Plank curve of T=17.5 K, indicating that there is no colder component of significance on large angular scales.

1.4 The Aim of This Study and The NANTEN Telescope

Under circumstances in Section 1.3, we have carried out observations at high

Galactic latitude. In spite of the existence of several large angular scale structures in H I and far infrared radiation, molecular observations have been covered toward only two of them (for details, see previous subsection). In order to better understand the structure of HLCs and to pursue the evolution of HLC complexes, CO observations covering tens of square degrees at a high angular resolution are crucial. In addition, It is likely that a large number of HLCs have not yet been detected in CO. Actually, Reach et al. (1998) identified good candicates for molecular clouds and more than a half of them have not been observed in a tracer of molecular clouds. Therefore, we have observed these objects with the NANTEN telescope. The aim of our study is to reveal the distribution and physical properties of HLCs, and to reveal observationally the mechanism of molecular cloud formation.

Figure 1–1 shows a photograph of the NANTEN telescope at Las Campanas Observatory (LCO), Chile. This telescope has observed the LMC, SMC, Galactic plane, many star-forming regions and so on from LCO since 1996 under a mutual agreement between Nagoya University and the Carnegie Institution of Washington. The results from NANTEN have been published in NANTEN special issues of Publications of the Astronomical Society of Japan (PASJ Vol. 51, No.6, 1999 and Vol. 53, No.6, 2001) and in some foreign journals such as Astrophysical Journal, and have been presented at many astronomical conferences.

The parameters of the NANTEN telescope are summarized in Table 1–1. The primary mirror has a diameter of 4 m and the surface accuracy is $\lesssim$ 50 μm. The high accuracy is maintained even in the daytime owing to the low thermal expansion coefficient of the material, CFRP (Carbon Fiber Reinforced Plastic) (Fukui & Sakakibara 1992). It has a beam size of 2'.6 at a frequency of ^{12}CO (J=1–0) emission, 115.271 GHz, corresponding to $\sim$0.08 pc at a distance of 100 pc, a typical distance to HLCs. The receiver front-end is a 4 K cooled Nb Superconductor Insulator Superconductor (SIS) tunnel junction mixer receiver which was developed at the Department of Astrophysics, Nagoya University (Ogawa et al. 1990). The receiver exhibits a best noise temperature of less than 100 K in a single side band at 85–115 GHz. The system noise temperature, including the sky toward the zenith, is $\sim$120 K at 85–110 GHz and $\sim$240 K at 115 GHz. For the backend, there are two acousto-optical spectrometers (AOS) with 2048 channels. One covers a wide band ($\sim$250 MHz, corresponding to a velocity coverage of $\sim$650 km s^{-1}) and the other covers a narrow band ($\sim$40 MHz, corresponding to that of $\sim$100 km s^{-1}). The pointing accuracy was measured to be better than $\sim$ 20″, as checked by optical observations with a CCD camera attached to the telescope as well as by radio observations of Jupiter, Venus, and the edge of the Sun. All operation and reduction software has

been developed by members of our laboratory.

1.5 Contents of This Thesis

In order to reveal the distribution of molecular clouds at high Galactic latitude, we carried out the three types of observation at high Galactic latitude regions. Results of these observations are shown in chapters 2 to 4 of this dissertation.

In chapter 2, the results of observations of the J=1–0 transition of ^{12}CO in the far infrared excess clouds, which were cataloged by Reach et al. (1998), survey are presented. Figure 1–2 shows the distribution of the far infrared excess clouds. In order to reveal the relation between those clouds and the molecular clouds, we carried out observations of all far infrared excess clouds (filled circles in Figure 1–2) accessable from NANTEN telescope in ^{12}CO.

There are two large scale structures within the dotted line in Figure 1–2. Figure 1–3 shows a large scale map of 100 μm derived by Schlegel et al. (1998) toward the dotted line in Figure 1–2. In chapter 3, the results of the observations of the molecular cloud complex including MBM 53, 54, and 55, which is the large structure on the righthand side of Figure 1–3, made in the J=1–0 transition of ^{12}CO, ^{13}CO and C^{18}O are presented. Toward MBM 53, 54 and 55, there is a large H I filament which may be expanding, as seen from the position-velocity map of H I (Gir et al. 1994). Martin & Kun (1996) and Li et al. (2000) confirmed the existance of T-tauri stars in the H I filament. In order to reveal the overall distribution and physical properties of molecular clouds associated with the H I filament, we carried out the observations toward the whole H I filament in ^{12}CO, ^{13}CO and C^{18}O. In chapter 4, the results of the observations of the molecular clouds toward a large loop-like structure in Pegasus (the large structure of left side in Figure 1–3) made in the J=1–0 transition of ^{12}CO and ^{13}CO are presented. There is one of large loop-like structures shown in far infrared and H I in Pegasus. In order to reveal the overall distribution and physical properties of molecular clouds associated with the loop-like structure and the effect of the external environment on the molecular clouds, we carried out observations of the whole loop-like structure in ^{12}CO and ^{13}CO.

Finally, we summarize the main findings of the present study, and remaining questions and future prospects in Chapter 5.

References

Bhatt, H. C. 2000, A&A, 362, 715

Bensch, F., Leuenhagen, U., Stutzki, J., & Schieder, R. 2003, ApJ, 591,1013

Blitz, L., Bazell, D., & Desert, F. X. 1990, ApJ, 352, 13

Boulanger, F. Abergel, A. Bernard, J. P., Burton, W. B., Désert, F. X., Hartmann, D., Lagache, G., & Puget, J. L. 1996, ApJ, 312, 256

Dame, T. M., Hartmann, D., & Thaddeus, P. 2001, ApJ, 547, 792

Draine, B. T. 1978, ApJS, 36, 595

Ewen, H. I., & Purcell, E. M. 1951, Nature, 168, 356

Falgarone, E., Panis, J. F., Heithausen, A., Perault, M., Stutzki, J., Puget, J. L., & Bensch, F. 1998, A&A, 331, 669

Fukui, Y., & Sakakibara, O. 1992, Mitsubishi Electric Advance, 60, 11

Gir, B. Y., Blitz, L., & Magnani, L. 1994, ApJ, 434, 162

Hara, A., Tachihara, K., Mizuno, A., Onishi, T., Kawamura, A., Obayashi, A., & Fukui, Y. 1999, PASJ, 51, 895

Hartmann, D., & Burton, W. B. 1997, Atlas of Galactic Neutral Hydrogen (Cambridge: Cambridge Univ. Press)

Hartmann, D., Magnani, L., & Thaddeus, P. 1998, ApJ, 492, 205

Hearty, T., Magnani, L., Caillault, J, P. 1999, A&A, 341, 163

Heiles, C. 1979, ApJ, 229, 533

Ingalls, J. G., Chamberlin, R. A., Bania, T. M., Jackson, J. M., Lane, A. P., & Stark, A. A. 1997, ApJ, 479, 296

Ingalls, J. G., Bania, T. M., Lane, A. P., Rumitz, M., & Stark, A. A. 2000, ApJ, 535, 211

Keto, E. R., & Myers, P. C. 1986, ApJ, 304, 466

Li, J. Z., Hu, J. Y., & Chen, W. P. 2000, A&A, 356, 157

Magnani, L., Blitz, L., & Mundy, L. 1985, ApJ, 295, 402 (MBM)

Magnani, L., Caillault, J. P., Buchalter, A., & Beichman, C. A. 1995, ApJS, 96, 159

Magnani, L., Hartmann, D., & Speck, B, G. 1996, ApJS, 106, 447

Magnani, L., Onello, J. S., Adams, N. G., Hartmann, D., & Thaddeus, P. 1998, ApJ, 504, 290

Magnani, L., Hartmann, D., Holcomb, S. L., Smith, L. E., & Thaddeus, P. 2000, ApJ, 535, 167

Martin, E. L., & Kun, M. 1996, A&AS, 116, 467

Matsunaga, K., Mizuno, N., Moriguchi, Y., Onishi, T., Mizuno, A., & Fukui, Y. 2001, PASJ, 53, 1003

Mizuno, A., Hayakawa, T., Tachihara, K., Onishi, T., Yonekura, Y., Yamaguch, N., Kato, S., Hara, A., Mizuno, N., Kawamura, A., Abe, R., Saito, H., Yamaguchi, R., Ogawa, H., & Fukui, Y. 1999, PASJ, 51, 859

Muller, C. A., & Oort, J. H. 1951, Nature, 168, 357

Ogawa, H., Mizuno, A., Hoko, H., & Fukui, Y. 1990, Int. J. Infrared Millimeter Waves, 11, 717

Onishi, T., Mizuno, A., Kawamura, A., Ogawa, H., & Fukui, Y. 1998, ApJ, 502, 296

Onishi, T., Kawamura, A., Abe, R., Yamaguchi, N., Saito, H., Moriguchi, Y., Mizuno, A., Ogawa, H., & Fukui, Y. 1999, PASJ, 51, 871

Pawsey, J. L. 1951, Nature, 168, 358

Pound, M. W., Wilson, R. W., & Bania, T. M. 1990, ApJ, 351, 165

Pound, M. W. 1996, ApJ, 457, 35

Reach, W. T., Koo, B. C., & Heiles, C. 1994, ApJ, 429, 672

Reach, W. T., Pound, M. W., Wilner, D. J., & Lee, Y. ApJ, 1995, 441, 244

Reach, W. T., Wall, W. F., & Odegard, N. 1998, ApJ, 507, 507

Schlegel, D. J., Finkbeiner, D. P., & Davis, M. 1998, ApJ, 500, 525

Solomon, P. M., Rivolo, A. R., Barrett, J., & Yahil, A. 1987, ApJ, 319, 730

Stark, R., & van Dishoeck, E. F. 1994, ApJ, 286, 43

Tachihara, K., Mizuno, A., & Fukui, Y. 2000, ApJ, 528, 817

van Dishoeck, E. F., & Black, J. H. 1988, ApJ, 334, 771

Table 1–1. The performance of the NANTEN telescope

Parameter	Value
Antenna	
Diameter	4 m
Type	Cassegrain (CFRP)
Beam width	2′.6 at 115 GHz
	2′.7 at 110 GHz
Surface accuracy	47 μm rms
Pointing accuracy	$\leq$ 20″ rms
Receiver	
Type	4 K cooled Nb SIS mixer
Noise temperature	$\leq$ 100 K in SSB at 85–115GHz
System Noise Temperature*	$\sim$120 K at 85–110GHz
	$\sim$240 K at 115GHz
Intermediate Frequency	
First	1500$\pm$500 MHz
Second	375$\pm$125 MHz
Third	65$\pm$20 MHz
Backend Type	Acousto-Optical Spectrometer (AOS)
Narrow band	
Frequency resolution	40 kHz (0.10 km s^{-1})
Frequency coverage	40 MHz (100 km s^{-1})
Wide band	
Frequency resolution	250 kHz (0.65 km s^{-1})
Frequency coverage	250 MHz (650 km s^{-1})
Observing Mode	Beam Switch, Position Switch,
	and Frequency Switch
Location	Las Campanas Observatory, Chile
Coodinates	70°42′00″W, 29°00′30″S
Altitude	2400 m

* Typical values during the observation, toward the zenith including the atmosphere.

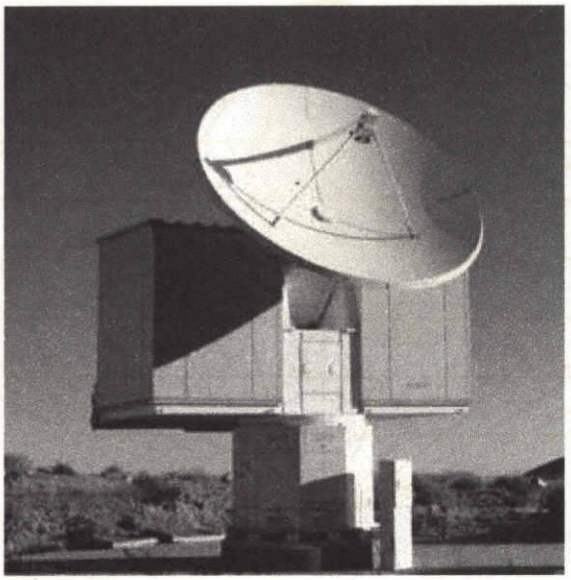

Figure 1–1. The NANTEN telescope at Las Campanas Observatory, Chile.

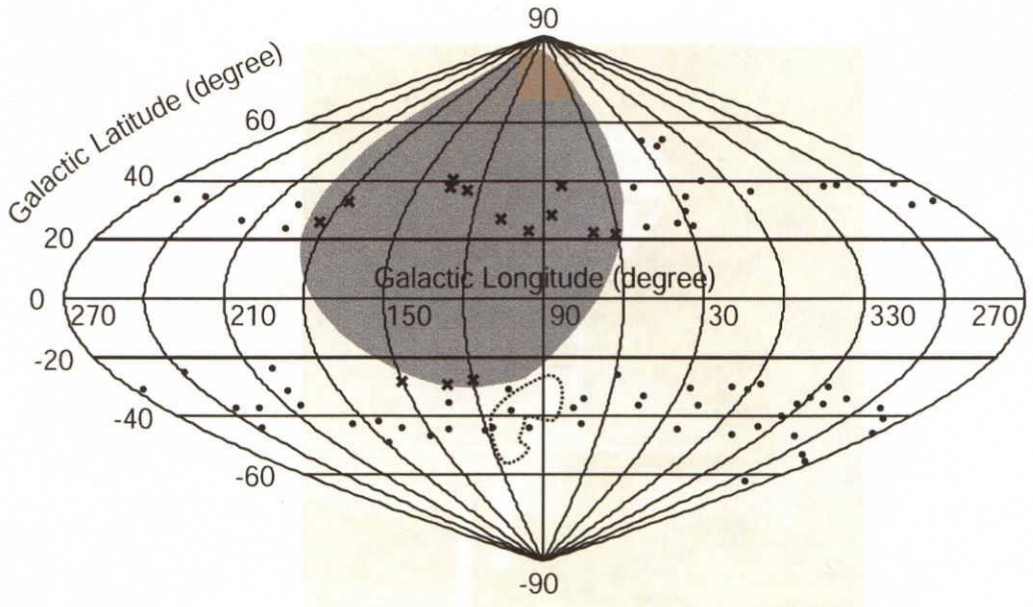

Figure 1–2. The distribution of far infrared excess clouds. The filled circles and crosses indicate the far infrared excess clouds which can and can not be accessed from the NANTEN telescope, respectively. The shaded area is the part of the sky invisible from the NANTEN telescope. The dotted line indicates the area where two large scale structures exist (In details, see fig 1–3).

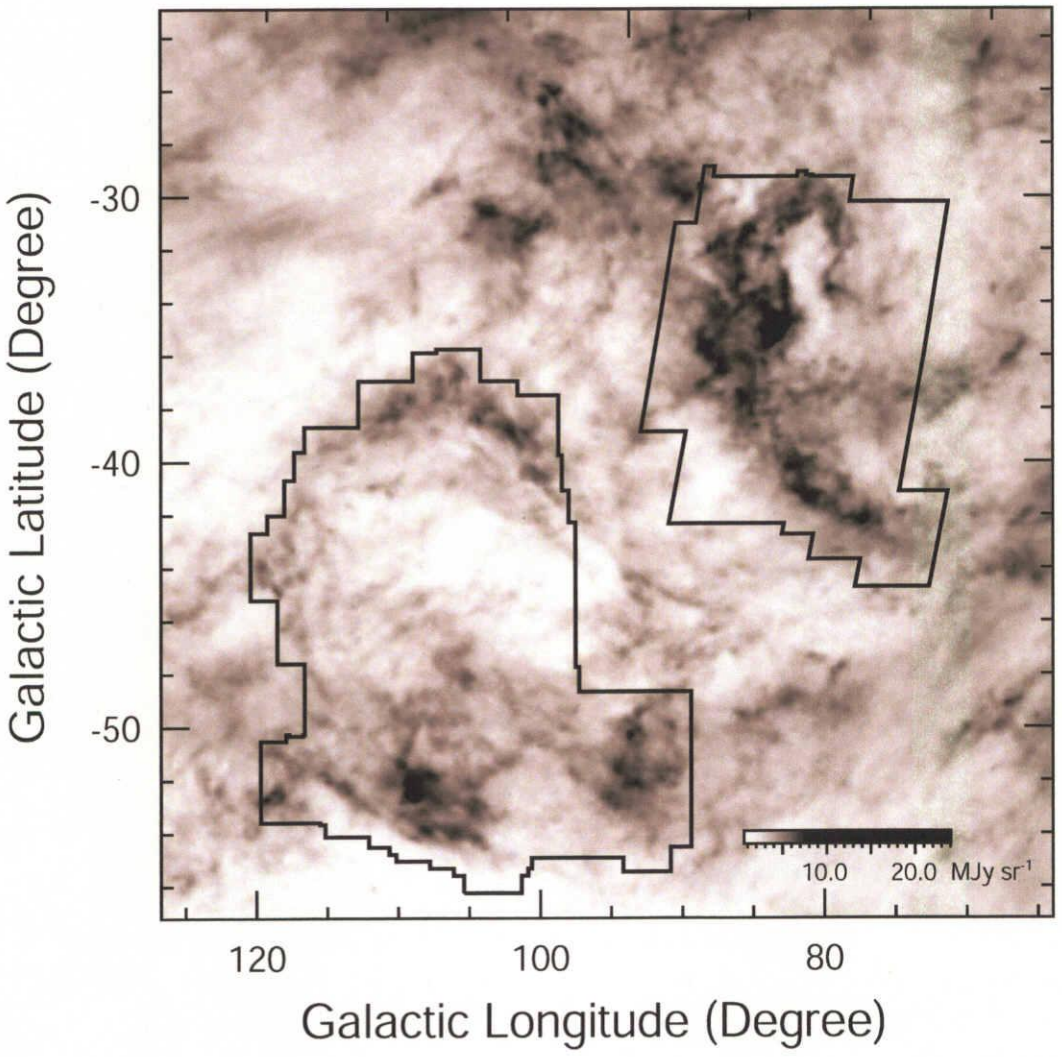

Figure 1–3. The large scale 100 μm map derived by Schlegel et al. (1998). The observed regions of two large structures are denoted by solid lines.

Chapter 2

A survey for HLCs toward Infrared-Excess Clouds

Abstract

A survey for high Galactic latitude molecular clouds was carried out toward the far-infrared-excess clouds of Reach et al. (1998, AAA 070.131.207), using the NANTEN telescope. All 68 infrared-excess clouds that are observable from NANTEN were mapped in the J=1–0 line of ^{12}CO. CO emission was detected from 32 infrared excess clouds, corresponding to a CO detection rate of 47%. Most of these CO clouds were identified and mapped as high-latitude clouds for the first time. The CO detection rate for the cold ($T_{\rm dust}$ < 17 K) infrared excess clouds is 72%, which is more than a factor of two higher than that of warmer ones, 33%. This indicates that the cold clouds are well shielded from external UV radiation, resulting in a high CO abundance and a low temperature of the clouds. The infrared-excess clouds with no CO emission are most likely to be molecular hydrogen clouds because the temperature is similar to, or lower than, that of the surrounding H I gas. The molecular gas without CO emission seems to occupy more than 90% of the area of the infrared-excess clouds.

Key Words : ISM: clouds — ISM: dust, extinction — ISM: individual (High Latitude Clouds) — ISM: molecules

2.1 Introduction

Most of the subsequent HLCs surveys were carried out mainly in the northern hemisphere (Magnani et al. 1996 and the references therein), although some authors surveyed high-latitude clouds in the southern sky (e.g., Keto, Myers 1986; Kawamura et al. 1999). Since HLCs are far from far-UV sources, most of them are probably exposed to the average interstellar far-UV field stars (see van Dishoeck, Black 1988; Draine 1978). The absence of internal disturbing sources and a uniform far-UV field makes the study of HLCs simpler than that of star-forming clouds. Magnani et al. (1996) summarized surveys of HLCs and cataloged more than 100 objects as of this moment. It is to be noted that not all of the objects were fully covered by the CO observations. Many of them were observed just toward only a few positions.

A survey for HLCs in ^{12}CO was made by Hartmann, Magnani, and Thaddeus (1998) and Magnani et al. (2000). They estimated the mass surface density of molecular gas based on the survey. The extremely sparse sampling grid compared with its beam size may however lead to missing small molecular clouds located between the observed points (in details, see section 1.3).

Under the above circumstances, we have started a high-latitude molecular cloud survey using the NANTEN telescope. This telescope has a millimeter-wave receiver with one of the best system noise temperatures and excellent sky conditions (see Table 1–1). This enabled us to survey for molecular clouds over a large area within a short time. Even with this telescope, the area of Galactic high-latitude is very large and the intensity of the low-density clouds is so weak that we cannot cover the whole area with a full-sampling grid in a reasonably short time.

For the first survey of HLCs by NANTEN, we used a catalog of far-infrared excess clouds at high Galactic latitude by Reach, Wall, and Odegard (1998; hereafter RWO). These authors suggest that clouds with far-infrared excess over H I emission are good candidates for molecular clouds. Because the area filling factor of their clouds is about 1.4% of the whole area of $|b| > 25°$, we can cover all of the clouds in a relatively short observation time from the sourthern hemisphere.

In this chapter, we present the observation parameters in section 2.2, and the results of the survey in section 2.3. In section 2.4, we discuss the physical properties of the detected CO clouds and the infrared excess clouds as well as future observations.

2.2 Observations

2.2.1 Far-Infrared Excess Clouds

The targets which we observed were chosen from a catalog of far-infrared excess clouds by RWO. This catalog is an updated version of that by Désert, Bazell, and Boulanger(1988, hereafter DBB) with a better dataset of both far-infrared and H I data. The infrared excess is defined to be the observed infrared surface brightness minus the contributions from dust associated with the atomic interstellar medium, the zodiacal light, and the cosmic infrared background radiation. If we assume that the amount of dust is proportional to that of the atomic hydrogen plus molecular hydrogen, and that the radiation field, gas-to-dust ratio, and temperature are uniform throughout the entire region, the amount of infrared excess is expected to be proportional to that of molecular hydrogen. RWO made maps of the infrared excess over H I by using far-infrared data from the Cosmic Background Explorer (COBE) Diffuse Infrared Background Experiment (DIRBE) (Hauser et al. 1998) and H I data from the combined Leiden–Dwingeloo (Hartmann, Burton 1997) and Parks (Cleary et al. 1979) 21 cm line surveys. Because the dust temperature of the excess cloud is found to be similar to, or colder than, that of the surrounding dust in H I clouds, they concluded that the excess is caused by dust associated with gas other than the atomic interstellar medium, i.e., molecular gas. Therefore, these excess clouds are good candidates for clouds that contain molecular material. The spatial resolution of the map is $\sim 1^\circ$, which is fairly large compared with that of IRAS or NANTEN ($\sim$ a few arcmin).

We should note here that Blitz, Bazell, and Désert (1990) observed infrared-excess clouds cataloged by DBB. They detected CO emission only toward 13% of the sample. They discussed that the DBB clouds without CO are likely to be diffuse molecular clouds and that many of the low-excess clouds may be artifacts of the analysis because of the quality of the dataset they used. Another possible cause of this low detection rate is that Blitz et al. (1990) observed only one or two points toward the excess clouds. In the present study, we therefore decided to cover most of the area of the far-infrared excess clouds by RWO, who used a dataset of better quality than that by DBB.

2.2.2 CO Observations by NANTEN

From the infrared-excess cloud catalog by RWO (Table 4), we have observed all objects whose maximum elevation angle is greater than 30° at Las Campanas in the J=1–0 line of ^{12}CO (rest frequency of 115.207 GHz). The number of the targets is 68. Since the spatial resolution of the maps of infrared excess is much larger than that of the NANTEN telescope, we used IRAS 100 μm images as guide maps. First, we observed an IRAS 100 μm cloud near the position of RWO. If CO emission was not detected, we observed an area of at least 2° × 2° with a grid spacing of 8′ with rms fluctuations of ∼0.4 K (in $T_{\rm R}^{*}$) in 0.1 km s^{-1} resolution. The total number of observed position was ∼15000. If CO emission exists at the edge of the map, we extended the observation until the emission disappeared. Some of the small CO clouds were observed with a 4′ or 2′ grid.

The observations were carried out with the NANTEN telescope in 1999 May and October. The observation was performed by frequency swithing mode and by using an acousto-optical spectrometer of narrow band. A typical integration time per observed points was ∼30 s. The detailed parameters of the NANTEN telescope are descraibed in section 1.4.

A room-temperature chopper wheel was employed for an intensity calibration. An absolute intensity calibration was made by observing Orion KL [α(1950) = $5^{\rm h}32^{\rm m}47.^{\rm s}0$, δ(1950) = −5°24′21″] for ^{12}CO (assuming 65 K).

2.3 Results

Among the 68 infrared-excess clouds, we detected CO emission toward 32 objects. In Table 2–1, we present a table of the observed and CO detected objects as well as the peak ($T_{\rm R}^{*}$) of each one. Column 4 in Table 2–1 shows the highest $T_{\rm R}^{*}$ in each cloud, and columns 5 and 6 in it show the position in Galactic coordinates. The "no" in column 4 in the table indicates no detection of CO. The detection rate is then 47%. This value is much higher than that of Blitz et al. (1990) for DBB clouds. Most of the CO clouds were not identified as CO high-latitude clouds previously. DIR 071−43, DIR 105−38, DIR 105−31, DIR 121−45, DIR 164−44, DIR 172−42, and DIR 203−32 were observed by Magnani et al. (2000) during the course of a 1° grid survey for high-latitude clouds. Because of the coarse sampling, each DIR cloud typically has a few observed points.

The distribution of the infrared-excess clouds in Tables 3, 4 of RWO is presented

in Figure 2–1. In this figure, the distribution is not symmetrical. For the Galactic south ($b < -25°$), the CO detection rate in Galactic east, $0° < l < 180°$, was calculated to be 82%, whereas that in Galactic west, $180° < l < 360°$, is only 24 %. Although the shadowed area could not be observed in this survey, the number of the CO high-latitude clouds, including the previously identified ones, seems to be preferentially concentrated in the Galactic southwest area.

We present here the average physical properties of the clouds. Most of the infrared excess clouds with CO emission have multiple cloud clumps in them. We identified 137 clumps in total. For the 63 clumps with more than 3 observed points, we derived the physical parameters. We assume the distance to the clouds to be 100 pc in the following. The radius, line width(FWHM), peak T_R^*, mass derived from CO luminosity, and virial mass are 0.15–0.67 pc, 0.8–3.4 km s^{-1}, 1.0–10.6 K, 0.4–14 $M_\odot$, and 40–1500 $M_\odot$, respectively. We assumed the CO/H_2 ratio $[N(H_2)/W(CO)]$ to be 1.3×10^{20} cm^{-2} (K km $s^{-1})^{-1}$ (RWO) when we calculated the mass. The averages are 0.33 pc, 1.95 km s^{-1}, 2.9 K, 3.2 $M_\odot$, and 300 $M_\odot$, respectively. These parameters are similar to those of previously identified high-latitude clouds, although the size and mass is smaller, probably because of the small beam size of the telescope. The total mass derived from the CO luminosity is estimated to be $\sim$250 $M_\odot$. These physical parameters of moleculer clouds are listed in Table 2–2.

Figure 2–2 shows an integrated intensity map of molecular clouds we detected. DIR 172−42 is the largest one among the detected CO clouds. The total mass is estimated to be $\sim$80 $M_\odot$ from the CO luminosity. It is shown that the cloud consists of $\sim$30 small clumps. The radii of most of the clumps are less than 0.5 pc and the masses are typically 1 $M_\odot$ or less. Two of the largest ones have a mass of 10 and 5 $M_\odot$, a radius of 0.55 and 0.39 pc, respectively.

2.4 Discussion

2.4.1 Distribution of Newly Detected CO High Latitude Clouds

In total, 32 high-latitude clouds have been mapped in CO for the first time, which includes 137 CO clumps. The area of CO detection is $\sim$10 deg^2, corresponding to a surface filling factor of 0.05% of the area of $|b| > 25°$. This value corresponds to 20% of the estimated surface filling factor for the northern Galactic hemisphere based on observations with a 1° grid of 0.25% (Hartmann et al. 1998). For the southern Galactic hemisphere (Magnani et al. 2000), the value is much higher, although only a small fraction of the southern sky was observed. The total mass of molecular clouds in northern Galactic hemisphere is estimated to be $\sim$800 $M_\odot$ with the same conversion factor from N(CO) to $N(H_2)$ (Hartmann et al. 1998). Our observed mass is $\sim$250 $M_\odot$, which corresponds to $\sim$30% compared with their mass. This fact indicates that the amount of molecular gas found by the present survey is still not negligible, although various types of surveys for HLCs were carried out previously.

The total area of the infrared-excess clouds with CO was calculated to be $\sim$130 deg^2. Therefore, the surface filling factor of the CO-emitting area in the infrared-excess clouds is only $\sim$8%. The CO cloud is much smaller than the infrared clouds, typically smaller than a few $\times$ 10′, and appears to be embedded in them.

All of these results suggest that the survey of HLCs with a grid spacing of $\lesssim$ 10′ not biased on optical obscuration is still needed to understand the molecular distribution at high Galactic latitude.

2.4.2 Detection Rate of CO toward Infrared-Excess Clouds

As mentioned in section 2.3, the CO detection rate of the infrared-excess clouds of RWO is observed to be 47%. This high detection rate implies that the infrared clouds of RWO are most likely molecular clouds, and that the method used by RWO is very useful to search for molecular clouds at high Galactic latitude.

The present detection rate is much higher than that of Blitz et al. (1990) for DBB clouds. The main cause of this is probably the worse data quality of far-infrared and H I data in DBB, as discussed by both Blitz et al. (1990) and RWO. About half of the DBB clouds have no infrared excess in the RWO map (RWO). If we take this value into account, the percentage given by Blitz et al. (1990) increases up to 26%. This value is too small to explain our high value of 47%. This is probably because

they observed only one or two positions toward the DBB clouds. The size of the DBB or RWO clouds is $\sim$ a few deg, whereas that of the CO clumps is $\sim 20'$ (see section 2.3). This means that observations of only one or two points may miss CO molecular clouds with high probability.

2.4.3 CO Properties of the Infrared-Excess Cloud

We now discuss the difference between infrared-excess clouds with and without CO emission. Figure 2–3(a) shows histograms of the dust temperature measured from 100 μm and 240 μm (RWO) for infrared-excess clouds with and without CO. It is apparent that the dust temperature of the infrared-excess clouds with CO is colder than that without CO. Actually, the detection rates for infrared-excess clouds whose dust temperature is lower and higher than 17 K are 72% and 33%, respectively. Figure 2–3(b) shows histograms of the total amount of infrared excess by RWO. There seems to be no correlation between the CO detection rate and the amount of excess.

The fact that colder infrared-excess clouds tend to have CO emission indicates that these clouds are well shielded from the external UV radiation, resulting in a high CO abundance and a low temperature of the clouds. Warin, Benayoun, and Viala (1996) calculated the chemical abundances of H_2, CO, and the isotopes in molecular clouds (diffuse, translucent, and dark ones) submitted to a not too intense radiation field. The ^{12}CO molecule becomes abundant around $\tau_v = 0.5$–1.0 as the gas temperature changes from 20 K to 10 K. From their calculations, the temperature of a CO cloud is inevitably close to 10 K. Our CO-detected cloud is then in the regime of a translucent cloud based on their category (also see van Dishoeck, Black 1988).

We should note here that the filling factor of CO clouds in infrared-excess clouds is about 8%, as discussed in the previous section, although the average dust temperature of the infrared-excess clouds shows a good correlation with the CO detection rate. If we assume that the temperature of the CO cloud is 10 K and the surrounding gas is 19 K, the average dust temperature of this infrared excess cloud is still calculated to be 18 K. This indicates that the surrounding gas of a CO cloud in an infrared-excess cloud must have a lower temperature compared with that of atomic gas. There should be a negative temperature gradient from the outer parts to the inner parts of the infrared-excess clouds.

Then, what is an infrared-excess cloud without CO emission? The infrared excess can be observed from molecular material, from gas at a higher temperature than the

surroundings, or from gas with a different gas-to-dust ratio, as discussed by RWO and Blitz et al. (1990). The dust temperature of the infrared-excess clouds without CO is still similar to, or lower than, that of the atomic component. Therefore, the excess is not due to the high temperature of the clouds. The third possibility, a different dust-to-gas ratio, cannot be completely ruled out. However, it is unlikely that many tiny regions with different ratios are distributed almost uniformly around the sky (see also Blitz et al. 1990). These results indicate that the infrared-excess clouds with no CO emission are most likely to be molecular hydrogen clouds. The CO molecule is probably selectively destructed by UV radiation in the clouds.

In a translucent cloud, the CO intensity can fluctuate largely due to a small change in the physical parameters according to chemical calculations (van Dishoek, Black 1988; Viala et al. 1988). In these models, there is a possibility that a layer of molecular gas without CO can exist. Magnani et al. (1998) measured the conversion factor, X_{CO}, between the velocity-integrated CO (J=1–0) antenna temperature, W(CO), and the H_2 column density, $N(H_2)$, based on observations of the CO and CH hyperfine transition. X_{CO} varies at least by an order of magnitude even in a single HLC. This also indicates that for low-density gas the CO abundance can change greatly. The CO abundance should depend on the morphology of the cloud, including both the column densities and the density at that position, because the UV radiation is considered to be uniform around the Solar system due to a lack of UV sources, like OB stars. Comparisons among IRAS, CO, and H I data by other authors have led to a discussion on the existence of molecular gas not traced by CO emission. Abergel et al. (1995) have reported the existence of molecular gas not traced by CO emission in Taurus, and Boulanger et al. (1998) summarized the discussion on this type of cloud.

If we assume that all of the infrared-excess clouds (all the objects in Tables 3 and 4 of RWO) are molecular-hydrogen clouds, the surface filling factor is estimated to be $\sim$1.4% (340 deg^2) of $|b| > 25°$. As discussed in subsection 4.1, the CO-emitting region is estimated to be 8% of the area, even in infrared-excess clouds with CO. Heithuasen et al. (1993) and Meyerdierks and Heithausen (1996) have claimed the existence of molecular gas without the associated CO emission, accounting for about 1/3 of the total mass in the Polaris Flare. Our results suggest that most of the mass of the infrared-excess cloud by RWO seem to consist of molecular gas without CO emission. This means that quite a large area is in the transition phase between the atomic and molecular components. It is of vital importance to observe such regions in order to understand how a molecular cloud is formed in atomic-hydrogen gas. Observations of far-infrared (longer than 100 μm) and H I with a finer resolution

compared with millimeter–submillimeter observations of $\sim$ a few arcmin or smaller are definitely needed because CO cannot be detected in such a diffuse region. Also, C I observations with the same resolution are needed to detect the phase transition between C I and CO.

2.5 Conclusions

A survey of high Galactic latitude molecular clouds was carried out toward far-infrared excess clouds using the NANTEN telescope. The catalog of infrared-excess clouds is from Reach et al. (1998). These clouds are considered to be good candidates for molecular clouds. The main conclusions presented in this paper are summarized below:

1. All of the 68 infrared-excess clouds that are observable from NANTEN have been mapped in the J=1–0 line of ^{12}CO. CO emission has been detected from 32 infrared-excess clouds. Most of the clouds have been identified and mapped in CO as high-latitude clouds for the first time. In 32 infrared-excess clouds, we identified 137 CO cloud clumps. The average properties of the clumps are presented.

2. The CO detection rate is found to be 47%. This value is much higher than that derived by Blitz et al. (1990), 13%, based on DBB clouds. The causes of this low detection are considered to be the poorer data quality of far-infrared data and H I data and only one or two observations toward infrared-excess clouds.

3. The CO detection rate for the cold ($T_{\rm dust} < 17$ K) infrared-excess clouds is 72%, which is much higher than that of warmer ones, 33%. This indicates that the cold clouds are well shielded from any external UV radiation, resulting in a low temperature of the clouds and prevention from destruction of the CO molecule. The filling factor of CO clouds in infrared-excess clouds is only about 8%, although the average dust temperature of the infrared-excess clouds shows a good correlation with the CO detection rate. This indicates that the surrounding gas of a CO cloud in an infrared-excess cloud must have a lower temperature compared with that of atomic gas. There should be a negative temperature gradient from the outer part to the inner part of the infrared-excess clouds.

4. The infrared-excess clouds with no CO emission are most likely to be molecular hydrogen clouds because the temperature is similar to, or lower than, that of the surrounding H I gas. The molecular gas without CO emission seems to occupy more than 90% of the area of the infrared-excess clouds.

References

Abergel, A., Boulanger, F., Fukui, Y., & Mizuno, A. 1995, A&AS, 111, 483

Blitz, L., Bazell, D., & Désert, F. X. 1990, ApJ, 352, L13

Boulanger, F., Bronfman, L., Dame, T. M., & Thaddeus, P. 1998, A&A, 332, 273

Cleary, M. N., Heiles, C., & Haslam, C. G. T. 1979, A&AS, 36, 95

Désert, F. X., Bazell, D., & Boulanger, F. 1988, ApJ, 334, 815 (DBB)

Draine, B. T. 1978, ApJS, 36, 595

Hartmann, D., & Burton, W. B. 1997, Atlas of Galactic Neutral Hydrogen (Cambridge: Cambridge Univ. press)

Hartmann, D., Magnani, L., & Thaddeus, P. 1998, ApJ, 492, 205

Hauser, M. G., Kelsall, T., Leisawitz, D., & Weiland, J. 1998, COBE Diffuse Infrared Background Experiment (DIRBE) Explanatory Supplement version 2.3, COBE Ref. Pub. No. 98-A (Greenbelt, MD: NASA/GSFC), available in electronic form from the NSSDC (http://space.gsfc.nasa.gov/astro/cobe/dirbe_exsup.html).

Heithausen, A., Satcy, J. G., de Vries, H. W., Mebold, U., & Thaddeus, P. 1993, A&A, 268, 265

Kawamura, A., Onishi, T., Mizuno, A., Ogawa, H., & Fukui, Y. 1999, PASJ, 51, 851

Keto, E. R., & Myers, P. C. 1986, ApJ, 304 466

Magnani, L., Hartmann, D., Holcomb, S. L., Smith, L. E., & Thaddeus, P. 2000, ApJ, 535, 167

Magnani, L., Hartmann, D., & Speck, B. G. 1996, ApJS, 106, 447

Magnani, L., Onello, J. S., Adams, N. G., Hartmann, D., & Thaddeus, P. 1998, ApJ, 509, 290

Meyerdierks, H., & Heithausen, A. 1996, A&A, 313, 929

Reach, W. T., Wall, W. F., & Odegard, N. 1998, ApJ, 507, 507 (RWO)

van Dishoeck, E. F., & Black, J. H. 1988, ApJ, 334, 771

Viala, Y. P., Letzelter, C., Eidelsberg, & M. Rostas, F. 1988, A&A, 193, 265

Warin, S., Benayoun, J. J., & Viala, Y. P. 1996, A&A, 308, 535

Table 2–1. CO properties of infrared-excess clouds

Name	$T_{\rm dust}$ (K)	$F_{\rm ex}$ (kJy)	$T_{\rm R}^{*}$ (K)	l (°)	b (°)
DIR 002−31	18.4	0.89	no		
DIR 009−30	16.5	2.50	2.02	9.27	−30.93
DIR 013+40	17.1	1.31	2.79	13.37	38.87
DIR 015+54			no		
DIR 018−37	12.2	0.04	0.43	17.19	−36.57
DIR 020−45	18.9	0.69	no		
DIR 021+52	17.5	0.29	no		
DIR 025+35	21.8	2.96	no		
DIR 027−31	15.3	0.52	1.19	26.27	−30.13
DIR 028+54	17.3	0.29	no		
DIR 029+25	16.6	2.15	3.09	28.13	25.40
DIR 029+30	16.7	0.72	1.36	28.20	28.87
DIR 034+26	18.6	3.21	no		
DIR 046−33	22.4	0.72	1.82	46.00	−32.07
DIR 046−37	16.1	1.24	4.33	45.53	−36.53
DIR 048+25	16.9	1.49	1.01	47.47	24.47
DIR 048+38	18.0	1.56	2.02	47.67	37.27
DIR 060−26	22.3	1.07	no		
DIR 071−43	15.5	3.14	3.31	71.67	−42.77
DIR 072−34	15.9	0.43	5.82	71.23	−33.80
DIR 077−37	18.5	1.75	1.41	76.63	−38.87
DIR 098−44	17.4	0.97	1.93	96.53	−44.33
DIR 105−31	15.3	1.16	4.07	103.80	−31.40
DIR 105−38	15.7	2.48	4.34	103.73	−39.33
DIR 117−44	18.0	0.70	3.78	116.23	−44.93
DIR 121−45	15.5	0.57	3.34	121.93	−46.07
DIR 134−36	16.3	0.62	1.82	134.20	−35.47
DIR 140−45	19.8	0.63	2.62	138.80	−44.33
DIR 152−47	16.2	2.74	2.34	151.07	−46.20
DIR 164−44	17.0	0.61	2.73	162.93	−43.60
DIR 172−42	15.6	2.87	4.01	172.13	−39.87
DIR 179−49	20.4	1.68	no		
DIR 187−43	20.4	0.58	no		
DIR 196+24	17.2	0.46	no		
DIR 198+32	15.8	0.61	no		
DIR 201−24	19.9	0.39	no		
DIR 203−32	14.9	0.33	10.08	203.53	−30.00
DIR 204−37	15.6	0.79	3.25	202.72	−36.68

Table 2–1. (Continued)

Name	$T_{\rm dust}$ (K)	$F_{\rm ex}$ (kJy)	$T_{\rm R}^{*}$ (K)	l (°)	b (°)
DIR 216+27	16.2	0.34	no		
DIR 223−37	22.3	1.21	no		
DIR 234−37	21.2	0.65	no		
DIR 237−44	19.7	0.72	no		
DIR 239−25	20.5	3.34	no		
DIR 245+35	17.1	0.88	0.83	244.47	33.73
DIR 257+34	16.2	0.76	no		
DIR 265−31	16.2	1.96	no		
DIR 274−46	18.1	0.63	no		
DIR 276+33	18.4	0.52	no		
DIR 280−55	17.0	0.91	no		
DIR 281+40	23.6	0.48	no		
DIR 282−41	17.6	3.42	2.16	282.40	−39.77
DIR 288+32	18.5	2.12	no		
DIR 289−53	16.2	0.95	no		
DIR 290−62	18.3	2.20	no		
DIR 292−37	17.7	2.71	0.95	293.07	−36.93
DIR 310+39	16.8	0.99	0.77	310.13	38.60
DIR 313−34	18.1	0.62	2.18	313.13	−34.40
DIR 314−47	19.8	2.76	no		
DIR 316+39	18.6	0.61	0.98	316.20	37.27
DIR 321−36	19.2	2.32	no		
DIR 327−30	17.6	2.86	2.17	326.53	−29.47
DIR 331−34	21.4	0.69	no		
DIR 333−36	17.0	0.74	no		
DIR 335−40	19.1	0.71	no		
DIR 340−43	16.0	0.50	no		
DIR 349−46	20.1	0.93	no		
DIR 354+37	17.8	0.72	no		
DIR 357−29	15.7	0.60	no		

Table 2–2. Physical Properties of ^{12}CO Clouds

Name (1)	No. (2)	l (3)	b (4)	T_R^* (5)	V_{LSR} (6)	ΔV (7)	R (8)	M_{CO} (9)
DIR 013+40	1	13.37	38.87	2.8	1.0	0.8	0.29	0.8
DIR 027−31	1	26.27	−30.13	1.2	−1.5	1.5	0.15	0.4
DIR 029+25	1	28.13	25.40	3.1	−0.2	1.2	0.56	5.1
DIR 046−33	1	45.73	−33.27	1.8	1.4	1.8	0.23	0.9
	2	45.73	−33.80	1.0	1.6	2.3	0.19	0.6
	3	45.87	−33.00	1.1	3.5	2.2	0.26	1.1
DIR 046−37	1	43.20	−36.47	1.0	−4.4	2.0	0.26	0.9
	2	43.60	−36.87	1.3	−3.2	2.3	0.19	0.5
	3	43.87	−36.20	0.6	−4.2	2.3	0.15	0.3
	4	44.60	−36.33	2.4	3.0	1.5	0.23	0.9
	5	45.53	−36.53	4.3	0.2	3.4	0.35	2.7
DIR 048+38	1	47.67	37.27	2.0	−3.6	2.4	0.43	4.1
	2	47.93	38.13	1.3	−3.0	1.9	0.15	0.4
DIR 071−43	1	71.40	−42.23	3.2	−5.6	1.7	0.44	4.5
	2	71.67	−42.77	3.3	−6.3	1.4	0.45	5.0
DIR 072−34	1	71.23	−33.80	5.8	−8.8	2.4	0.33	3.5
DIR 077−37	1	76.63	−38.87	1.4	−6.9	1.6	0.13	0.1
DIR 098−44	1	96.53	−44.33	1.9	−11.6	2.1	0.32	2.1
DIR 105−31	1	103.80	−31.40	4.1	−9.3	2.0	0.51	5.9
	2	103.93	−31.80	1.6	−10.9	1.7	0.23	0.7
	3	105.93	−30.60	1.7	−9.6	2.4	0.56	5.3
DIR 105−38	1	103.73	−39.33	4.3	−9.3	2.5	0.67	11.2
	2	105.87	−38.40	2.9	−3.9	2.5	0.59	13.5
DIR 117−44	1	116.23	−44.93	3.8	−3.8	2.1	0.64	13.8
	2	116.77	−44.67	2.1	−2.7	2.7	0.45	4.2
DIR 121−45	1	120.07	−44.47	2.7	−5.5	2.2	0.29	2.1
	2	121.93	−46.07	3.3	−2.1	1.7	0.39	4.2
DIR 134−36	1	134.20	−35.47	1.8	−5.5	0.8	0.35	1.4
DIR 140−45	1	139.87	−44.87	1.6	−1.0	3.0	0.23	1.6
	2	140.27	−44.87	1.5	−0.8	2.2	0.23	1.2
	3	140.80	−45.27	2.1	0.5	1.8	0.37	3.0
DIR 152−47	1	151.07	−46.20	2.3	−9.1	1.7	0.39	4.0
DIR 164−44	1	162.40	−44.13	2.0	−13.5	1.8	0.23	1.1
	2	162.93	−43.60	2.7	−5.4	2.2	0.23	1.0
	3	163.07	−44.40	0.9	−10.5	2.2	0.23	0.8
	4	163.60	−43.33	1.7	−7.0	1.8	0.29	1.6
	5	164.53	−43.60	1.1	−9.8	2.7	0.29	1.5
	6	164.93	−43.60	1.2	−9.1	1.6	0.23	0.9

Table 2–2. (Continued)

Name (1)	No. (2)	l (3)	b (4)	T_R^* (5)	V_{LSR} (6)	ΔV (7)	R (8)	M_{CO} (9)
DIR 172−42	1	168.93	−42.73	2.3	−8.6	1.3	0.35	3.1
	2	168.93	−43.20	2.0	−2.0	3.6	0.56	9.5
	3	169.60	−44.27	3.5	−9.0	1.8	0.51	5.5
	4	169.73	−42.53	2.7	−8.5	2.0	0.39	4.8
	5	169.47	−45.47	2.4	−10.2	1.8	0.35	2.8
	6	169.73	−43.60	2.3	−5.9	1.6	0.23	0.9
	7	169.60	−44.00	1.6	−10.4	1.5	0.23	1.1
	8	170.13	−42.93	1.6	−3.1	3.4	0.44	4.0
	9	170.27	−43.07	2.3	−9.5	1.1	0.23	0.9
	10	170.53	−42.53	2.0	−9.2	2.1	0.35	2.4
	11	171.33	−41.33	3.3	−7.6	1.6	0.42	3.9
	12	171.60	−41.47	1.6	10.2	2.4	0.63	8.9
	13	172.13	−39.87	4.0	−6.8	1.8	0.49	7.0
	14	173.47	−39.47	3.2	−8.6	1.5	0.59	7.2
	15	173.20	−41.47	3.8	9.1	2.5	0.32	4.3
	16	174.00	−41.60	3.8	7.9	1.4	0.32	3.2
DIR 203−32	1	202.47	−31.27	3.4	−6.2	1.5	0.24	1.2
	2	202.80	−31.93	2.7	4.9	1.7	0.13	0.4
	3	202.93	−31.67	1.5	5.7	1.9	0.13	0.4
	4	203.53	−30.00	10.1	−4.8	1.4	0.48	13.1
DIR 204−37	1	202.72	−36.68	3.3	12.8	1.3	0.15	0.5
DIR 282−41	1	282.40	−39.77	2.2	3.3	1.8	0.23	1.5
DIR 313−34	1	313.13	−34.40	2.2	5.8	2.2	0.23	1.0
DIR 327−30	1	326.60	−29.73	1.8	−0.9	1.6	0.16	0.5
	2	328.30	−30.77	1.4	4.9	2.8	0.23	1.4

Note—Col. (1) : Name of infrared-excess cloud, Col. (2) : Cloud number of each object, Col. (3)–(4) : peak (l, b) position in degree, Col. (5) : Peak temperature in K, Col. (6) : Peak velocity of the peak position in km s^{-1}, Col. (7) : Line width of the composite spectrum in km s^{-1}, Col. (8) : Radius of the molecular cloud in pc, Col. (9) : Mass of the molecular cloud in $M_\odot$. Col. (5) to (7) are derived by using a single Gaussiun fitting.

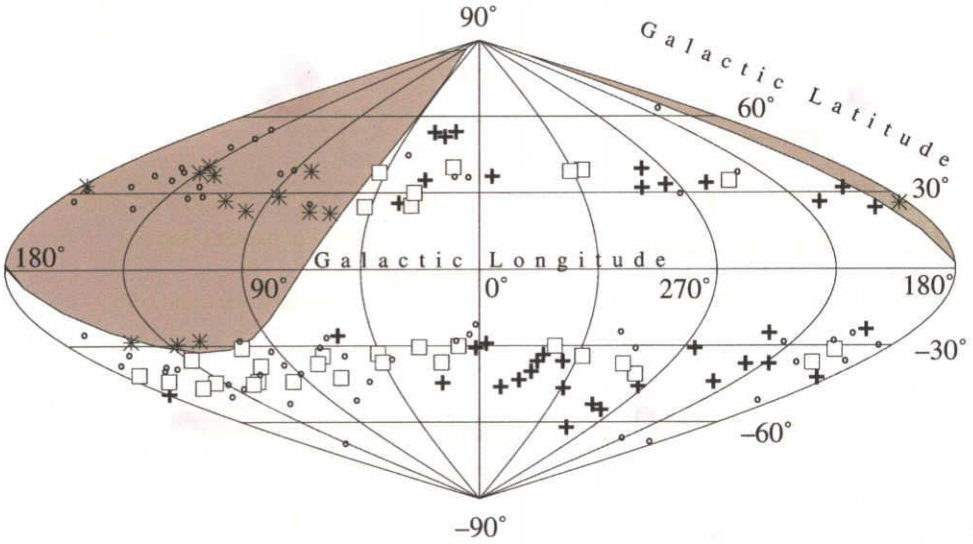

Figure 2–1. Distribution of the infrared-excess clouds of RWO. The open rectangles indicate those clouds with CO emission. The crosses, stars, and small open circles indicate the infrared-excess clouds with no CO emission, unidentified ones that are not observable from Chile, and the ones with known HLC counterparts (Table 3 of RWO), respectively. The shaded area is the invisible part of the sky from Las Campanas.

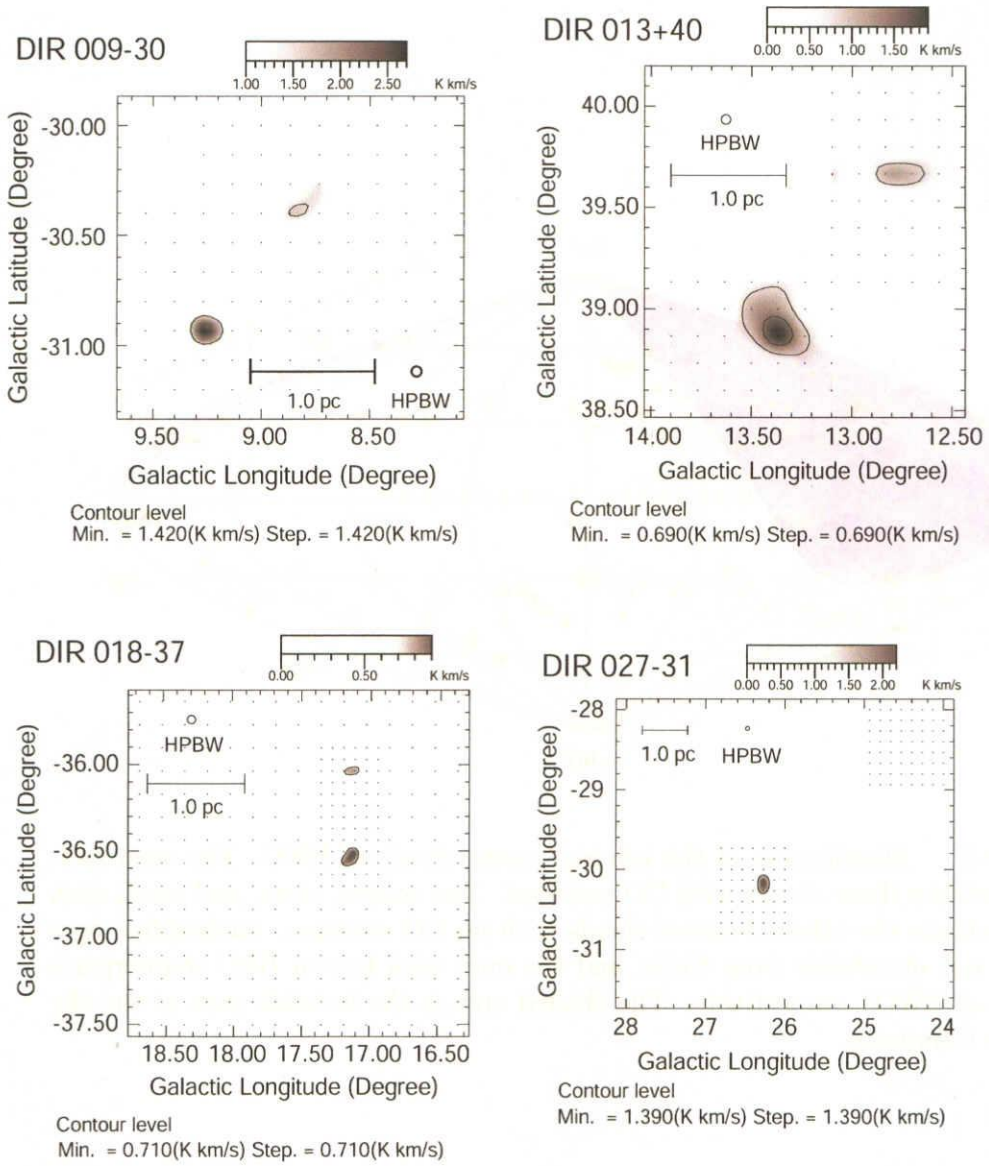

Figure 2–2. Velocity-integrated intensity map of ^{12}CO (J=1–0) associated with DIR clouds in Galactic coordinates. The name of the DIR cloud is shown to the left-top in each panel. Dots denote the observed positions. The lowest contour and the contour interval in each panel are 5σ of each region and they are shown to the bottom in that.

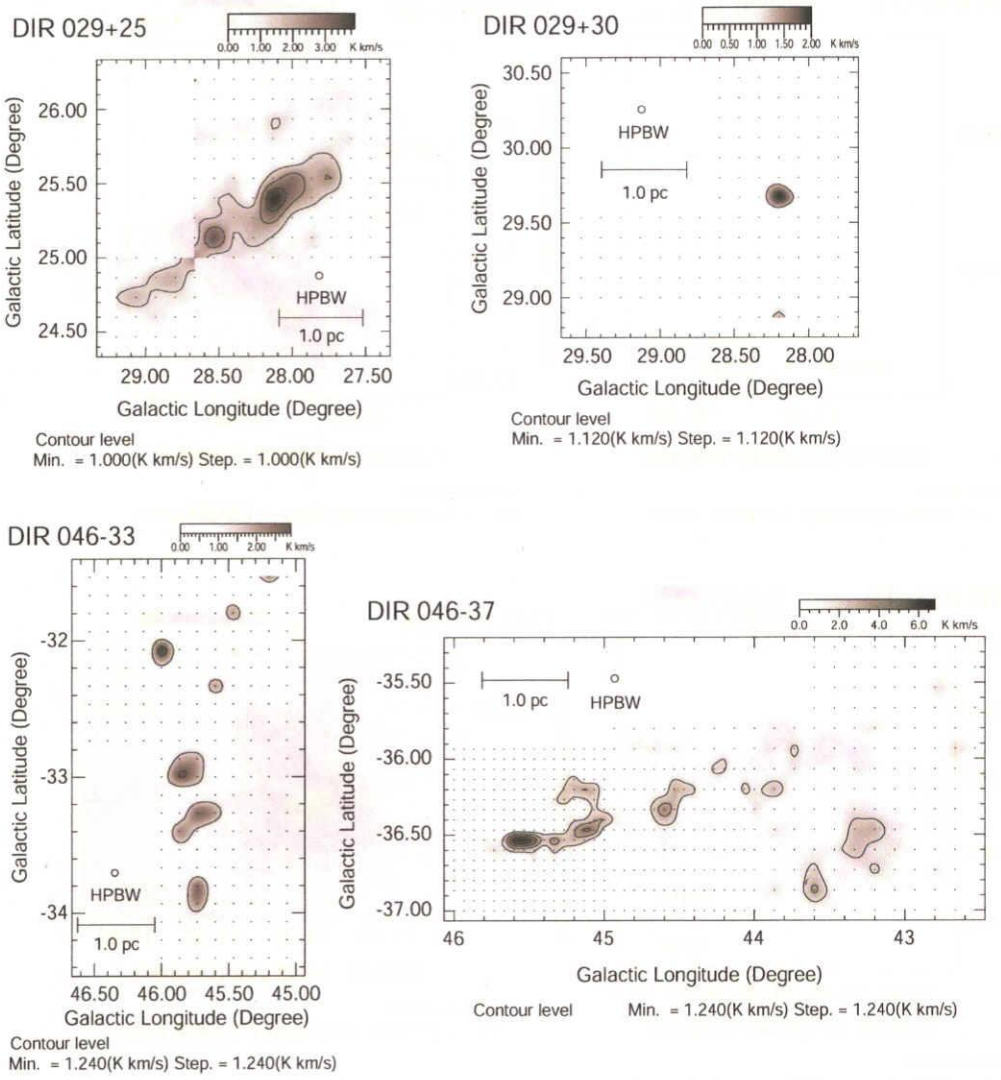

Figure 2–2. (Continued)

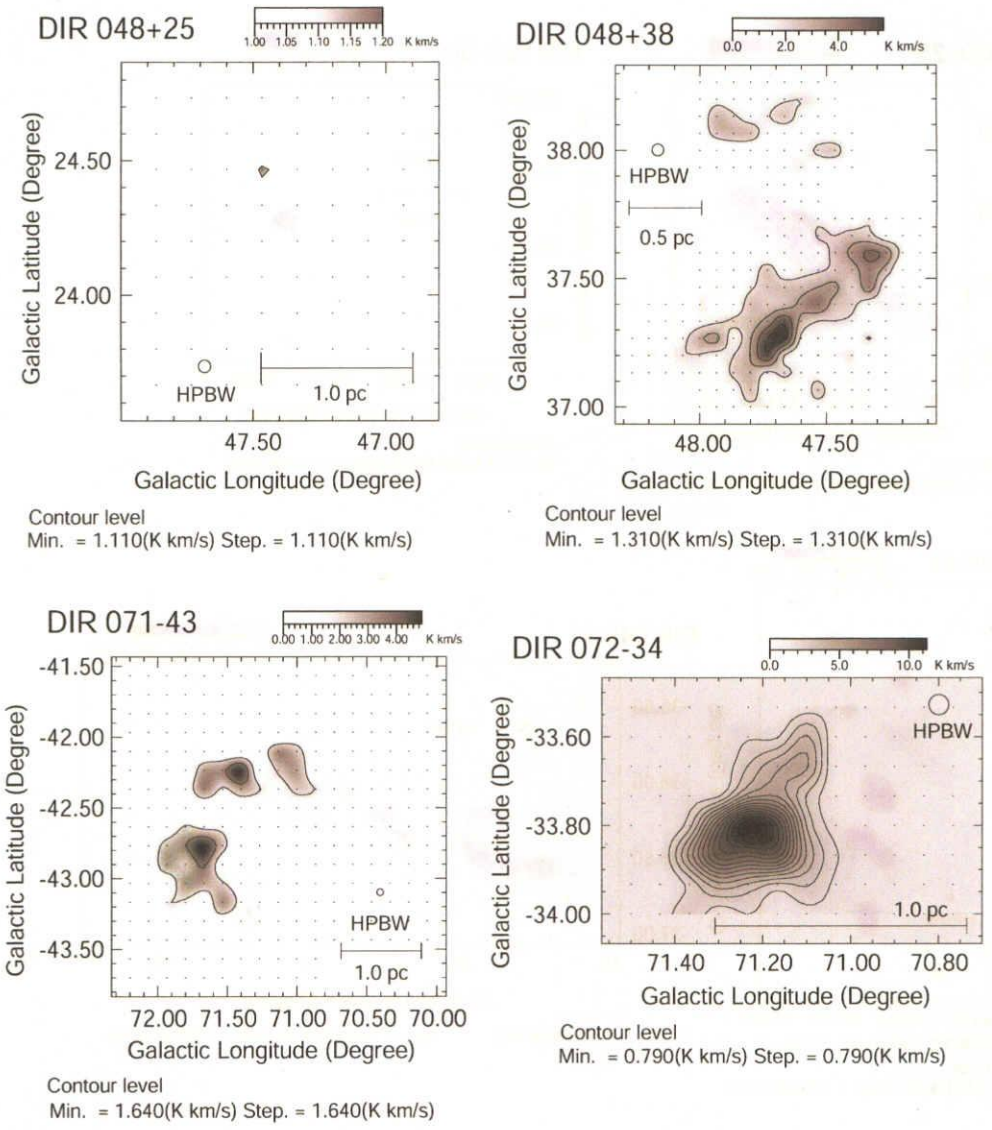

Figure 2–2. (Continued)

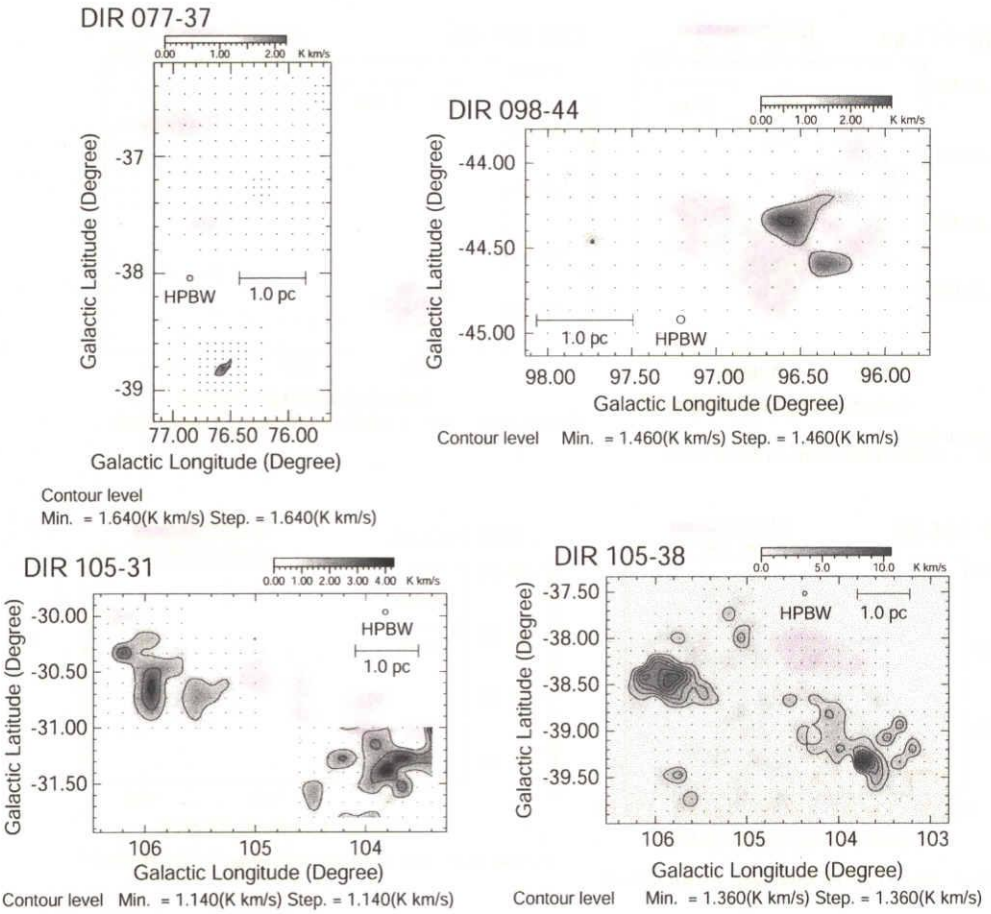

Figure 2–2. (Continued)

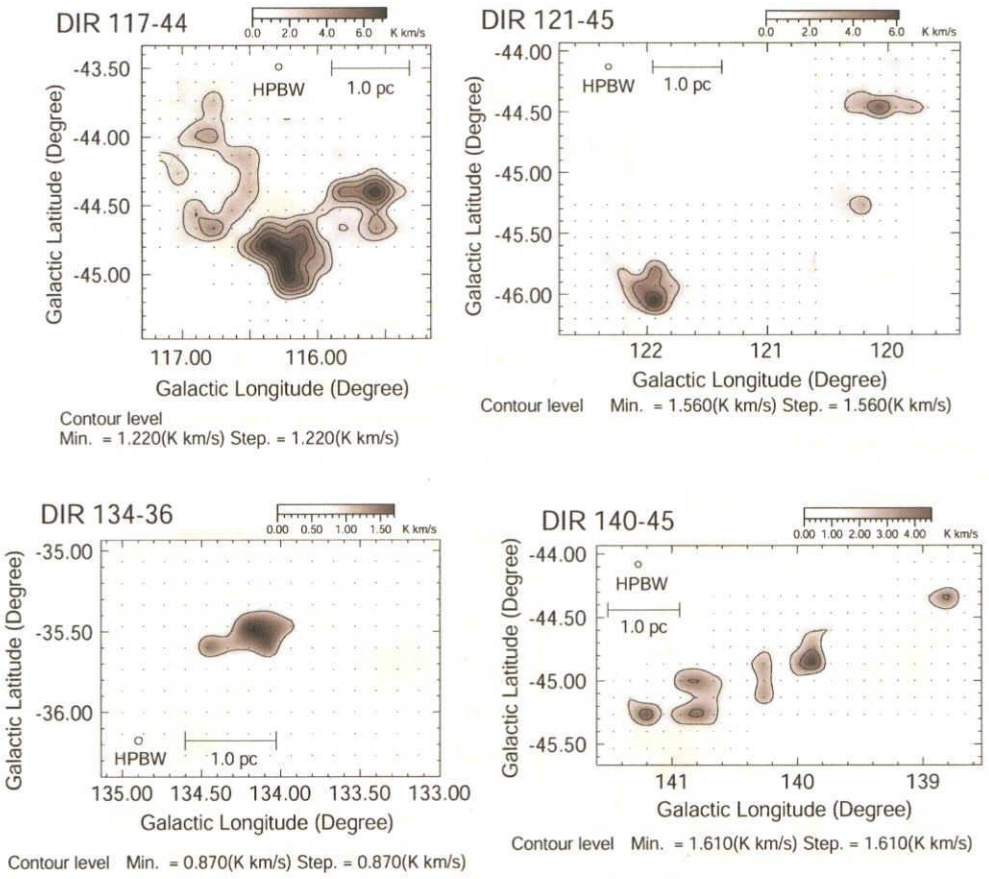

Figure 2–2. (Continued)

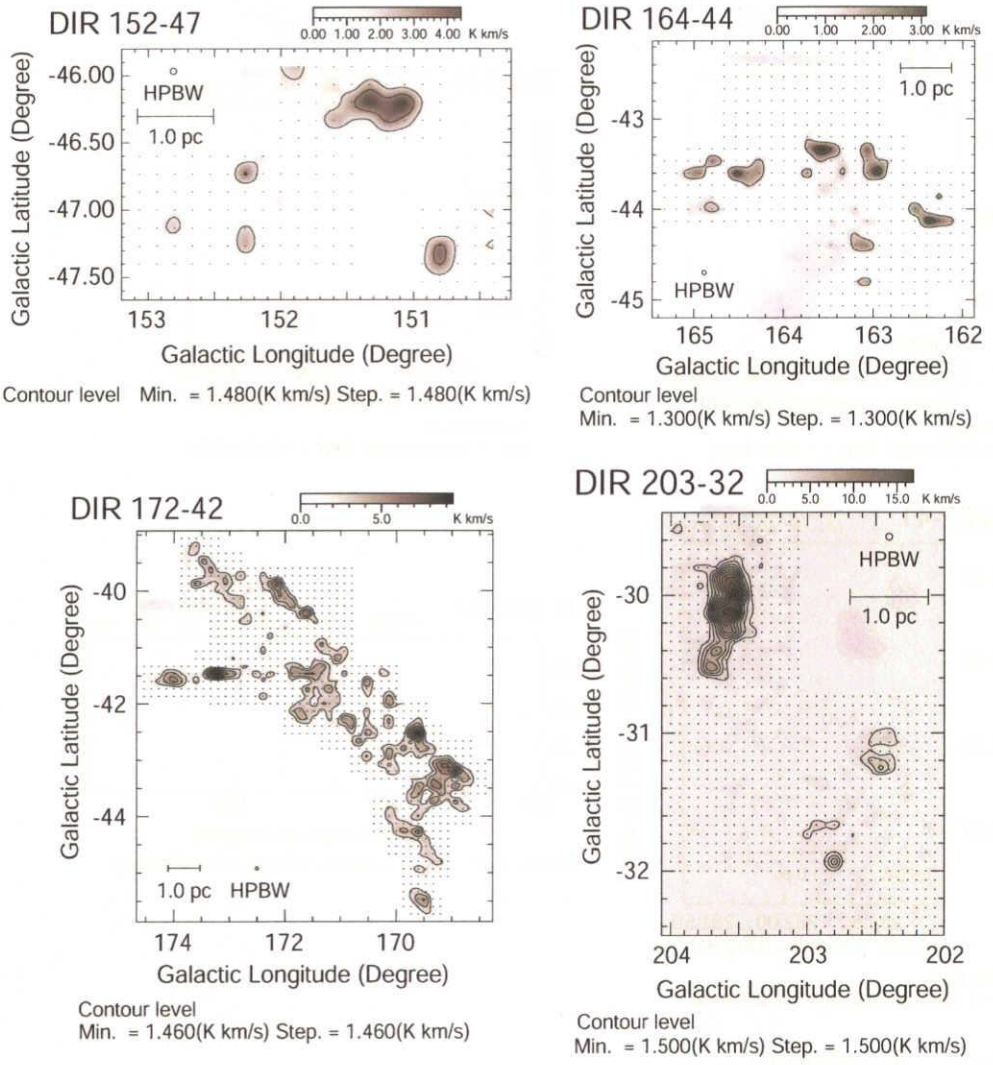

Figure 2–2. (Continued)

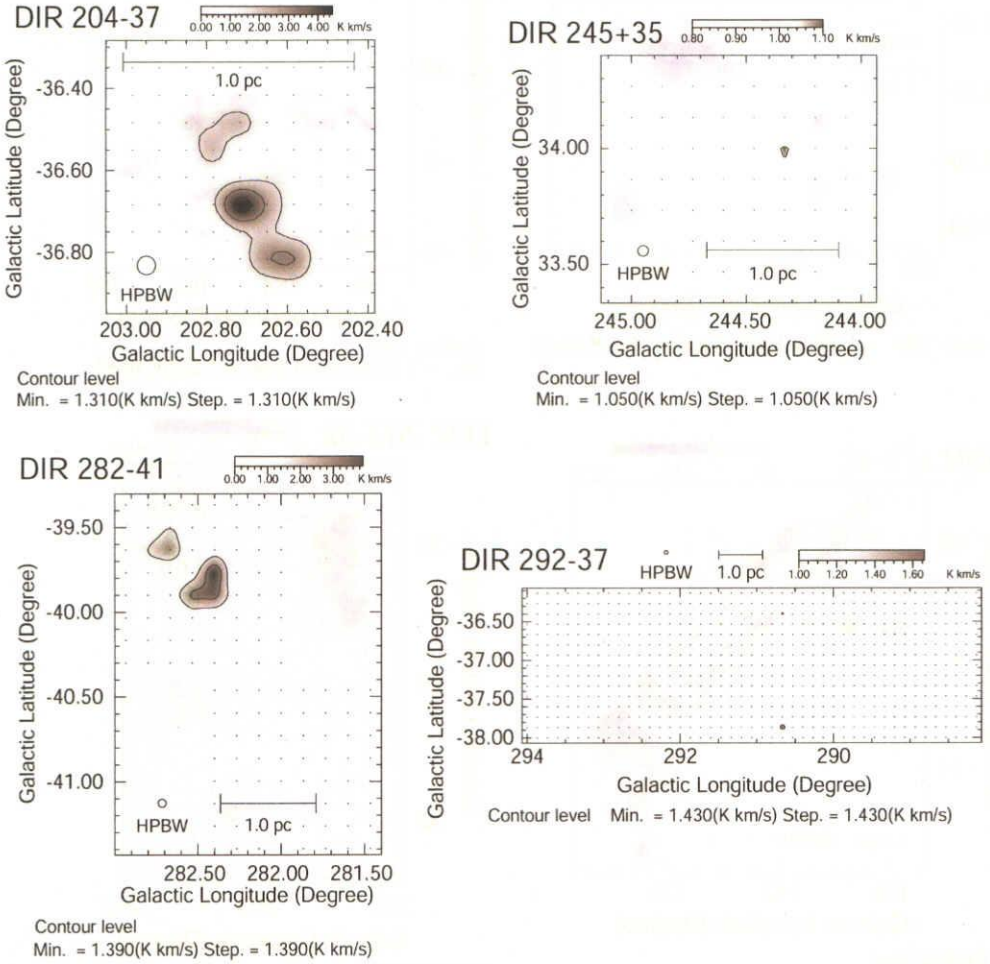

Figure 2–2. (Continued)

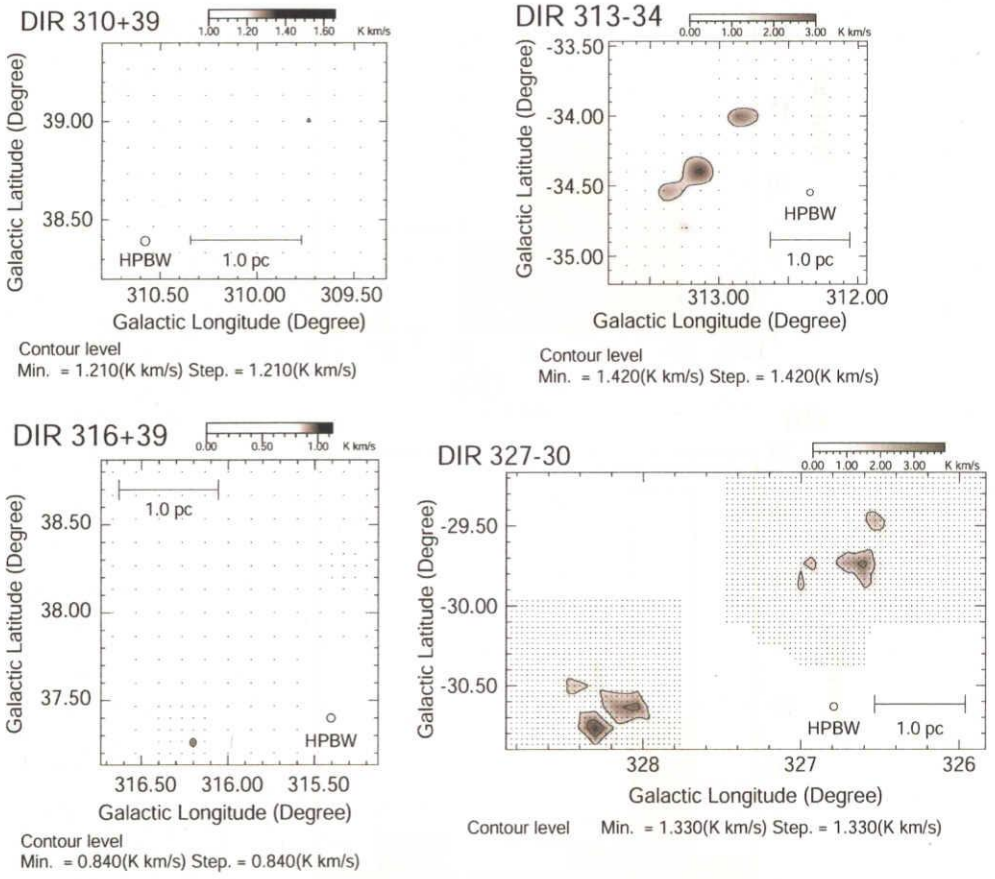

Figure 2–2. (Continued)

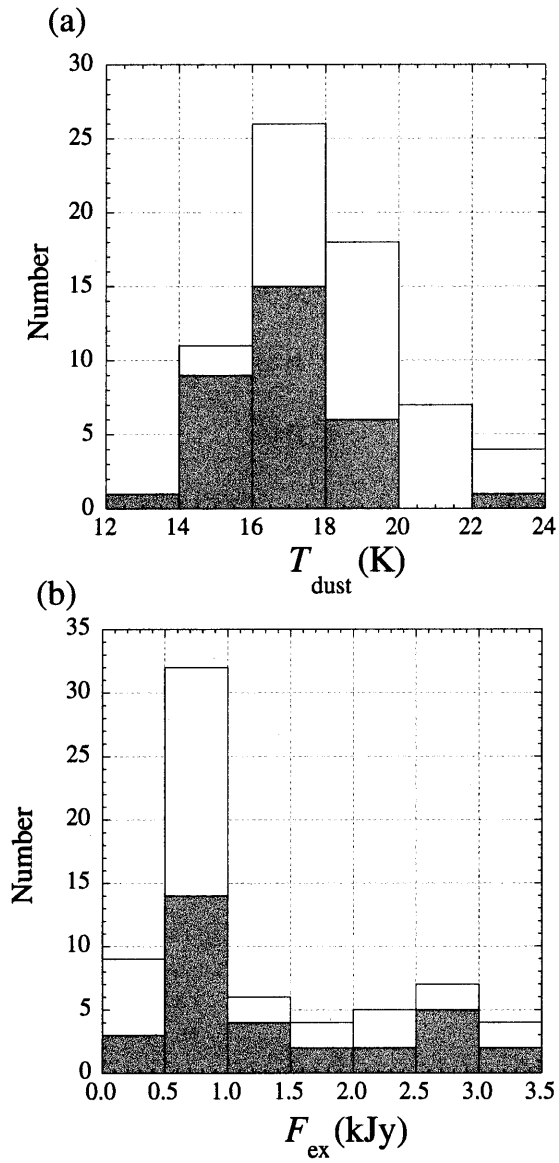

Figure 2–3. Histograms of (a) the dust temperature and (b) the total amount of excess of the infrared-excess clouds. The shaded area indicates those clouds with CO emission.

Chapter 3

HLCs In an HI Filament toward the MBM 53, 54, and 55 complex

Abstract

We carried out a CO survey of high galactic latitude molecular clouds toward an H I filament that contains a molecular cloud complex, MBM 53, 54, and 55, with the NANTEN telescope. Our observation covered the whole area of the H I filament in ^{12}CO (J = 1–0) with a 4′ grid spacing. The filament is found to consist of a number of clumpy molecular clouds, and we identified 110 ^{12}CO clouds in the region, whose total mass is estimated to be $\sim$1200 $M_{\odot}$. ^{13}CO (J = 1–0) observations were carried out toward the region of high ^{12}CO intensities in order to measure the optical depth of molecular gas. There is no detection in C^{18}O (J = 1–0) line in the observed region, indicating that there are no clouds dense enough to form stars in the near future. These observations spatially resolved the entire gas distribution of MBM 53, 54, and 55 for the first time, and we have found a massive cloud, HLCG 92−35, around (l, b) $\sim$ (92°, −35°) whose mass is $\sim$330 $M_{\odot}$, corresponding to $\sim$1/4 of the total mass. This CO cloud occupies a galactic western half of a circular H I cloud toward (l, b) = (93°.5, −35°.5), and the H I to CO mass ratio is estimated to be the largest in the observed region. The far-infrared excess over H I emission, which is a good indicator of an existence of molecular hydrogen, toward HLCG 92−35 is the largest in the observed region. The ratio of the luminosity of the infrared excess to CO mass is also significantly larger than those of the other clouds by a factor of $\sim$5. These facts indicate that HLCG 92−35 is a CO-forming molecular cloud, which is younger than the MBM clouds in terms of molecular cloud formation. Some past

explosive event has been suggested by Gir et al. (1994) toward the H I filament. Toward HLCG 92−35, the molecular gas distributed along the western edge of the H I cloud, which implies that the molecular gas may be formed by a compression of expanding H I shell.

Key Words : ISM: atoms — ISM: clouds — ISM: molecules — ISM: structure — stars: formation

3.1 Introduction

HLCs are usually surveyed and observed in the $J = 1$–0 line of $^{12}C^{16}O$ (hereafter CO), because the line is the strongest among the thermally or sub-thermally excited ones of all molecular species. However, even the strongest CO emission is observed to be faint, $T_R^* \sim$ a few K, toward HLCs. This has made spatially extensive observations with a high-spatial resolution quite difficult. Most of the cataloged clouds as HLCs in Magnani et al. (1996) were, however, mapped with coarse sample spacings of $\sim 30'$, or were observed only toward a few observed points. Because the Jeans-length of gas with $n(H_2) \sim$ a few $\times$ 100 cm^{-3} and $T \sim$10 K is estimated to be $\sim$1 pc, observations with a spatial resolution of $\ll 1$ pc are needed to investigate the physical properties of individual clouds and the dynamical state. Actually, the following high-resolution observations toward these HLCs showed that the distribution of molecular clouds shows smaller structures (e.g., Wouterloot et al. 2000), and then observations with higher spatial resolutions are definitely needed to investigate the physical properties of the molecular clouds. The result of the first survey was presented in previous chapter, detecting more than 30 new HLCs by observing infrared excess clouds over H I emission cataloged by Reach et al. (1998). The survey shows that the NANTEN can cover an extensive area with a relatively high-spatial resolution within a short time even toward the high latitude region.

From Bhatt 2000, it has found that the distribution of HLCs is not uniform and there are some groups or complexes of HLCs, whose angular extent is $\sim$10 degrees or larger. In order to pursue the mechanism of the formation of the cloud complexes, CO observations of the entire system with a high spatial resolution are needed. Studies of the large-scale HLC complexes with high spatial resolution have been rare, since the spatial extent is as large as tens of square degrees or more. Such studies ware carried out only by Heithausen & Thaddeus (1990) toward Polaris Flare, and by de Vries, Heihausen, & Thaddeus (1987) and Pound & Goodman (1997) toward Ursa Major clouds. They showed the detailed structure of the entire

molecular cloud system, and Pound & Goodman (1997) suggested that the origin of such structures could be some explosive events. Another HLC complex, MBM 53, 54, and 55, is one of the largest and most massive ones, a little smaller than Polaris Flare. Toward the complex, there is an H I filament whose angular length is as long as ~20 degrees, and the filament contains the MBM clouds. In the present study, we present the results of a CO mapping with NANTEN toward the H I filament that contains the high latitude molecular cloud complex of MBM 53, 54, and 55 regions.

MBM 53, 54, and 55 are cataloged and named by Magnani et al. (1985) and are located at $(l, b) \sim (92°.97, -32°.15)$, $(92°.97, -37°.54)$, and $(89°.19, -40°.94)$, respectively. The effective spatial resolution of the map is ~20′. A high-resolution strip line observation in MBM 54 and 55 was done by Sakamoto (2002) and the precise velocity structure was obtained. A molecular emission line observation toward a small portion of MBM 55 by high-density tracers was done by Reach et al. (1995).

The distance to the HLCs is estimated to be an order of ~100 pc because it lies at high Galactic latitude. Welty et al. (1989) measured strong interstellar Na I absorption towards 21 stars toward or near MBM 53, 54, and 55. They suggested that if the strong D line absorptions are associated with the molecular clouds, all three clouds are estimated to be at about 150 pc. We then adopt hereafter a distance of 150 pc for the complex.

A search for T Tauri stars is done by Hearty et al. (1999) and Li et al. (2000). Li et al. (2000) found a candidate for a T Tauri star around MBM 55. Kun (1992) observed Hα emission toward MBM 53, 54, and 55, detecting twelve candidates for emission-line stars. However, only one star is found to be a candidate for a weak-line T Tauri star toward MBM 55 by the follow-up observations (Martin & Kun 1996). These facts indicate that the cloud may have experienced star formation in the past. However, the association of younger stars, i.e., protostars, with the molecular clouds is not studied well, because of the absence of the high-resolution molecular map to be compared with the distribution of far-infrared sources.

H I emission at 21 cm is observed toward the region including MBM 53, 54, and 55 (Gir et al. 1994), and they found an H I filament, whose length is ~60 pc, which contains the molecular cloud complex. They claimed that this H I filament may be expanding from the reduction of the position-velocity map.

These interesting characters of the complex strongly led us to the present study. In the present paper, we will present the observational results of the survey toward the complex covering the H I filament in the lines of ^{12}CO ($J = 1$–0), ^{13}CO ($J = 1$–0) and C^{18}O ($J = 1$–0). The main purpose of the survey is to probe an evolutionary status of the molecular clouds in a same complex with a relatively high spatial

resolution. The details concerning the observational procedures are described in section 3.2. In section 3.3, we give the results of our observations. The results are discussed in section 3.4.

3.2 Observations

Observations were carried out in the $J = 1$–0 lines of ^{12}CO, ^{13}CO, and C^{18}O (rest frequencies of 115.271204 GHz, 110.201353 GHz, and 109.782182 GHz, respectively) with the NANTEN telescope.

The observed region was ~141 square degrees toward $82° \lesssim l \lesssim 98°$ and $-45° \lesssim b \lesssim -29°$. To begin with, the observations in ^{12}CO were made in Galactic coordinates at a grid spacing of $8' \times \cos(b)$ in galactic longitude and $8'$ in galactic latitude. Then, we observed the region where the ^{12}CO emission had been significantly detected at a grid spacing of $4' \times \cos(b)$ in galactic longitude and $4'$ in galactic latitude. Next, we observed the position of strong ^{12}CO emission in ^{13}CO. If the ^{13}CO emission exists at the edge of the map, we extended the observations until the emission becomes undetectable. Furthermore, we also observed C^{18}O line at the positions of intense ^{13}CO emission. The observations of ^{13}CO and C^{18}O were made at a grid spacing of $2' \times \cos(b)$ in galactic longitude and $2'$ in galactic latitude. The periods of observations were several sessions between 2001 June to 2002 February. All the observations were made by frequency switching method whose interval is 15 MHz, corresponding to ~38 km s^{-1}. The observation was performed by using an acousto-optical spectrometer of narrow band. The detailed parameters of the NANTEN telescope are descraibed in section 1.4. Total number of points observed in ^{12}CO, ^{13}CO, and C^{18}O were 15628, 5687, and 378, respectively. The integration times per point for ^{12}CO, ^{13}CO, and C^{18}O were typically ~30 s, ~20 s, and ~200 s, resulting in typical rms noise temperatures per channel of ~0.5 K, ~0.21 K, and ~0.07 K in the abusolute antenna temperature, $T_{\rm R}^{*}$, respectively. In reducing the spectral data, we subtracted forth-order polynomials for the emission-free parts in order to ensure a flat spectral baseline. The observation was performed by frequency swithing mode and by using an acousto-optical spectrometer of narrow band.

We employed a room-temperature chopper wheel for the intensity calibration (Kutner & Ulich 1981). An absolute intensity calibration was made by observing Orion KL [$\alpha(1950) = 5^{\rm h}32^{\rm m}47.^{\rm s}0$, $\delta(1950) = -5°24'21''$] for ^{12}CO and ^{13}CO and ρ Oph East [$\alpha(1950) = 16^{\rm h}29^{\rm m}20^{\rm s}.9$, $\delta(1950) = -24°22'13''$] for C^{18}O and we observed them every 2 hours. We assumed the $T_{\rm R}^{*}$ of Orion KL to be 65 K for ^{12}CO and 10

K for ^{13}CO and ρ Oph East to be 4.4 K for $C^{18}O$.

3.3 Results

3.3.1 ^{12}CO

3.3.1.1 Large Scale Distribution of ^{12}CO Clouds

Out of the 15628 observed positions, significant ^{12}CO emission with an integrated intensity greater than 1.5 K km s^{-1} (5σ) was detected toward the 3164 positions. Figure 3–1 shows the spatial distribution of the velocity-integrated intensity of ^{12}CO. The region surrounded by block borders shows the observed region in ^{13}CO. ^{12}CO clouds are distributed along an arc-like filament having a length of $\sim$40 pc. The filamentary structure is made up of small clumpy clouds, and the radius of each small cloud is measured to be less than 0.5 pc. Molecular clouds toward (l, b) $\sim$ (92°.97, $-$32°.15), (92°.97, $-$37°.54), and (89°.19, $-$40°.94) corresponds to MBM 53, 54, and 55 detected by Magnani et al. (1985), respectively. We newly detected a large molecular cloud, whose size is comparable to MBM 54 and 55, toward 91° $\lesssim l \lesssim$ 94° and $-$36° $\lesssim b \lesssim$ $-$33°(hereafter, HLCG 92$-$35). The LSR velocity of most of the ^{12}CO clouds is in a range from $-$11 km s^{-1} to 0 km s^{-1}.

We calculated the molecular mass, $M(^{12}\mathrm{CO})$, at a distance, D, by adopting the formula

$$M(^{12}\mathrm{CO}) = \mu m_{\mathrm{H}} \Sigma [D^2 \Omega N(\mathrm{H_2})], \tag{3.1}$$

where Ω is the solid angle subtended by the effective beam size $4' \times 4'$, m_{H} is the mass of a hydrogen, and μ, the mean molecular weight, is assumed to be 2.8 by taking into account a relative helium abundance of 25% in mass. $N(\mathrm{H_2})$ is the molecular hydrogen column density and is derived by assuming a conversion factor from the ^{12}CO intensity of 1.0 $\times 10^{20}$ cm^{-2}/(K km s^{-1}). Summation is performed over all the positions observed within 5σ level contours to derived the total cloud mass. The total mass of the ^{12}CO clouds was estimated to be $\sim$1200 $M_{\odot}$.

3.3.1.2 Individual Clouds

We present here the properties of individual molecular clouds. A ^{12}CO cloud is defined as a collection of more than two contiguous observed positions such that the integrated intensity at each position exceeds 1.5 K km s^{-1} (5σ). Based on this definition, 108 individual clouds have been identified. For these 108 clouds, the maximum brightness temperature, $T_{\mathrm{R}}^{*}(^{12}\mathrm{CO})$ and the FWHM line width, ΔV, derived from single Gaussian fitting, range from 0.8 K to 8.3 K and 0.7 km s^{-1} to

7.8 km s^{-1}, respectively. The radius of a cloud, R, is defined as the radius of an equivalent circle having the same area, i.e., $R(\mathrm{pc}) = \sqrt{A/\pi}$, where A is the total cloud surface area within the 5σ contour level, ranges from 0.14 pc to 2.57 pc. HLCG 92−35 has the mass of 326 $M_\odot$ and R of 2.57 pc, and is the largest and most massive molecular cloud in the present observed area. These physical propterteis of molecular clouds are listed in Table 3–1.

3.3.2 ^{13}CO and C^{18}O Observations

3.3.2.1 Large Scale Distribution of ^{13}CO Cloud

Out of the 5687 observed positions, significant ^{13}CO emission with an integrated intensity greater than 0.33 K km s^{-1} (5σ) was detected toward 461 positions. Figure 3–2 shows a spatial distribution of the velocity-integrated intensity of ^{13}CO. Filled circles show the points observed in C^{18}O. The distribution of ^{13}CO emission is found to be very clumpy. Basically, the ^{13}CO emission traces the high-intensity regions in ^{12}CO. However, ^{13}CO emission toward HLCG 92−35 is weaker than MBM 54 and 55 by a factor of 2 in spite of the similar ^{12}CO intensities of the three clouds, and the distribution of ^{13}CO emission in HLCG 92−35 shows smaller and more clumpy structure (see the discussion in section 3.4.3).

We also observed C^{18}O emission toward the positions of strong ^{13}CO detection (see Figure 3–2). But we could not detect C^{18}O emission toward any of these observed points at the rms noise fluctuations of ∼0.07 K (T_{R}^*).

3.3.2.2 Individual Clouds

A ^{13}CO cloud is defined as the same as the ^{12}CO clouds is, a collection of more than two contiguous observed positions such that the integrated intensity at each position exceeds 0.33 K km s^{-1} (5σ). We identified 70 ^{13}CO clouds. Tables 3–2 and 3–3 give the observed properties and the derived physical properties of the ^{13}CO clouds, respectively. In Table 3–2, the runnnig number is given in column (1). The positions are given in Galactic coordintes in columns (2) and (3). Columns (4–6) list absolute peak antenna temperature, T_{R}^* [K], FWHM line width, ΔV [km s^{-1}], and the velocity with respect to the local standard of rest, V_{LSR} [km s^{-1}], measured at the peak intensity position of the cloud by a Gaussian fitting, Column (7) gives the ^{13}CO integrated intensity [K km s^{-1}] at the peak. In Table 3–3, the running number is given in column (1). Column (2) lists column density of H_2, $N(H_2)$ [cm^{-2}]. Column

(3) lists FWHM line width of composite spectrum of the cloud by a Gaussian fitting, $\Delta V_{\rm comp}$ [km s^{-1}]. Column (4) lists radius, R [pc]. Column (5) lists the mass assuming that rotational levels of a ^{13}CO molecule are in local thermodynamic equilibrium (LTE), $M_{\rm LTE}$ [$M_\odot$]. Column (6) lists the mass assuming that the cloud is under the virial equilibrium, $M_{\rm vir}$. Column (7) lists the optical depth of ^{13}CO, $\tau(^{13}{\rm CO})$.

Definition of radius is the same as that of ^{12}CO (see section 3.1.2). We calculated the ^{13}CO column densities, $N(^{13}{\rm CO})$, by assuming the local thermodynamic equilibrium (LTE) condition with an excitation temperature, $T_{\rm ex}$, of 8.7K for all observed points. $T_{\rm ex}$, 8.7K, was derived from ^{12}CO observation with NANTEN under the assumption that the ^{12}CO emission toward the most intense region is optically thick. The optical depth of ^{13}CO, $\tau(^{13}{\rm CO})$, was calculated by using the following equation:

$$\tau(^{13}{\rm CO}) = \ln\left[1 - \frac{T_{\rm R}^{*}(^{13}{\rm CO})}{5.29}\left\{\frac{1}{\exp(5.29/T_{\rm ex}) - 1} - 0.164\right\}^{-1}\right]. \qquad (3.2)$$

The ^{13}CO column density, $N(^{13}{\rm CO})$, was estimated by

$$N(^{13}{\rm CO}) = 2.42 \times 10^{14} \times \frac{\tau(^{13}{\rm CO}) T_{\rm ex}({\rm K}) \Delta V({\rm km\ s^{-1}})}{1 - \exp[-5.29/T_{\rm ex}({\rm K})]}({\rm cm^{-2}}). \qquad (3.3)$$

The ratio $N({\rm H_2})/N(^{13}{\rm CO})$ was assumed to be 7×10^5 (Dickman 1978). The LTE mass of clouds was derived by the same as ^{12}CO (see equation (3–1)). The radius, column density and LTE mass range from 0.07 pc to 0.74 pc, 7.0×10^{20} cm^{-2} to 2.8×10^{21} cm^{-2} and 0.2 $M_\odot$ to 94.3 $M_\odot$, respectively. The virial mass, $M_{\rm vir}$ of a cloud was derived by using the following equation, assuming isothermal, spherical, and uniform density distribution with no external magnetic pressure: $M_{\rm vir} = 209 \times R \times \Delta V_{\rm comp}^2$, where R and $\Delta V_{\rm comp}$ are the radius (pc) and line width (km s^{-1}) of the composite profile obtained by averaging all of the spectra within the cloud, respectively (for details of the line width of composite profiles, see Yonekura et al. 1997; Kawamura et al. 1998).

3.4 Discussion

3.4.1 Physical Properties of the Molecular Clouds

The velocity-integrated intensity map of the complex shows that it is highly clumpy, or there are a lot of small-scale structures. Apparently, the map is quite

different with that in Magnani et al. (1985) because of the difference in spatial resolution, indicating that observations with a relatively high spatial resolution of $<$ 10 arc minutes are definitely needed to investigate the physical properties of HLCs. Actually, the observation with higher spatial resolutions revealed much smaller fluctuations, $\lesssim$ 0.1 pc, toward some HLCs (e.g., Pound et al. 1990; Wouterloot et al. 2000), although the present observation seems to resolve the individual clouds that are separated at the 5σ intensity level. The boundary of MBM 53, 54, and 55 is rather vague in the present ^{12}CO map; MBM 53 seems to be only a fragment of molecular cloud in the H I filament and there is no clear difference with the other fragments.

HLCG 92−35 was newly detected in this survey. Although this cloud is the largest ^{12}CO cloud in this complex, it is interesting that the cloud has been missed in the previous study. MBM 53, 54, and 55 were found by observations toward optical obscurations (Magnani et al. 1985), indicating that this type of survey can miss a large amount of molecular gas.

The mass spectra of the ^{12}CO and ^{13}CO clouds are shown in Figure 3–3. The spectra have been fitted by the maximum-likelihood method (Crawford et al. 1970), and it is found that they are represented by a power law as follows: $dN/dM \sim M^{-1.73\pm0.08}$ for ^{12}CO and $dN/dM \sim M^{-1.65\pm0.12}$ for ^{13}CO. These spectrum indices are similar to that which has been derived in other regions (e.g., Kawamura et al. 1999; Yamaguchi et al. 1999; Kramer et al. 1998). It is to be noted that the mass spectrum for ^{13}CO clouds is fitted rather poorly, indicating that the mass spectrum may not be represented by a single-power law.

Figure 3–4 illustrates the correlation diagram between $M_{\rm LTE}$ and $M_{\rm vir}$ for ^{13}CO clouds. Although the present ^{13}CO clouds tend to be more virialized as the mass increase, the virial mass of the present ^{13}CO clouds is calculated to be one or two order larger than LTE one for all the clouds. This is a typical property of HLCs; filled triangles in Figure 3–4 represent MBM 12 from Pound et al. (1990). The ratio $M_{\rm vir}/M_{\rm LTE}$ is found to be a nice indicator of the possibility of star formation in a cloud (e.g., Tachihara et al. 2000). The ratio tends to be $\sim$1 for ^{13}CO clouds with C^{18}O cores in Ophuichus north region (filled circles), which are considered to be close to star formation phase, and the ^{13}CO clouds without C^{18}O cores (open circles) have a little bit larger ratio. Although the present ^{13}CO clouds tend to be more virialized as the mass increase, even the most massive cloud is far from the virial equilibrium, which is typical in HLCs (e.g., Zimmermann et al. 1990). This fact implies that the star formation will not occur in the present ^{13}CO clouds in the near future when we see their dynamical state.

3.4.2 Star Formation

3.4.2.1 Past Star Formation

As mentioned in introduction, there are two candidates for weak line T Tauri stars in the observed region. Figure 3–5 shows the distribution of the candidates (Martin & Kun 1996; Li et al. 2000) superposed on the ^{12}CO integrated intensity contour map. One of the T Tauri stars, 1RXS J231019.1+144711, shows weak Li I absorption, and therefore, the age is estimated to be an order of 10^6 yr (Li et al. 2000). As suggested by Li et al. (2000), there is a possibility that this star is formed in MBM 55. This indicates that the molecular cloud complex may have formed stars in the past, although the star formation activity has been quite low during this $\sim 10^7$ yr.

3.4.2.2 Present Star Formation

In order to examine the present star formation, we used the following criteria to choose candidates for protostars from IRAS point sources : (1) point sources detected at all four bands (12 μm, 25 μm, 60 μm, and 100 μm) with a data quality flag more than 2 and (2) flux ratios at 25 μm and 60 μm satisfying $\log(F_{25}/F_{60}) < 0$, where F_λ is a flux density at wavelength λ. At high latitude, since a possibility of overlapping with other astronomical objects is quite low, the good association of the cold objects with molecular clouds indicates that they are protostars formed in the cloud. We found the 4 IRAS sources towards these molecular clouds, but no sources were associated them (see Figure 3–5). The detection limit of IRAS point sources at 150 pc is $< 0.1\ L_\odot$ (Myers et al. 1987). This implies that stars of $\sim$ a solar mass or more are not formed at present in the complex.

We observed C^{18}O line toward high-intensity part of the ^{13}CO clouds with an rms noise of as low as 0.07 K (T_R^*), but we could not detect the emission at any of the observed points. This means that there are no high-density gas of $\sim 10^4$ cm^{-3} in this region, indicating that the star formation will not occur in the near feature of $\sim 10^6$ yr, although there is a plenty of molecular gas to form many stars in the complex.

3.4.3 Evolutionary Status of the Complex

As suggested in section 3.4.2, there is no dense core whose density is high enough to lead a near-future star formation toward the complex. Since the number of T

Tauri stars is only ~2, quite small compared with the cloud mass, it may be unlikely that the complex had a high-star formation activity in the past which leads to a cloud dissipation and/or compression. However, there is a large amount of gas of 1200 $M_{\odot}$ as a reservoir for star formation in the complex at present, and there is still a possibility that star formation will occur in the future. The low-column density of the complex implies that most part of the complex is exposed to the external far-UV radiation, and the observations of other components, i.e., dust and H I, are an important. Here, we investigate the evolutionary status of the complex by comparing the present molecular data with the other wavelength data.

Figure 3–6 illustrates the velocity-integrated intensity map of H I emission toward the complex taken from a Leiden-Dwingeloo H I survey (Hartmann & Burton 1997) whose half-power beam width and angular resolution are 35′.2 and 30′, respectively. The velocity range over which we integrated is from -11 km s^{-1} to 0 km s^{-1}, corresponding to the velocity range of ^{12}CO spectra. Because the spatial resolution of ~30′ is coarser than that of CO observation by a factor of ~10, we discuss here only the overall comparison between CO and H I distribution. The ^{12}CO intensity is overlaid with the H I map. Overall distribution of H I and ^{12}CO emission is similar; the molecular emission basically traces the high-intensity region of H I emission. Toward some regions, such as HLCG 92−35, and H I clouds at (l, b) ~ (82°, −43°), (87°, −34°), and (90°, −30°), the H I distribution is not well coincident with CO ones. We will discuss this matter later in this section.

Figure 3–7 shows an integrated intensity map of ^{12}CO supurposed on IRAS 100 μm image from IRAS Sky Survey Atlas (ISSA). The distribution of the dust emission toward the complex is very similar to that of ^{12}CO. The strongest dust emission comes from the position of HLCG 92−35. There is, however, major exception of the good coincidence; the filamentary or arc-like feature which extends along −37°.5 in galactic latitude. Figure 3–8 illustrates the H I intensity map of the same area as that in Figure 3–6, with a different integrated velocity range from -20 km s^{-1} to -12 km s^{-1}. There is another arc-like feature which is obviously different from that in Figure 3–6, although the integrated intensity of H I is weaker than that toward the complex including HLCG 92−35, MBM 53, 54, and 55. The feature coincides well with the dust arc-like feature showing no CO emission along −37°.5 in galactic latitude. This indicates that this arc-like dust emission comes from the different region of the CO clouds in the same line of sight, suggesting that there are two cloud components toward this region; one is a CO emitting cloud of $-11 < V_{LSR} <$ 0 km s^{-1}, and another is no-CO emitting cloud which can be detected only by H I and IRAS. Hereafter, we use therefore the velocity integrated intensity map of H I

with $-11 < V_{LSR} < 0$ km s^{-1}, when we compare the CO distibution with the H I distribution.

The comparisons among ^{12}CO, ^{13}CO, H I, and dust emissions indicate that the HLCG 92−35 has different and interesting properties compared with the other clouds; H I and IRAS emission are the strongest while the CO optical depth is small. Hereafter, we discuss the quantitative physical properties of HLCG 92−35 by comparing with those of the other clouds.

First, we shall present an enlarged view toward HLCG 92−35 in Figure 3–9(a) and toward MBM 55 in Figure 3–9(c) for a comparison with the same contours and color levels. As mentioned above in this section, the CO distribution doesn't resemble that of H I toward HLCG 92−35, contrary to the case toward MBM 55. Toward (l, b) = (93°.5, −35°.5), there is a circular H I cloud whose spatial extent is 4° × 4°, and the H I cloud includes HLCG 92−35 newly detected in ^{12}CO. The size of the H I cloud is measured to be ∼5 pc, and the mass is estimated to be ∼590 $M_{\odot}$ under the assumption of H I intensity-mass conversion factor of 1.823 × 10^{18} cm^{-2}/(K km s^{-1}). HLCG 92−35 is located at the galactic western part of the H I cloud, and the CO intensity toward the galactic eastern half is nearly the detection limit or lower (hereafter the "west" and "east" are in Galactic coordinates). Although the HLCG 92−35 almost coincides with the position of the peak intensity position of the H I cloud, the H I intensities of western and eastern halves of the H I cloud are similar within a factor of 1.1, i.e., the intensity contrast is not so large in the center part of the H I cloud. The west and east ones are divided along the dotted line in Figure 3–9(a). The CO/H I mass ratio of the western half of 0.97 is calculated to be much larger than that of the eastern half of 0.10 by a factor of ∼10. This result indicates that evolutionary status is not uniform in a single H I cloud, and the western half is considered to be more evolved in terms of molecular cloud formation.

Next, we shall compare the physical properties of the three clouds with a similar ^{12}CO intensity, HLCG 92−35, MBM 54, and MBM 55. Table 3–4 shows the comparison of physical properties among HLCG 92−35, MBM 54, and MBM 55 toward the region whose intensity is more than 6.0 K km s^{-1} in ^{12}CO. The cloud name is given in column (1). Column (2) lists the area whose intensity is more than 6.0 K km s^{-1} in ^{12}CO. Column (3) lists the LTE mass derived from ^{13}CO. Column (4) lists the ratio of mass derived from H I to that derived from ^{13}CO intensity. Column (5) lists the ratio of the luminosity of infrared excess, $L_{\rm Iex}$, to the LTE mass derived from ^{13}CO. Column (6) lists the ratio of the $E(B-V)$ luminosity, $L_{\rm E(B-V)}$, calculating from $E(B-V)$ derived by Schlegel et al. (1998), to the LTE mass derived from

^{13}CO. The infrared excess is defined to be

$$I_{\rm ex} = I_{100} - SN({\rm H\,I}) - {\rm O}. \tag{3.4}$$

S is the locally interpolated slope of the infrared-H I correlation. The offset O contains residual zodiacal light and the cosmic infrared background. We used 0.62 MJy sr^{-1}/(10^{20} cm^{-2}) for S and 0.76 MJy sr^{-1} for O derived by Reach et al. (1998). The luminosity of the infrared excess, $L_{\rm I_{ex}} = \sum(F_{\rm I_{ex}}\Omega)$, where $F_{\rm I_{ex}}$ is the flux density of the infrared excess and the unite is MJy sr^{-1} and Ω is the solid angle, is the sum of the infrared excess toward the region detected more than 6.0 K km s^{-1} in ^{12}CO and the unite is MJy sr^{-1} pc^2. The luminosity of $E(B-V)$, $L_{\rm E(B-V)} = \sum(E(B-V)\Omega)$, is the sum of $E(B-V)$ within the same region as that of the infrared excess and the unite is mag pc^2.

One of the significant difference of HLCG 92−35 from the other clouds is the weakness of ^{13}CO intensity, i.e., small optical depth of CO. This leads to the largest ratio of $M_{\rm H\,I}$ to $M_{\rm ^{13}CO}$ compared with the other two clouds by a factor of $\sim 4-5$, indicating that HLCG 92−35 is an H I-rich cloud compared with the amount of CO.

The luminosity of $E(B-V)$ to LTE mass ratio in HLCG 92−35 is larger by a factor of ∼4 compared with MBM 54 and 55. Since the infrared emission is the strongest toward HLCG 92−35 from Figure 3–7, this indicates that the amount of dust toward HLCG 92−35 is most abundant. This result implies that the ratio of CO to total gas (molecular + atomic) in HLCG 92−35 is smaller than that of the other typical HLCs such as MBM 54 and 55.

Finally, we look into the luminosity of infrared excess. If we assume that the amount of dust is proportional to that of the atomic hydrogen plus hydrogen molecule, and that the radiation field, gas-to-dust ratio, and the temperature are uniform throughout the entire region, the amount of the infrared excess is expected to be proportional to that of hydrogen molecule (see e.g., Reach et al. 1998). We used it as one index of measuring the quantity of a hydrogen molecule because the direct measurement is very difficult because of the zero permanent dipole moment. Figure 3–10 shows the distribution of the infrared excess toward the observed region. The infrared excess is calculated by using IRAS 100μm data by ISSA and H I data by Hartmann & Burton (1997). The spatial resolution of the map is therefore ∼30 $'$. Because a map of ISSA represents continuum, i.e., it integrates all the emission in the same line of sight, we use the total velocity integrated intensity for H I for the calculation of the infrared excess. Overall distribution of the infrared excess is more similar to that of CO compared with those of H I and IRAS (see also Figures

3–9(b) and 3–9(d)). For example, a holizontal filament at $b \sim -37°.5$ seen in the IRAS map is absent in this map, and H I clouds at (l, b) $\sim$ (82°, −43°), (87°, −34°), and (90°, −30°) showing poor correlation with CO become weak, strengthening the fact that the infrared excess is a good indicator of a molecular cloud.

The infrared excess toward HLCG 92−35 is estimated to be higher than that toward the other regions. The luminosity of the infrared excess to LTE mass ratio in HLCG 92−35 is also larger by a factor of ∼4 compared with MBM 54 and 55. The cause of the infrared excess is generally explained as the existence of hydrogen molecule, and/or high dust temperature as mentioned above. The average dust temperatures derived by Schlegel et al. (1998) are estimated to be 16.6, 16.7, and 16.7 K toward HLCG 92−35, MBM 54, and MBM 55, respectively. The temperature toward HLCG 92−35 is almost the same as other clouds, indicating that the cause of the infrared excess is not due to high temperature. Therefore, the large infrared excess toward HLCG 92−35 is considered to reflect the amount of hydrogen molecule.

To summarize the properties of HLCG 92−35, the ratio of the CO luminosity to the amount of atomic and molecular hydorogen is significantly smaller by a factor of ∼5 compared with the other clouds, although the ratio of molecular hydorogen to atomic one is almost the same as those of the other clouds. The low CO intensity is considered to be due to either low abundunce of CO or sub-thermal excitation of CO. The low abundance of CO can be explained by the fact that CO is dissociated by external far-UV radiations or that the cloud is young in terms of the evolutionary status in molecular cloud formation. Because the optical depth of dust toward HLCG 92−35 is the largest in the present region, it is unlikely that the CO in the cloud is more exposed to far-UV radiations compared with the other clouds with low dust optical depth. Therefore, the question is whether it is possible to observe an evolutionary stage of H_2 cloud without CO molecule or not. Lee et al. (1996) calculated the time dependent chemistry in inhomogeneous interstellar clouds exposed by interstellar far-UV field from one side of a cloud. They argued that most of the atomic hydrogen is converted to molecular one at a time scale of $\sim 10^6$ yr at $A_v \sim$ a few. The fractional abundance of CO at that time is an order of magnitude lower than that at steady state. The formation of CO at the A_v range reaches almost steady state in $\sim 10^7$ yr, i.e., the ratio $N(H_2)/N(CO)$ becomes constant after this phase. This means that the stage of a H_2 cloud without CO can survive up to $\sim 10^7$ yr with their model. The crossing time of the H I cloud observed here is, several pc / several km s^{-1} $\sim 1 \times 10^6$ yr. The time scale of the cloud formation is then estimated to be an order of 10^6 yr. These facts suggest that there is a possibility of detecting

an H_2 cloud without CO just after the formation of the cloud. Therefore, the HLCG 92−35 is expected to be the youngest molecular cloud in the present observed region and to be at a stage just after moleuclar cloud formation. There is, however, still a possibility of sub-thermal excitation of CO. Since the H I cloud toward HLCG 92−35 has largest size in the present observed region, the length along the line of sight is expected to be large, ∼4 pc, which makes $n(H_2)$ of HLCG 92−35 smaller than those of MBM 54 and MBM 55 by a factor of a few. Further multi-line observeations are needed to know the exitation of CO in these clouds. In any case, evidence for H_2 cloud not traced by CO emission has been indicated by many authors; Reach et al. (1994) for high latitude cirrus, Meyerdierks & Heithausen (1996) for Polaris flare, Boulanger et al. (1998) for Chamaeleon dark cloud, and Onishi et al. (2001) for high galactic latitude clouds. Such a cloud is a nice target for studying molecular cloud formation because it is expected to be very young in terms of molecular cloud formation. In order to look deeper into the properties of such an object, multi-transition molecular line observations and especially [C I] observations with high spatial resolution of $\sim$ a few arcmin are definitely needed.

3.4.4 Morphology of the Cloud Complex and HI Shell

The present cloud complex including MBM 53, 54, 55, and HLCG 92−35 has an arc-like strucuture and is composed of more than a hundred of small molecular clouds. It includes clouds with different evolutionary stages in terms of moleuclar cloud formation as discussed in the previous sub-section. The same type of cloud complex was reported in Ursa Major cloud by de Vries et al. (1987). The CO clouds are distributed along an arc-like structure with many local peaks, although the spatial extent is smaller, $\sim 7°$, than that of the present complex. They claimed that there is a clear H I-H_2 transition region at $(l, b) \sim (141°, 39°)$ in the complex. These situations resemble the present ones. The difference is that they didn't found H_2 clouds without CO emission in their region. There is also a difference in the position where the transition takes place. In the present case, the transition region is located in a filamentary structure and the transition from H I to H_2 is perpendicular to the filament, whereas in the Ursa Major case, it is located at the edge of a filament and the transition occurs along the filament. The cause of the difference is hardly understood in the present situation of the small number of observation samples. The detailed investigation of surrounding environment may be helpful to understand it. We note here that the centroid velocity of the H I peak and the CO peak in the Ursa Major case is different (Pound & Goodmann 1997); there are

two velocity components in H I spectra toward the transition region. Because the velocity difference is not so large, the difference in velocity may be due to velocity gradient in the same cloud, however, there is a possibility that the two clouds are accidentally projected.

Pound & Goodman (1997) suggested that the Ursa Major cloud is a part of an expanding shell known as the North Celestial Pole loop, and that the cloud is located far-side of the shell from the kinematic analysys of the atomic and molecular gas. It is also suggested that the H I filament that includes the present molecular cloud complex is a part of an expanding H I filament (Gir et al. 1994), although the CO cloud seems to be located at the edge of the shell in the present case. Gir et al. (1994) derived an expanding velocity of $\sim$18 km s^{-1}, and suggested that the filament could have been formed by a few supernovae or another similarly large mechanical input of energy such as the stellar wind from an OB association of early O stars from the estimation of the kinetic energy. If this is true, the molecular cloud formation can be affected by such explosive events; triggering molecular cloud formation, or destroying existed molecular clouds. As mentioned in the previous section, HLCG 92$-$35 is associated with the western half of the H I cloud and the peak of the H I cloud is the west of one. Furthermore, there is a sharp western edge of the ^{12}CO distribution, although the diffuse cloud is extended toward the opposite direction. These observational facts imply that HLCG 92$-$35 seems to be preferentially formed at the western edge of the H I cloud. This might be because the old explosive events triggered the molecular cloud formation in the H I filament.

It is to be noted that the expanding velocity of $\sim$18 km s^{-1} by Gir et al. (1994) seems to be too fast compared with the radius of $\sim$23 pc because the age of the shell is then estimated to be $\sim 10^6$ yr or less. In this case, the early type B stars should remain inside the shell, although we found no OB stars or no X-ray radiation in the shell. However, our observation supports their idea that the shell could have been formed by some explosive events from the western direction. If this idea is correct, the expanding velocity should be much smaller in order to explain the environment around the shell. Actually, the present CO observation shows no expanding motions, and therefore, the expanding velocity should be less than or roughly equal to the total velocity dispersion of the present clouds, $\sim$ several km s^{-1}.

3.5 Conclusions

We have made a large-scale survey of high galactic latitude molecular clouds in the $J = 1$–0 lines of ^{12}CO, ^{13}CO, and C^{18}O toward an H I filament which contains MBM 53, 54, and 55 complex with NANTEN telescope. This survey spatially resolved the distribution of molecular gas toward the entire MBM clouds for the first time, and furthermore, we newly found a relatively massive cloud of interesting nature, whose evolutionary status is very young in terms of molecular cloud formation. The main results of the present study are summarized as follows:

1. The ^{12}CO observation covered the entire H I filament with a grid spacing of 4'. The filament is found to consist of many small-sized molecular clouds and there identified 108 ^{12}CO clouds in the observed region. The total mass is estimated to be $\sim$1200 $M_{\odot}$ if we assume the normal conversion factor from CO intensity as 1.0×10^{20} cm^{-2}/(K km s^{-1}).

2. We performed the ^{13}CO observation toward the region of high ^{12}CO intensities in order to measure the optical depth of molecular gas. We identified 70 ^{13}CO clouds and derived the physical properties of column densities and masses under the assumption of LTE. The tables of the physical properties of the ^{13}CO clouds are presented.

3. The mass spectra of ^{12}CO and ^{13}CO clouds are calculated to be $dN/dM \sim M^{-1.73\pm0.08}$ and $dN/dM \sim M^{-1.65\pm0.12}$, respectively. These spectrum indices are similar to that which has been derived in other regions.

4. The virial mass to LTE mass ratio is found to be $\gg 1$ for all the clouds, and therefore, the clouds are not gravitationally bounded if we consider the mass traced only by ^{13}CO. This implies that the star formation will not occur in the present ^{13}CO clouds in the near future.

5. The C^{18}O observation was carried out toward high-intensity region in the ^{13}CO map. There is no C^{18}O detection with a rms noise temperature of as low as $\sim$0.07 K. This also indicates that there is no cloud dense enough to form stars in the near future of $\sim 10^6$ yr.

6. Comparison between the distributions of molecular gas and T Tauri stars suggests that there are at least two weak-line T Tauri stars around MBM 55. This indicates that there might be star formation $\sim 10^7$ yr ago although the

activity was considered to be quite low compared with the mass of the current molecular gas.

7. We newly found a relatively massive cloud between MBM 53 and 54 around $(l, b) \sim (92°, -35°)$ of $\sim$330 $M_\odot$. HLCG 92−35 occupies a galactic western half of a circular-shaped H I gas, and the H I to CO mass ratio is estimated to be the largest in the observed region. The far-infrared excess over H I emission, which is a good indicator of the existence of molecular hydrogen, toward HLCG 92−35 is the largest in the observed region. Together with low CO optical depth, the ratio of the luminosity of the infrared excess to CO mass is calculated to be significantly larger than those of the other clouds by a factor of $\sim$5. These facts indicate that HLCG 92−35 is a CO-forming molecular cloud, which is younger than the MBM clouds in terms of molecular cloud formation.

8. The observational facts imply that HLCG 92−35 seems to be preferentially formed at the western edge of the H I cloud. This might be because the old explosive events triggered the molecular cloud formation in the H I filament.

References

Bhatt, H. C. 2000, A&A, 362, 715

Crawford, D. F., Jauncey, D. L., & Murdoch, H. S. 1970, ApJ, 162, 405

de Vries, H. W., Heithausen, A., & Thaddeus, P. 1987 ApJ, 319, 723

Dickman, R. L. 1978, ApJS, 37, 407

Gir, B. Y., Blitz, L., & Magnani, L. 1994, ApJ, 434, 162

Hartmann, D., & Burton, W. B. 1997, Atlas of Galactic Neutral Hydrogen. Cambridge Univ. Press, Cambridge

Hearty, T., Magnani, L., & Caillault, J. P. 1999, A&A, 341, 163

Heithausen, A., & Thaddeus, P. 1990, ApJ, 353, L49

Kawamura, A., Onishi, T., Mizuno, A., Ogawa, H., & Fukui, Y. 1998, ApJS, 117, 387

Kawamura, A., Onishi, T., Mizuno, A., Ogawa, H., & Fukui, Y. 1999, PASJ, 51, 851

Kramer, C., Stutzki, J., Rohrig, R., & Corneliussen, U. 1998, A&A, 329, 249

Kun, M. 1992, A&AS, 92, 875

Kutner, M. L., & Ulich, B. L. 1981, ApJ, 250, 341

Lee, H.H., Herbst, E., Pineau des. Forêts, G., Roueff, E., & Le Bourlot, J. 1996, A&A, 311, 690

Li, J. Z., Hu, J. Y., & Chen, W. P. 2000, A&A, 356, 157

Magnani, L., Blitz, L., & Mundy, L. 1985, ApJ, 295, 402 (MBM)

Magnani, L., Hartmann, D., & Speck, B. G. 1996, ApJS, 106, 447

Martin, E. L., & Kun, M. 1996, A&AS, 116, 467

Myers, P. C., Fuller, G. A., Mathieu, R. D., Beichman, C. A., Benson, P. J., Schild, R. E., & Emerson, J, P. 1987, ApJ, 319, 340

Pound, M. W., Bania, T. M., & Wilson, R. W. 1990, ApJ, 351, 165

Pound, M. W., & Goodman, A. A. 1997, ApJ, 482, 334

Reach, W. T., Koo, B. C., & Heiles, C. 1994, ApJ, 429, 672

Reach, W. T., Pound, M. W., Wilner, D. J., & Lee, Y. 1995, ApJ, 441, 244

Reach, W. T., Wall, W. F., & Odegard, N. 1998, ApJ, 507, 507

Sakamoto, S. 2002, ApJ, 565, 1050

Schlegel, D. J., Finkbeiner, D. P., & Davis, M. 1998, ApJ, 500, 525

Tachihara, K., Mizuno, A., & Fukui, Y. 2000, ApJ, 528, 817

Welty, D. E., Hobbs, L. M., Blitz, L., & Penprase, B. E. 1989, ApJ, 346, 232

Wouterloot, J. G. A., Heithausen, A., Schreiber, W., & Winnewisser, G. 2000, A&AS, 144, 123

Yamaguchi, N., Mizuno, N., Moriguchi, Y., Yonekura, Y., Mizuno, A., & Fukui, Y. 1999, PASJ, 51, 765

Yonekura, Y., Dobashi, K., Mizuno, A., Ogawa, H., & Fukui, Y., 1997, ApJS, 110, 21

Zimmermann, T., & Ungerechts, H. 1990, A&A, 238, 337

Table 3–1. Physical Properties of ^{12}CO Clouds

No. (1)	l (2)	b (3)	T_R^* (4)	ΔV (5)	V_{LSR} (6)	R (7)	$N(H_2)$ (8)	M_{CO} (9)
1	92.00	−29.13	2.1	2.2	−8.4	0.17	4.0	0.6
2	91.69	−29.46	2.6	4.4	−10.0	0.33	4.8	2.1
3	92.00	−30.53	2.7	6.1	−9.7	0.20	5.0	1.0
4	91.76	−30.27	1.1	6.1	−9.7	0.67	15.2	15.7
5	92.31	−30.40	1.6	2.8	−10.0	0.14	5.0	0.5
6	92.38	−30.73	2.8	3.3	−9.2	0.17	5.1	0.9
7	91.54	−30.80	2.9	4.3	−6.2	0.14	3.1	0.4
8	91.30	−30.67	3.4	2.0	−6.0	0.21	5.0	1.3
9	92.85	−30.67	3.6	3.3	−10.9	0.31	8.2	2.4
10	92.69	−31.00	3.4	1.9	−7.6	0.20	4.0	0.7
11	91.69	−30.94	2.3	4.7	−5.5	0.37	4.7	2.9
12	94.65	−31.33	0.8	3.1	−5.0	0.30	5.6	2.1
13	94.97	−31.53	3.5	2.0	−5.7	0.22	4.5	0.9
14	95.29	−31.73	3.2	3.5	−7.5	0.14	5.0	0.7
15	95.24	−32.40	2.8	3.1	−8.1	0.31	4.8	2.0
16	93.48	−31.13	2.9	6.4	−10.7	0.14	5.7	0.5
17	93.79	−31.20	5.4	6.1	−5.2	0.17	2.8	0.5
18	94.27	−31.80	2.4	1.5	−3.5	0.17	2.8	0.5
19	93.81	−32.33	2.0	3.1	−2.2	0.36	5.7	3.4
20	93.83	−33.14	2.8	2.7	−2.3	1.21	9.5	42.5
21	92.62	−31.40	2.7	2.4	−5.3	0.20	4.9	0.9
22	92.39	−31.93	2.6	2.4	−2.4	0.14	5.0	0.5
23	93.02	−32.20	4.6	2.2	−10.8	0.42	5.4	2.8
24	93.02	−32.40	5.1	2.2	−10.8	0.70	10.8	13.1
25	94.16	−33.53	3.5	1.9	−2.2	0.37	5.0	2.3
26	94.08	−33.73	2.4	2.2	−2.1	0.17	3.5	0.6
27	94.64	−33.67	2.2	3.7	−8.3	0.14	3.7	0.4
28	94.65	−33.93	2.4	5.6	−6.0	0.14	4.9	0.1
29	94.41	−34.06	2.3	2.3	−8.3	0.14	3.8	0.5
30	95.05	−33.73	2.8	5.3	−6.8	0.38	6.4	3.4
31	94.58	−34.27	3.1	7.8	−8.7	0.20	5.1	1.1
32	94.90	−34.20	2.6	3.8	−4.2	0.30	3.1	1.5
33	94.75	−34.53	2.7	2.6	−3.1	0.26	3.8	1.3
34	94.92	−34.73	3.1	1.4	−3.1	0.20	2.4	0.6
35	96.03	−34.20	3.0	2.4	−7.9	0.20	4.9	0.8
36	96.36	−34.27	2.9	6.5	−8.2	0.20	3.9	0.7
37	96.35	−34.07	2.3	4.0	−7.5	0.17	3.1	0.5
38	96.58	−34.00	2.1	4.8	−8.1	0.22	2.5	0.7
39	95.59	−35.20	2.3	3.1	−3.1	0.24	5.6	1.3
40	95.60	−35.40	2.5	2.5	−3.8	0.17	4.0	0.6
41	95.12	−35.73	2.7	3.6	−3.4	0.39	5.2	3.5
42	94.95	−35.67	3.0	1.6	−3.1	0.14	4.1	0.4

Table 3–1. (Continued)

No. (1)	l (2)	b (3)	T_R^* (4)	ΔV (5)	V_{LSR} (6)	R (7)	$N(H_2)$ (8)	M_{CO} (9)
43	95.30	−36.07	2.0	4.7	−3.1	0.22	5.8	1.3
44	94.33	−36.60	3.6	4.9	−5.3	0.84	10.9	21.5
45	93.49	−36.40	2.1	1.9	−6.5	0.14	2.8	0.3
46	93.24	−36.40	1.7	3.5	−8.0	0.17	2.7	0.4
47	93.40	−36.70	2.7	5.3	−5.9	0.22	5.3	1.1
48	93.32	−36.27	3.2	4.1	−7.0	0.26	6.6	1.8
49	93.15	−35.87	2.6	2.1	−9.8	0.14	3.6	0.4
50	92.74	−36.13	3.3	4.3	−4.2	0.36	6.2	3.2
51	92.41	−36.20	4.7	5.8	−6.5	0.26	9.0	2.5
52	92.25	−36.00	—	2.2	−7.5	0.20	3.1	0.8
53	92.49	−36.00	2.2	2.1	−7.6	0.14	3.2	0.4
54	92.50	−36.80	1.6	4.3	−3.4	0.17	5.7	0.8
55	96.48	−37.93	1.8	6.6	−5.4	0.17	5.7	0.6
56	96.14	−37.87	2.4	3.6	−3.6	0.28	4.8	1.7
57	95.71	−37.80	2.7	1.7	−3.9	0.14	2.2	0.3
58	96.21	−37.73	2.4	1.6	−5.6	0.14	2.0	0.3
59	96.20	−37.47	1.9	2.4	−5.7	0.14	2.4	0.3
60	95.85	−37.20	1.8	6.5	−6.8	0.17	2.4	0.4
61	95.53	−37.53	1.9	3.6	−6.0	0.20	4.8	1.1
62	94.67	−36.87	2.9	2.0	−3.6	0.24	4.1	1.2
63	91.66	−37.40	2.0	1.7	−3.2	0.17	3.8	0.6
64	91.50	−37.40	2.1	1.3	−3.3	0.14	2.7	0.3
65	91.41	−37.73	2.0	4.4	−3.0	0.14	2.9	0.3
66	93.18	−37.47	2.0	4.4	−3.0	2.22	25.4	212.3
67	92.25	−38.27	7.6	2.3	−4.9	0.17	4.0	0.6
68	93.11	−38.47	2.4	6.2	−5.5	0.24	5.7	1.4
69	92.17	−38.67	2.7	1.1	−9.8	0.17	7.1	0.9
70	92.60	−39.07	3.7	2.4	−2.0	0.31	4.4	1.8
71	92.95	−39.40	2.8	2.3	−2.3	0.17	2.4	0.4
72	92.60	−39.40	1.7	1.0	−1.5	0.14	2.0	0.3
73	92.52	−39.53	2.0	2.1	−1.7	0.20	4.5	0.9
74	90.61	−39.80	3.4	3.6	−1.7	0.24	4.7	1.4
75	90.01	−39.67	2.6	3.2	−1.1	0.56	8.9	7.4
76	89.97	−40.80	5.5	4.4	−4.2	0.14	3.2	0.4
77	86.19	−41.80	2.0	2.2	−5.4	0.14	3.2	0.4
78	85.84	−41.67	2.6	3.9	−7.1	0.17	2.6	0.4
79	84.85	−41.80	2.0	2.3	−6.9	0.26	5.4	1.7
80	84.45	−42.13	3.0	0.7	−5.9	0.17	3.8	0.7
81	85.65	−42.67	3.4	1.5	−6.4	0.14	3.7	0.4
82	84.82	−42.80	2.6	1.4	−6.5	0.24	2.9	0.9

Table 3–1. (Continued)

No.	l	b	T_R^*	ΔV	V_{LSR}	R	$N(H_2)$	M_{CO}
(1)	(2)	(3)	(4)	(5)	(6)	(7)	(8)	(9)
83	83.98	−43.00	2.2	3.5	−6.4	0.17	4.8	0.6
84	83.94	−41.87	3.6	1.8	−2.8	0.41	5.1	3.6
85	87.80	−40.40	4.3	1.6	−8.3	0.14	3.4	0.4
86	87.67	−41.00	2.4	1.9	−6.0	0.24	3.7	1.3
87	96.12	−29.07	2.7	1.9	−6.0	0.26	10.7	3.7
88	95.99	−25.60	4.7	2.2	−15.8	0.30	5.9	2.3
89	96.22	−29.60	3.2	3.0	−5.2	0.17	4.4	0.6
90	89.33	−31.87	2.4	1.6	−1.7	0.14	4.3	0.5
91	89.92	−33.40	2.3	1.9	−1.7	0.14	4.2	0.5
92	90.09	−33.27	2.2	1.7	−2.2	0.17	4.6	0.6
93	88.94	−36.27	3.0	2.4	−11.7	0.22	4.8	1.0
94	91.41	−37.73	2.8	2.4	−11.7	0.14	2.9	0.3
95	91.32	−38.20	2.0	5.9	−3.1	1.36	20.8	73.4
96	90.26	−39.93	5.9	4.2	−2.6	0.24	4.8	1.3
97	89.64	−40.27	2.6	3.1	−9.5	0.94	10.9	29.7
98	88.98	−41.33	3.4	5.5	−6.1	2.41	25.0	256.2
99	——	——	7.6	5.5	−6.1	0.20	4.7	0.9
100	94.35	−34.80	1.6	4.3	−7.1	0.34	7.3	3.2
101	92.25	−35.73	4.4	4.3	−7.1	0.60	8.4	12.4
102	92.32	−34.40	8.3	4.3	−7.1	2.57	28.9	326.9
103	93.94	−34.27	3.7	6.7	−4.9	0.57	8.6	9.3
104	93.21	−34.07	2.4	3.7	−5.4	0.17	4.6	0.6
105	93.28	−33.80	3.2	7.0	−6.4	0.17	4.3	0.7
106	93.20	−33.47	2.5	5.5	−5.4	0.28	4.2	1.6
107	92.72	−33.73	3.1	4.3	−7.6	0.20	5.1	1.0
108	92.56	−33.53	2.0	3.5	−7.3	0.20	3.9	0.7

Note—Col. (1) : Cloud number, Col. (2)–(3) : Cloud peak (l, b) position in degree, Col. (4) : Peak temperature in K, Col. (5) : Line width of the composite spectrum in km s^{-1}, Col. (6) : Peak velocity of the composite spectrum in km s^{-1}, Col. (7) : Radius of the molecular cloud in pc, Col. (8) : Column density of peak position in 10^{20} cm^{-2}, Col. (9) : Mass of the molecular cloud in $M_\odot$. Col. (4) to (6) are derived by using a single Gaussiun fitting. The peak temperature of cloud No.31 could not be derived by using a single Gaussiun fitting. The peak position of cloud No.101 is the same as that of cloud No.100.

Table 3–2. Observed Properties of ^{13}CO Clouds

	Position		Observed Properties of 13CO clouds			
No.	l	b	T_R^*	ΔV	V_{LSR}	$\int T_R^* dv$
(1)	(2)	(3)	(4)	(5)	(6)	(7)
1	91.73	−30.33	1.1	1.2	−9.6	1.35
2	93.79	−31.23	1.5	1.3	−5.5	1.72
3	92.94	−32.07	0.6	2.6	−10.5	1.41
4	93.02	−32.13	0.5	0.7	−10.7	0.41
5	92.95	−32.40	0.4	4.4	−10.1	1.21
6	91.72	−34.33	0.9	2.4	−7.7	1.69
7	92.69	−34.40	0.7	2.4	−5.7	1.18
8	92.08	−34.67	1.2	1.8	−7.2	1.77
9	91.88	−34.40	0.4	2.6	−5.6	0.75
10	92.00	−34.50	0.9	1.0	−6.2	0.92
11	92.57	−34.53	0.9	1.5	−6.4	1.08
12	91.51	−34.83	0.8	0.9	−8.3	0.95
13	91.72	−34.83	0.6	2.6	−7.4	1.18
14	91.63	−34.90	0.6	1.5	−8.5	0.68
15	91.88	−34.93	0.6	1.7	−7.0	0.86
16	91.96	−34.93	0.5	1.6	−6.8	0.47
17	91.63	−35.00	1.3	1.4	−8.4	1.59
18	91.84	−35.07	0.5	1.7	−7.8	0.68
19	92.12	−35.13	0.6	0.9	−7.1	0.43
20	91.76	−35.17	0.5	3.1	−8.8	1.31
21	92.53	−35.23	0.7	1.1	−7.4	0.59
22	96.37	−35.23	0.7	1.1	−7.4	1.63
23	91.84	−35.37	0.6	1.9	−7.7	0.84
24	92.00	−35.37	1.6	0.8	−5.6	1.20
25	92.12	−35.40	0.5	2.4	−5.6	0.71
26	92.33	−35.53	0.5	2.2	−5.5	0.79
27	92.82	−35.50	1.4	0.4	−5.1	0.56
28	92.62	−35.60	1.1	1.7	−4.8	1.50
29	92.00	−35.57	1.0	0.7	−6.4	0.51
30	92.29	−35.67	0.9	0.9	−8.9	1.39
31	92.08	−33.23	0.3	2.3	−7.5	0.76
32	92.00	−33.23	0.5	2.5	−7.5	1.33
33	92.36	−33.37	0.4	2.5	−7.3	0.97
34	91.96	−33.43	0.6	2.4	−7.0	1.43
35	92.00	−33.83	1.3	1.1	−10.0	1.55
36	92.28	−33.97	0.6	0.8	−8.1	0.47
37	94.18	−37.43	1.9	1.7	−4.6	2.85
38	93.14	−37.63	1.2	4.7	−5.8	4.35
39	93.06	−37.90	0.9	2.2	−6.7	1.53
40	92.75	−37.17	0.8	1.6	−3.3	1.27

Table 3–2. (Continued)

	Position		Observed Properties of 13CO clouds			
No.	l	b	$T_{\rm R}^{*}$	ΔV	$V_{\rm LSR}$	$\int T_{\rm R}^{*} dv$
(1)	(2)	(3)	(4)	(5)	(6)	(7)
41	92.67	−37.50	0.4	2.2	−4.8	0.90
42	92.54	−37.27	0.5	2.0	−4.6	0.90
43	92.34	−37.43	0.6	2.3	−4.5	1.36
44	92.00	−37.40	0.6	1.8	−5.0	1.15
45	91.28	−38.13	1.6	1.8	−3.3	2.38
46	91.28	−38.37	0.9	0.4	−4.3	0.47
47	91.14	−38.87	0.9	2.2	−1.9	1.47
48	90.93	−39.13	0.8	2.3	−1.2	1.22
49	91.09	−39.47	0.7	1.8	−4.8	1.67
50	91.19	−39.03	0.5	2.0	−0.9	1.00
51	91.31	−39.03	0.5	2.2	−1.8	0.96
52	89.18	−40.93	2.1	1.8	−7.7	3.43
53	89.66	−41.07	1.7	1.4	−4.8	2.41
54	88.45	−41.27	1.4	4.0	−5.9	4.78
55	88.71	−41.43	0.8	4.7	−5.5	3.08
56	88.22	−41.40	0.6	1.7	−6.0	0.98
57	88.21	−41.67	0.4	2.0	−8.0	0.67
58	87.81	−41.67	0.7	2.7	−7.5	1.92
59	87.54	−41.63	0.8	1.8	−6.2	1.48
60	87.40	−41.73	0.5	3.2	−6.7	1.72
61	87.30	−41.83	0.8	0.9	−6.5	0.68
62	87.17	−41.87	0.6	1.0	−6.9	0.73
63	86.78	−42.23	0.4	2.5	−7.2	1.00
64	86.65	−42.20	0.5	1.2	−5.6	0.63
65	86.43	−42.10	0.5	4.6	−6.5	2.13
66	86.08	−42.03	0.8	1.3	−6.4	1.16
67	86.06	−42.17	0.4	3.5	−5.5	1.55
68	85.89	−42.13	0.4	1.0	−9.1	0.46
69	85.72	−42.03	0.4	0.9	−6.3	0.47
70	85.67	−42.10	0.4	0.9	−7.0	0.45

Note—Col. (1) : Cloud number, Col. (2)–(3) : Cloud peak (l, b) position in degree, Col. (4) : Peak temperature in K, Col. (5) : Line width of the composite spectrum in km s^{-1}, Col. (6) : Peak velocity of the composite spectrum in km s^{-1}, Col. (7) : Integrated intensity of peak position in K km s^{-1}, Col. (4) to (6) are derived by using a single Gaussiun fitting.

Table 3–3. Physical Properties of ^{13}CO Clouds

No. (1)	$N(H_2)$ (2)	V_{comp} (3)	R (4)	M_{LTE} (5)	M_{vir} (6)	$\tau(^{13}CO)$ (7)
1	1.24	−9.9	0.31	8.43	144.48	0.25
2	1.45	−5.6	0.21	4.42	96.92	0.32
3	1.20	−10.7	0.18	2.65	19.77	0.20
4	0.69	−10.8	0.11	0.58	19.90	0.15
5	1.20	−10.7	0.28	6.50	119.03	0.21
6	1.65	−7.5	0.27	8.67	505.37	0.35
7	1.50	−5.3	0.20	4.08	350.95	0.26
8	1.51	−6.8	0.61	40.10	572.20	0.35
9	1.04	−6.7	0.09	0.53	32.97	0.12
10	1.04	−6.6	0.11	0.53	20.33	0.17
11	1.30	−6.4	0.11	1.11	58.90	0.20
12	1.16	−8.2	0.14	1.57	32.09	0.15
13	1.14	−7.8	0.11	0.97	153.16	0.17
14	1.02	−8.4	0.07	0.35	37.72	0.17
15	1.13	−7.1	0.12	1.10	44.59	0.18
16	0.76	−6.8	0.09	0.39	12.88	0.16
17	1.22	−8.2	0.20	4.45	148.36	0.35
18	1.09	−7.8	0.10	0.74	89.90	0.17
19	0.70	−7.2	0.07	0.24	17.61	0.14
20	1.22	−8.2	0.10	0.83	242.12	0.21
21	0.81	−7.4	0.16	1.51	59.47	0.16
22	1.33	−5.7	0.19	3.39	127.69	0.24
23	0.99	−7.9	0.12	1.17	125.34	0.17
24	1.42	−5.6	0.14	1.94	27.95	0.32
25	1.62	−6.0	0.09	0.82	3.30	0.18
26	1.03	−5.7	0.13	1.22	40.52	0.17
27	0.87	−5.0	0.07	0.30	13.98	0.26
28	1.40	−4.9	0.25	6.17	227.00	0.25
29	0.78	−6.1	0.07	0.26	6.15	0.15
30	0.97	−5.3	0.18	1.66	30.72	0.24
31	1.31	−7.2	0.10	0.89	38.63	0.21
32	2.09	−7.6	0.11	1.77	58.17	0.25
33	1.61	−7.6	0.11	1.37	85.71	0.23
34	1.97	−7.1	0.24	7.69	189.58	0.28
35	2.13	−9.8	0.40	23.54	142.37	0.59
36	1.07	−8.3	0.09	0.54	27.40	0.19
37	2.39	−4.3	0.33	18.26	251.82	0.42
38	2.67	−5.4	0.63	82.88	1426.28	0.32
39	1.68	−6.8	0.25	7.15	12.35	0.20
40	1.86	−3.8	0.16	3.47	154.84	0.31

Table 3–3. (Continued)

No. (1)	$N(H_2)$ (2)	V_{comp} (3)	R (4)	M_{LTE} (5)	M_{vir} (6)	$\tau(^{13}CO)$ (7)
41	1.74	−5.1	0.11	1.48	138.11	0.30
42	1.95	−4.3	0.11	1.65	90.21	0.24
43	1.16	−4.1	0.18	0.39	166.57	0.31
44	1.80	−4.5	0.33	13.44	206.65	0.30
45	1.75	−2.8	0.54	36.00	771.07	0.37
46	0.73	−2.1	0.10	0.50	20.99	0.17
47	1.38	−1.8	0.26	6.35	265.94	0.18
48	1.28	−1.6	0.21	3.92	243.15	0.15
49	1.35	−0.4	0.21	4.11	85.57	0.20
50	1.63	−1.1	0.09	0.83	61.66	0.20
51	1.60	−2.1	0.12	1.63	50.11	0.30
52	2.52	−7.4	0.33	19.71	213.73	0.51
53	1.62	−4.8	0.35	14.01	202.50	0.41
54	2.31	−5.6	0.77	95.82	631.44	0.38
55	2.66	−4.1	0.34	21.24	122.92	0.26
56	2.42	−6.1	0.07	0.82	43.05	0.28
57	1.44	−7.8	0.09	0.73	18.54	0.23
58	2.66	−6.7	0.19	6.79	479.87	0.31
59	1.61	−5.9	0.26	0.28	115.54	0.26
60	2.65	−6.2	0.11	2.25	72.09	0.26
61	1.84	−6.5	0.09	0.94	14.76	0.19
62	1.44	−6.9	0.14	1.96	111.81	0.22
63	1.35	−6.4	0.13	1.61	147.80	0.15
64	1.01	−6.1	0.07	0.34	28.93	0.14
65	1.69	−5.7	0.21	5.17	183.47	0.18
66	1.45	−6.2	0.10	0.98	36.40	0.20
67	1.46	−6.6	0.24	5.94	87.84	0.15
68	0.75	−6.0	0.09	0.38	11.12	0.08
69	0.79	−6.5	0.07	0.27	16.97	0.12
70	0.79	−6.8	0.07	0.27	33.62	0.14

Note—Col. (1) : Cloud number, Col. (2) : Column density of peak position in 10^{20} cm^{-2}, Col. (3) : Peak velocity of the composite spectrum in km s^{-1}, Col. (4) : Radius of the molecular cloud in pc, Col. (5) : Mass of the molecular cloud assuming the LTE in $M_{\odot}$, Col. (6) : Virial mass of the molecular cloud in $M_{\odot}$, Col. (7) : Optical depth of ^{13}CO. Col. (4) is derived by using a single Gaussiun fitting.

Table 3–4. Comparison among HLC 92-35, MBM 54, and MBM 55*

Cloud name	area (pc^2)	$M_{^{13}CO}$ ($M_\odot$)	$M_{HI}/M_{^{13}CO}$	$L_{I_{ex}}{}^{\ddagger}/M_{^{13}CO}$ (‡)	$L_{E(B-V)}{}^{\diamond}/M_{^{13}CO}$ ($^{\diamond}$)
HLCG92-35	8.38	82	0.82	0.81	0.034
MBM54	2.16	72	0.15	0.17	0.008
MBM55	5.70	164	0.20	0.14	0.009

*The regions only detected at more than 6.0 K km s^{-1} in ^{12}CO are picked out.

*$L_{I_{ex}} = \sum(F_{I_{ex}}\Omega)$. See section 4.3 for a full acount of $L_{I_{ex}}$.

†$L_{E(B-V)} = \sum(E(B-V)\Omega)$. See section 4.3 for a full acount of $L_{E(B-V)}$.

‡The unit is (MJy sr^{-1} pc^2 $M_\odot^{-1}$)

◇The unit is (mag pc^2 $M_\odot^{-1}$)

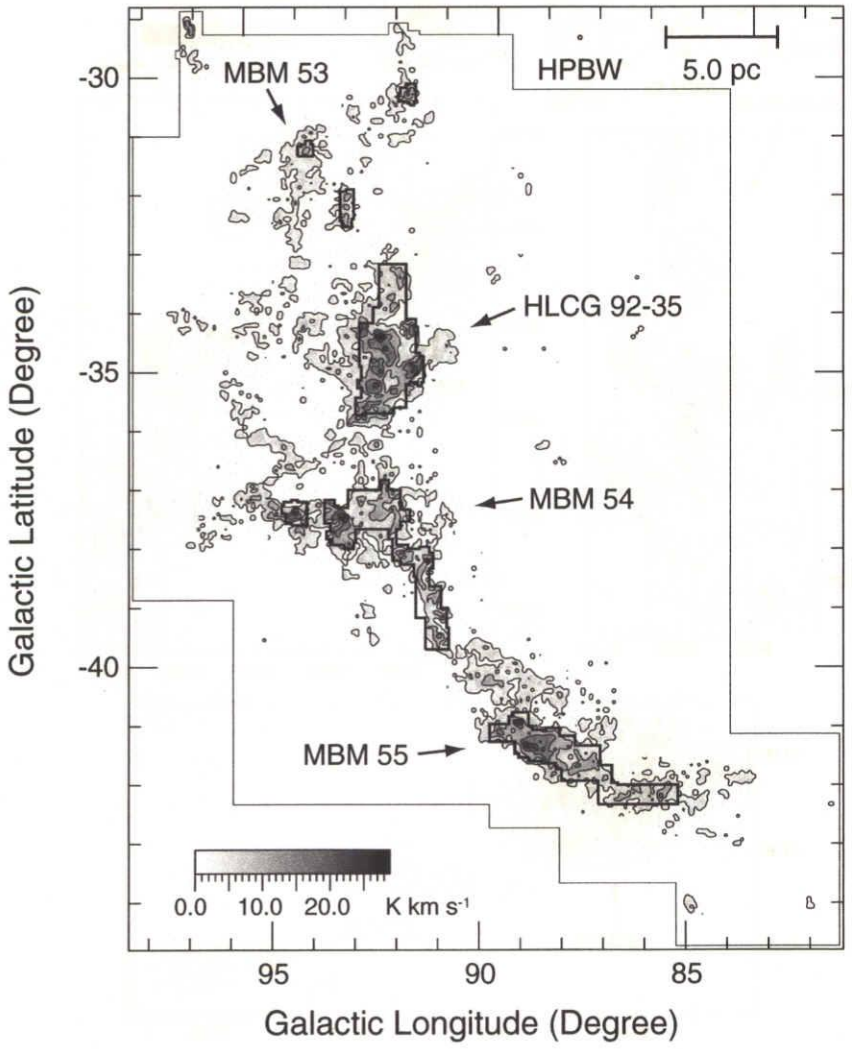

Figure 3–1. Total velocity integrated intensity map of ^{12}CO ($J = 1$–0) in galactic coordinates. The lowest contour is 1.50 K km s^{-1}, and separation between the contours is 6.0 K km s^{-1}. The observed area of ^{12}CO is denoted by a thin solid line and the one of ^{13}CO is denoted by thick solid lines.

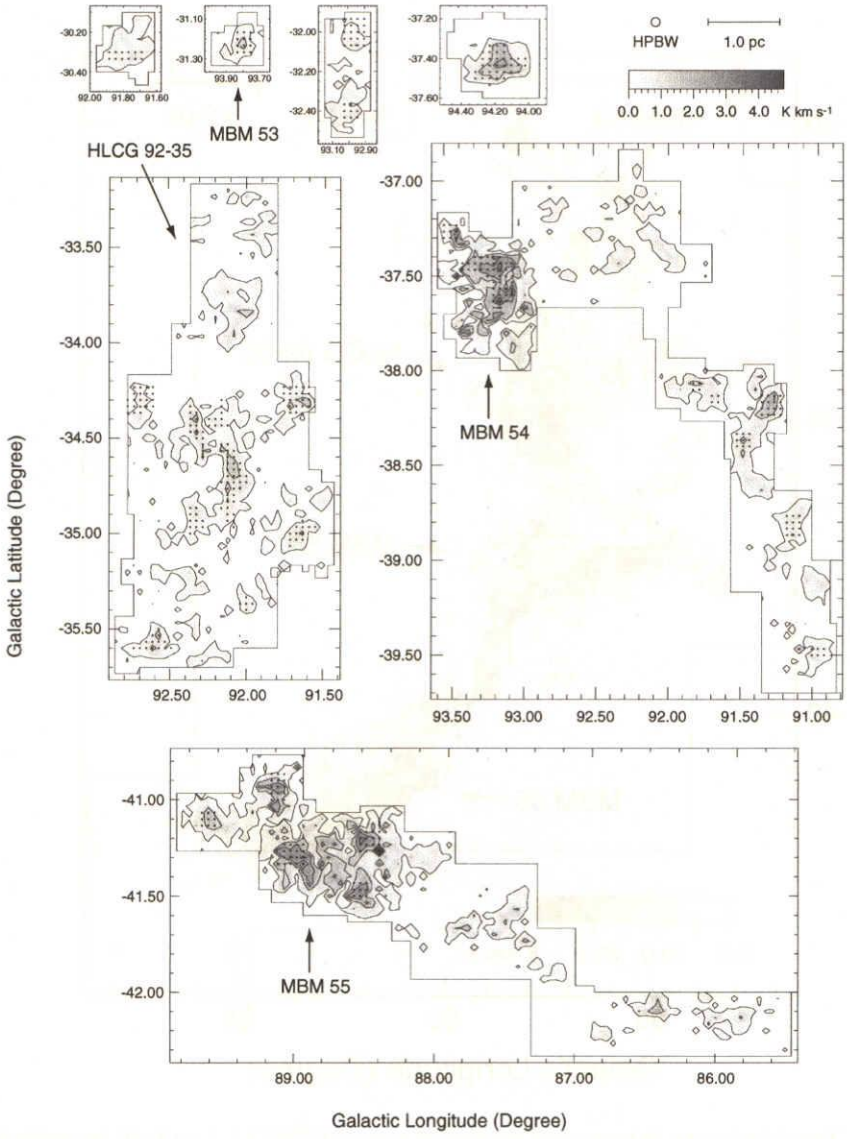

Figure 3–2. Total velocity integrated intensity map of ^{13}CO ($J = 1$–0) in galactic coordinates. The lowest contour is 0.33 K km s^{-1}, and separation between the contours is 0.99 K km s^{-1}. The filled circles are the positions observed in C^{18}O. The linear scale of all the figures are the same.

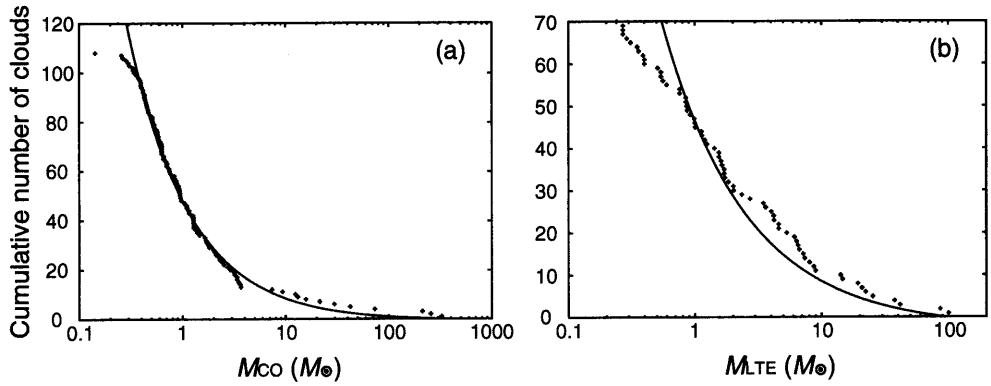

Figure 3–3. (a) The mass spectrum of ^{12}CO clouds. The number of clouds, $N(\leq M_{\rm CO})$ with mass grater than $M_{\rm CO}$, is plotted against $M_{\rm CO}$, along with the best-fitting power law for the mass range of 0.4 $M_{\odot}$, $N(\leq M_{\rm CO}) = 49 \times M_{\rm CO}^{-0.73} - 0.71$ (solid line) derived by using the maximum likelihood method (Crawford et al. 1970). (b) Same as (a), but for ^{13}CO clouds with $M_{\rm LTE}$. It is expressed as $N(\leq M_{\rm LTE}) = 49 \times M_{\rm LTE}^{-0.65} - 2.41$ (solid line) for the mass range of 0.7 $M_{\odot}$.

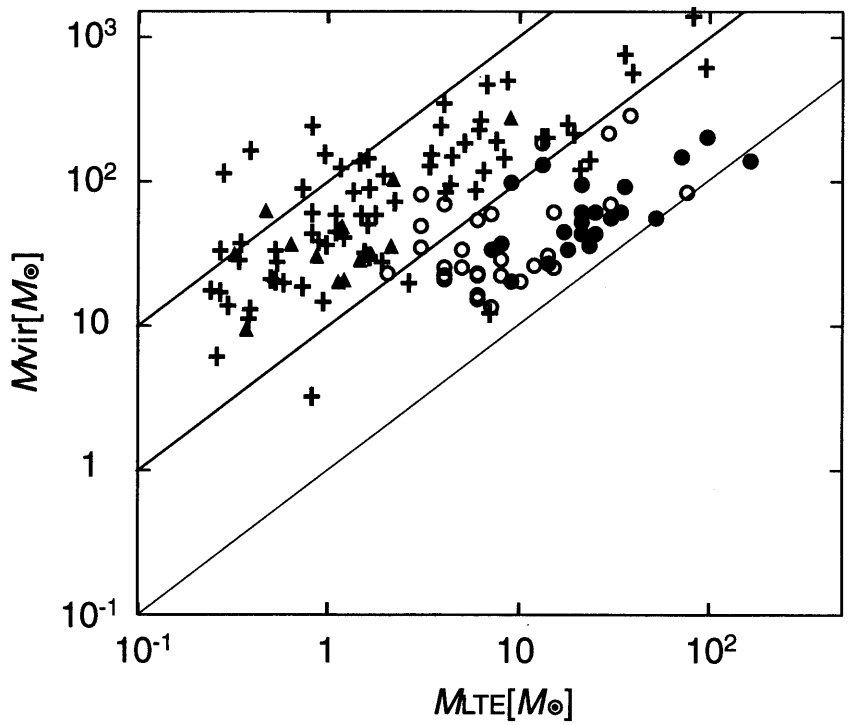

Figure 3–4. Virial mass, $M_{\rm vir}$, plotted against ^{13}CO LTE mass, $M_{\rm LTE}$. The crosses and closed triangles indicate ^{13}CO clouds in the present area and in MBM 12 (Pound et al. 1990), respectively. The filled circles and open circles are ^{13}CO clouds with and without C^{18}O cores in Ophiuchus north region (Tachihara et al. 2000), respectively. The three solid lines represent $M_{\rm vir}=10^2 \times M_{\rm LTE}$, $M_{\rm vir}=10 \times M_{\rm LTE}$ and $M_{\rm vir}=M_{\rm LTE}$ from the top.

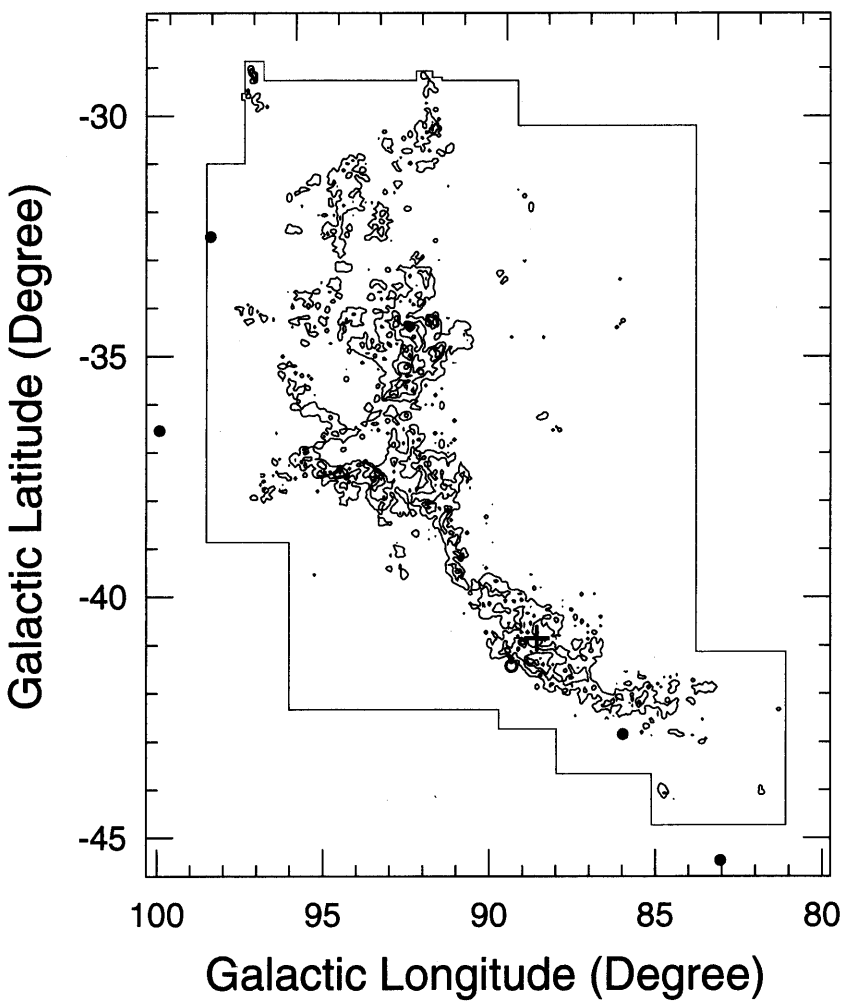

Figure 3–5. Positions of weak-line T Tauri stars detected by Li et al. (2000) (open circle). That confirmed by Martin & Kun (1996) (cross) and selected IRAS point sources (filled circles) are shown in galactic coordinates. The IRAS point sources are selected as candidates for protostars. The contour shows the velocity-integrated intensity of the ^{12}CO (J = 1–0). The lowest contours and intervals are the same as in Figure 3–1.

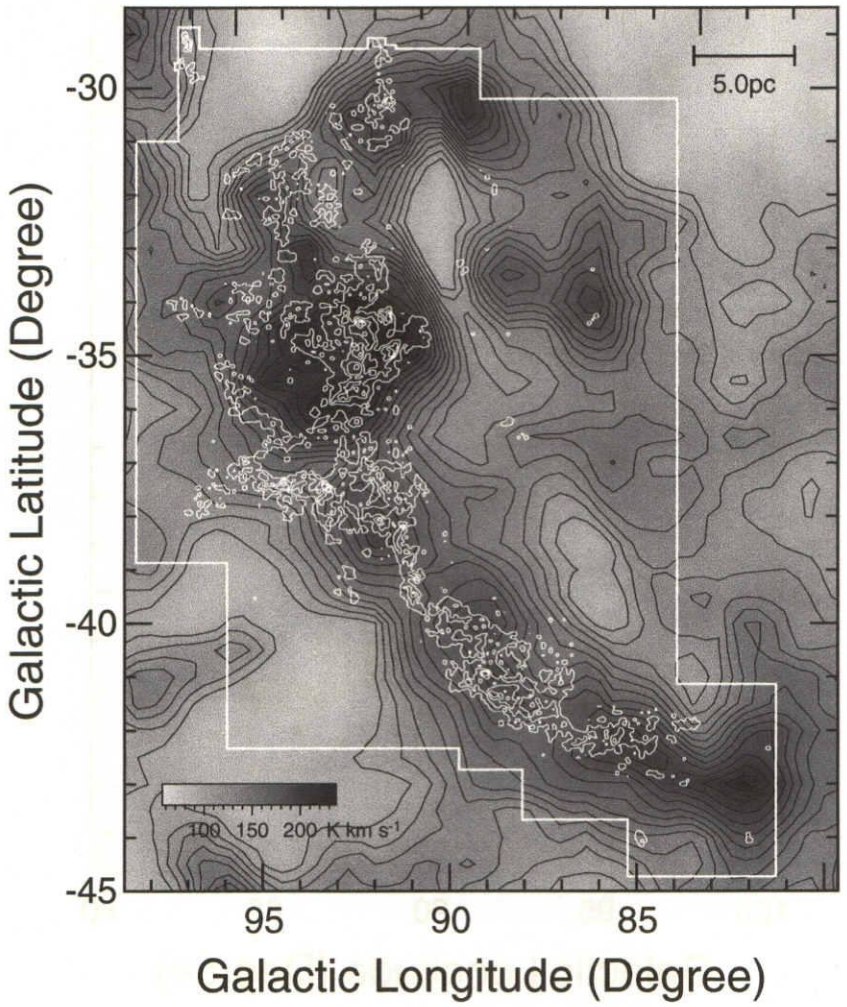

Figure 3–6. The velocity-integrated intensity map of ^{12}CO ($J = 1$–0) superposed on the velocity-integrated intensity map of H I with the velocity range -11 km s^{-1} $\leq$ $V_{\rm LSR} \leq 0$ km s^{-1} (Hartmann & Burton 1997). The lowest contours and separation between contours of ^{12}CO (white lines) are the same as Figure 3–1. The lowest contours of H I (black lines) are 100 K km s^{-1} and separation between contours is 10 K km s^{-1}.

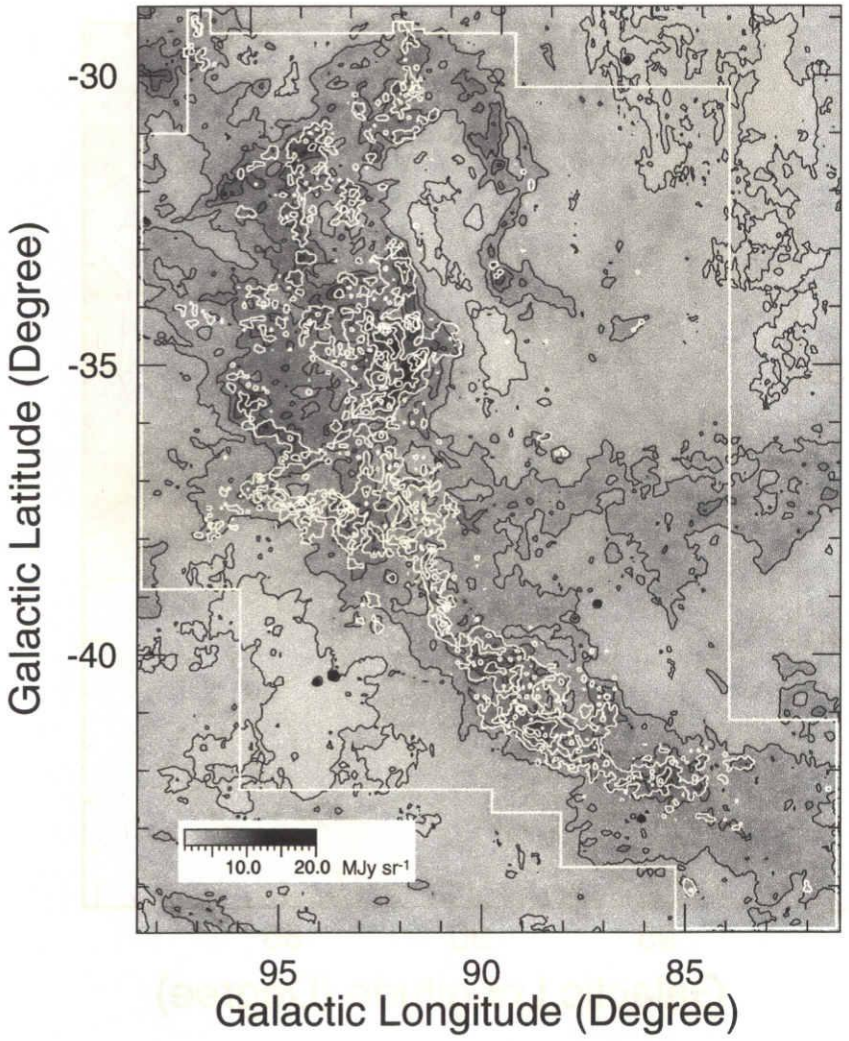

Figure 3–7. The velocity-integrated intensity map of ^{12}CO ($J = 1$–0) superposed on the IRAS 100 μm map by ISSA. The lowest contours and separation between contours of ^{12}CO (white lines) are the same as Figure 3–1. The contour levels of IRAS 100 μm (black lines) begin at and increase by steps of 2 MJy sr^{-1}.

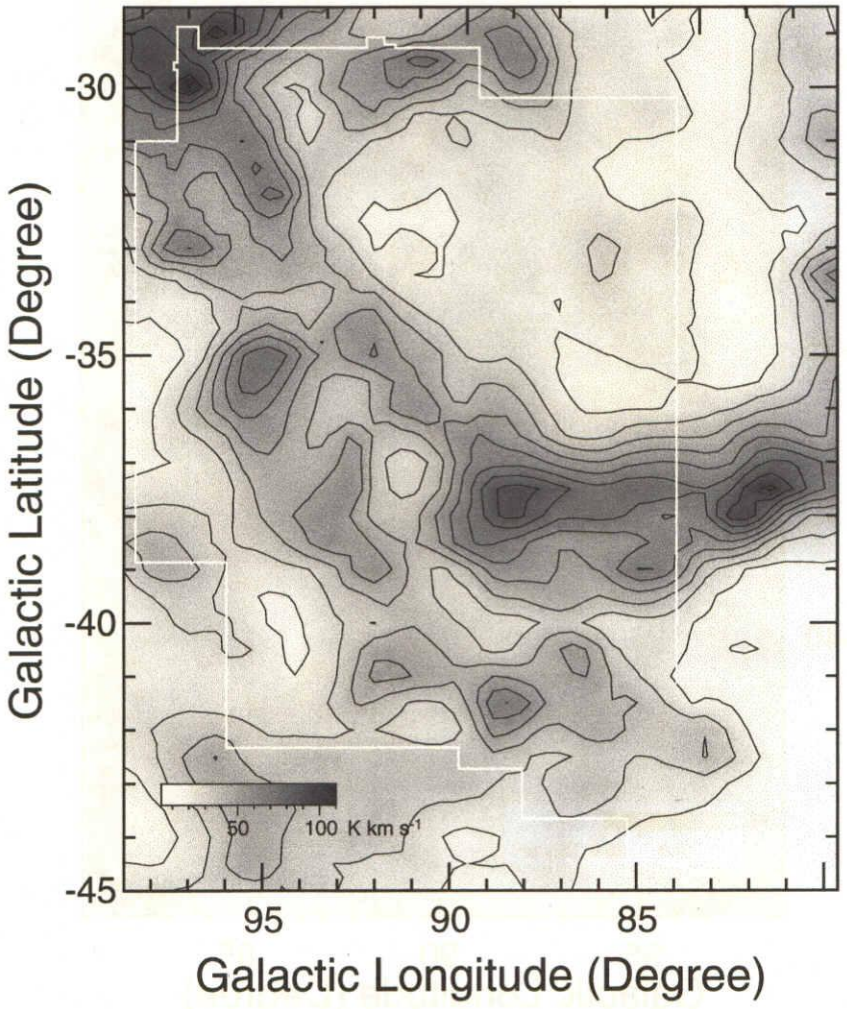

Figure 3–8. The velocity-integrated intensity map of H I for a velocity range -20 km s^{-1} $\leq V_{\rm LSR} \leq -12$ km s^{-1} (Hartmann & Burton 1997). The lowest contours of H I (black lines) are 0 K km s^{-1} and separation between contours is 10 K km s^{-1}. The observed area of ^{12}CO is denoted by the white solid lines.

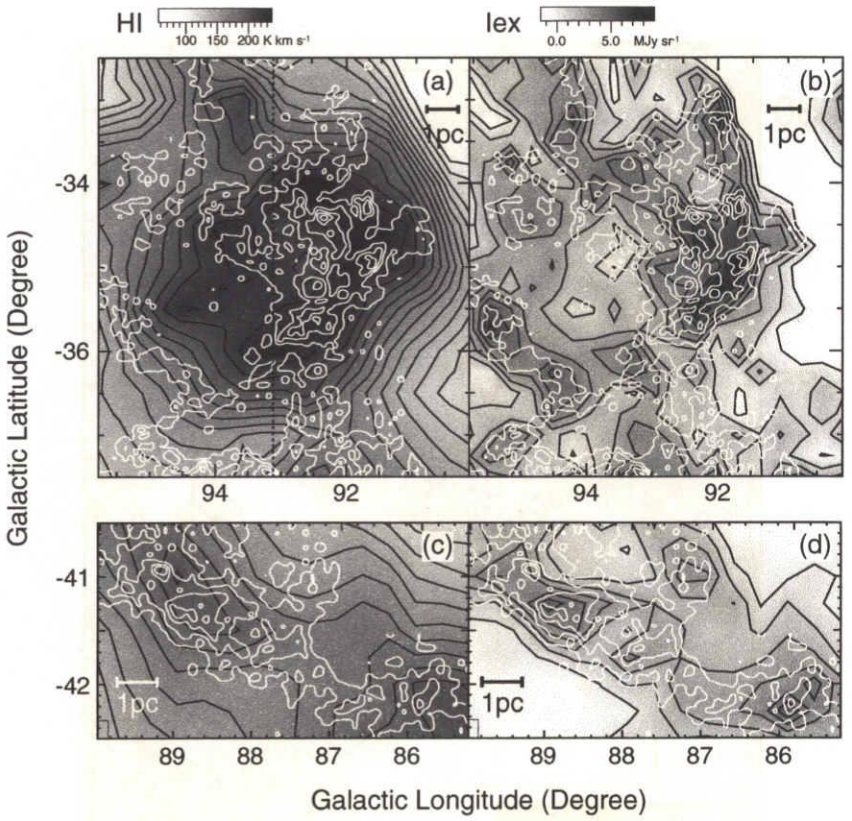

Figure 3–9. The map scaled up toward HLCG 92−35 and MBM55. The gray scales of H I integrated intensity of (a) and (c), and of infrared excess (b) and (d) are the same, respectively. (a): The map scaled up toward HLCG 92−35. The gray scale and black contours indicate the integrated intensity of H I with the velocity range $-11\ \mathrm{km\ s^{-1}} \leq V_{\mathrm{LSR}} \leq 0\ \mathrm{km\ s^{-1}}$ (Hartmann & Burton 1997). The lowest coutours and separation between contours are the same as Figure 3–6. White contours indicate the integrated intensity of ^{12}CO. The lowest coutours and separation between contours are the same as Figure 3–1. See seciton 3.4.2 for a full acount of the black dotted line in the upper-left panel. (b): Same as (a), but the gray scale and black contours indicate not H I but the infrared excess. The lowest coutours and separation between contours are 0 MJy sr^{-1} and 1 MJy sr^{-1}, respectively. (c): Same as (a), but for MBM55. (d): Same as (b), but for MBM55.

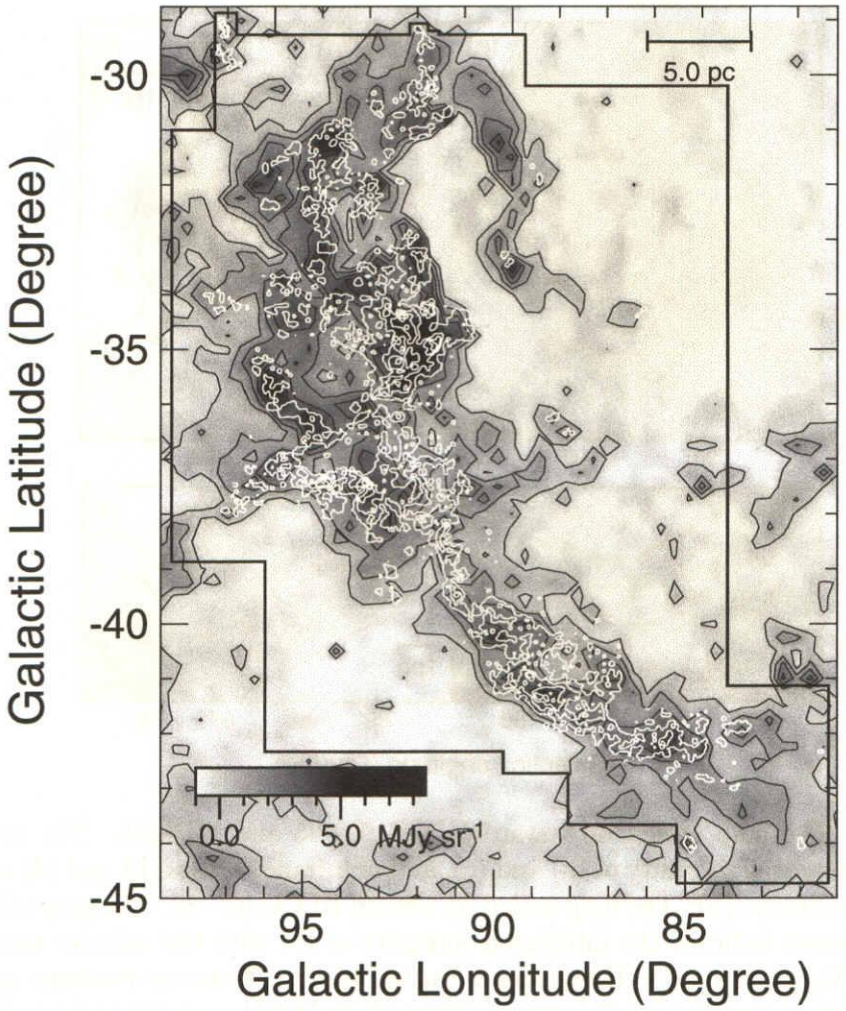

Figure 3–10. The velocity-integrated intensity map of ^{12}CO (J = 1–0) supuerposed on the infrared excess map. The lowest contours and separation between contours of the infrared excess (black lines) are 0 MJy sr^{-1} and 1 MJy sr^{-1}, . The lowest contours and separation between contours of ^{12}CO (white lines) are the same as Figure 3–1.

Chapter 4

Large Scale CO Observations of a Far-Infrared Loop in Pegasus

Abstract

We have carried out large scale CO observations with a mm/sub-mm telescope NANTEN toward a loop-like structure in far infrared whose angular extent is about 20×20 degrees around (l, b) $\sim$ (109°, −45°) in Pegasus. Its diameter corresponds to $\sim$ 26 pc at a distance of 100 pc, adapted from that of a star HD886 (B2IV) at the center of the loop. We covered the loop-like structure in the ^{12}CO (J = 1–0) emission at 4′–8′ grid spacing and in the ^{13}CO (J = 1–0) emission at 2′ grid spacing for the ^{12}CO emitting regions. The ^{12}CO distribution is found to consist of 78 small clumpy clouds whose masses range from 0.04 $M_{\odot}$ to 11 $M_{\odot}$, and about 83% of the ^{12}CO clouds have very small masses less than 1.0 $M_{\odot}$. ^{13}CO observations revealed that 19 of the 78 ^{12}CO clouds show significant ^{13}CO emission. ^{13}CO emission was detected in the region where the molecular column density of H_2 derived from ^{12}CO is greater than 5×10^{20} cm^{-2}, corresponding to Av of $\sim$ 1 mag, which takes into account that of H I. We find no indication of star formation in these clouds in IRAS Point Source Catalog and 2MASS Point Source Catalog. The very low mass clouds, $M \leq 1 M_{\odot}$, identified are unusual in the sense that they have very weak ^{12}CO peak temperature of 0.5 K–2.7 K and that they aggregate in a region of a few pc with no main massive clouds; contrarily to this, similar low mass clouds less than 1 $M_{\odot}$ in other regions previously observed including those at high Galactic latitude are all associated with more massive main clouds of $\sim$ 100 $M_{\odot}$. A comparison with a theoretical work on molecular cloud formation (Koyama & Inutsuka 2002) suggests

that the very low-mass clouds may have been formed in the shocked layer through the thermal instability. The star HD886 (B2IV) may be the source of the mechanical luminosity via stellar winds to create shocks, forming the loop-like structure where the very low-mass clouds are embedded.

Key Words : ISM: clouds — ISM: individual(High Latitude Clouds) — radio lines: ISM — stars: formation — stars: winds

4.1 Introduction

High Galactic latitude molecular clouds (hereafter HLCs) are typically located at $|b| \gtrsim 20°$–$30°$. Since the Gaussiun scale height of CO is estimated to be ~ 100 pc in the inner Galactic disk (e.g., Magnani et al. 2000), HLCs are likely located very close to the Sun, within a few hundred pc or less. Their proximity to the Sun and the low possibility of overlapping with other objects along the line of sight enable us to study them with a high spatial resolution and to compare CO data unambiguously with the data at other wavelengths. HLCs have lower molecular densities compared with dark clouds where the optical obscuration is significant. Therefore, HLCs are often called as translucent clouds (e.g., van Dishoeck & Black 1988) and most of the known HLCs are not the sites of active star formation, although a few of them are known to be associated with T Tauri stars (e.g., Magnani et al. 1995; Pound 1996; Hearty et al. 1999).

Given the very small distances of HLCs, it is a challenging task for observers to make a complete survey for HLCs over a significant portion of the whole sky. ^{12}CO ($J = 1$–0) emission has been used to search for HLCs because the line emission in the mm band is strongest among the thermally or sub-thermally excited spectral lines of interstellar molecular species. It is however difficult to cover an area as large as tens of square degrees subtended by some of the HLCs because of the general weakness of the ^{12}CO emission, typically $\sim$ a few K (e.g., Magnani et al. 1996), with existing mm-wave telescopes in a reasonable time scale. HLCs have been therefore searched for by employing various large-scale datasets at other wavelengths including the optical obscuration (Magnani et al. 1985; Keto & Myers 1986), the infrared radiation (Reach et al. 1994), and the far-infrared excess over H I (=FIR excess)(Blitz et al. 1990; Chaapter 2). On the other hand, unbiased surveys in CO at high Galactic latitudes have been performed at very coarse grid separations of 1° resulting in a small sampling factor of a few % (Hartmann et al. 1998; Magnani et al.

2000). Most recently, in Chapter 2 we discovered 32 HLCs or HLC complexes. This search was made based on the FIR excess, demonstrating the correlation between FIR excess clouds with CO clouds is a useful indicator of CO HLCs.

Previous CO observations of individual HLCs at higher angular resolutions show that HLCs exhibit often loop-like or shell-like distributions having filamentary features with widths of several arc min or less (Hartmann et al. 1998; Magnani et al. 2000; Bhatt 2000), and in addition that HLCs often compose a group, whose angular extent is $\sim$ 10 degrees or larger. In order to better understand the structure of HLCs and to pursue the evolution of HLC complexes, CO observations covering tens of square degrees at a high angular resolution are therefore crucial. The past observations of such complexes of HLCs are limited to a few regions including Polaris flare (Heithausen & Thaddeus 1990), Ursa Major (Pound & Goodman 1997) and the HLC complex toward MBM 53, 54, and 55 in Chapter 3. Pound & Goodman (1997) showed an arc-like structure of the molecular cloud system and suggest that the origin of such structures could be some explosive events. Most recently, in Chapter 3 we carried out extensive observations of the molecular cloud complex including MBM 53, 54, and 55 and suggest that the HLCs may be significantly affected by past explosive events based on the arc-like morphologies of molecular hydrogen (see also Gir et al. 1994).

The region of MBM 53, 54, and 55 is of particular interest among the three, because it is associated with a large H I cloud of $\sim$ 590 $M_{\odot}$ at a latitude of -35 degrees and because there is a newly discovered HLC of 330 $M_{\odot}$, HLCG92$-$35, which is significantly H I rich with a mass ratio $M(\mathrm{H_2})/M(\mathrm{H\,I})$ of $\sim$ 1, among the known HLCs (Chapter 3). This cloud was in fact missed in the previous surveys based on optical extinction (Magnani et al. 1985). Subsequent to these observations we became aware of that the region is also very rich in interstellar matter as shown by the 100μm dust features (Kiss et al. 2004). There is a loop-like structure shown in 100 μm around (l, b) $\sim$ (109°, -45°). Toward the center of the loop, an early type star HD886(B2IV) is located which may play a role in creating the loop. Its proper motion is large at a velocity of a few km s^{-1}, suggesting that the stellar winds of the star might have continued to interact with the surrounding neutral matter over a few tens of pc in $\sim$ a few Myr. Magnani et al. (1985) and we in Chapter 2 yet observed only a small part of this region. In order to reveal the large scale CO distribution of the region, we have carried out observations toward (l, b) $\sim$ (109°, -45°) by ^{12}CO (J = 1–0) and ^{13}CO (J = 1–0) by using NANTEN 4-meter millimeter/sub-mm telescope of Nagoya University at Las Campanas, Chile. We shall adopt the distance of 100 pc from the sun to the loop-like structure which is

equal to the distance of the B2 star in the center of the loop, and is also a typical value for the HLCs.

4.2 Observations

The observed region in ^{12}CO was $\sim$ 240 square degrees toward the whole area of the loop-like structure centered at around (l, b) $\sim$ (109°, -45°) shown in a 100 μm map by Schlegel et al. (1998). First, the ^{12}CO observations were made at a grid spacing of $8'\times\cos(b)$ and $8'$ in Galactic longitude and latitude, respectively. Then, the regions where the ^{12}CO emission is significantly detected were observed at a grid spacing of $4'\times\cos(b)$ and $4'$ in Galactic longitude and latitude, respectively. The ^{13}CO observations were made in and around the whole area where the peak temperature of ^{12}CO emission is higher than 2.0 K at a grid spacing of $2'\times\cos(b)$ and $2'$ in Galactic longitude and latitude, respectively. The periods of ^{12}CO observations were several sessions between 2002 May to November and those of ^{13}CO were those between 2003 April to August. All the observations were made by frequency switching whose interval is 20 MHz, corresponding to $\sim$ 50 km s^{-1}. The frequency resolution was 35 kHz, corresponding to a velocity resolution of $\sim$ 0.1 km s^{-1}. The half-power beam width was about $2'.6$, corresponding to 0.076 pc at a distance of 100 pc. The integration times per point of ^{12}CO and ^{13}CO observations were typically $\sim$ 30 s and $\sim$ 75 s, respectively, resulting in typical rms noise temperatures per channel of $\sim$ 0.35 K and $\sim$ 0.15 K in the radiation temperature, $T_{\rm R}^{*}$, respectively. In reducing the spectral data, we subtracted forth-order polynomials for the emission-free parts in order to ensure a flat spectral baseline. Total numbers of observed points of ^{12}CO and ^{13}CO are 16890 and 3100, respectively.

We employed a room-temperature blackbody radiator and the sky emission for the intensity calibration. An absolute intensity calibration and the overall check of the whole system were made by observing Orion KL [$\alpha(1950) = 5^{\rm h}32^{\rm m}47.^{\rm s}0$, $\delta(1950) = -5°24'21''$] every 2 hours. We assumed the $T_{\rm R}^{*}$ of Orion KL to be 65 K for ^{12}CO and 10 K for ^{13}CO.

4.3 Results

4.3.1 ^{12}CO Observation

4.3.1.1 Distribution and Past Detection of ^{12}CO Clouds

Figure 4–1 shows the distribution of the velocity-integrated intensity map of ^{12}CO emission. We defined a ^{12}CO cloud as a collection of more than two contiguous observed positions whose integrated intensity exceeds 0.77 K km s^{-1} (5σ). Based on the definition, we identified 78 molecular clouds in this region. Molecular clouds are concentrated from (l, b) $\sim$ (107°, −37°) to (116°, −45°) and around (l, b) $\sim$ (114°, −52°). Most of the molecular clouds are very small, having size of $\lesssim$ 1°. Figure 4–2 shows the distribution of the CO superposed on the SFD 100 μm (Schlegel et al. 1998), which was derived from a composite of the COBE/DIRBE and IRAS/ISSA maps, with the foreground zodiacal light and confirmed point sources removed. CO clouds are distributed along the infrared loop whose diameter is $\sim$ 25 pc. We detected little CO emission within the loop-like structure, while toward some of the local peaks of SFD 100 μm there is no CO emission.

Figure 4–3 shows the peak radial velocity distribution derived from the present ^{12}CO data set. The velocity in Figure 4–3 is derived by a single gaussiun fitting from all CO spectra. The velocity range of the molecular clouds is from −18.3 km s^{-1} to 0.3 km s^{-1} and there is no systematic large scale velocity gradients.

Some of the molecular clouds have already been known by previous observations. Molecular clouds toward (l, b) $\sim$ (110°.18, −41°.23) and (117°.36, −52°.28) are identified by Magnani et al. (1985) and named as MBM 1 and MBM 2, respectively. DIR117−44 and DIR105−38 identified by Reach et al. (1998) are also identified in CO toward (l, b) $\sim$ (116°.5, −44°.0) and (105°.0, −38°.0) in Chapter 2. Magnani et al. (1986) detected CO emission at (l, b) $\sim$ (112°, −40°). Magnani et al. (2000) also covered this region even though they made observations on a locally Cartesian grid with 1°(true angle) spacing in longitude and latitude for abeam size of 8′.8, they detected CO emission at eight positions of (l, b) $\sim$ (103°.2, −38°.0), (103°.2, −39°.0), (104°.4, −39°.0), (106°.8, −37°.0), (108°.0, −52°.0), (109°.5, −51°.0), (110°.4, −41°.0), and (111°.0, −50°.0) in the present region while they missed the present small molecular clouds whose sizes are less than several arc min in Figure 4–1 due to the coarse grid spacing.

4.3.1.2 Physical Properties of ^{12}CO Molecular Clouds

Seventy eight ^{12}CO molecular clouds are identified in the present region. For each molecular cloud, ΔV derived from single Gaussian fitting was from 0.5 to 3.7 km s^{-1}, and the radial velocity, $V_{\rm LSR}$, ranges from -15.7 to -0.1 km s^{-1}. The maximum brightness temperature, $T_{\rm R}^{*}(^{12}{\rm CO})$ ranges from 0.5 to 5.7 K. The radius of a cloud, R, which is defined as the radius of an equivalent circle having the same area, i.e., and $R({\rm pc})=\sqrt{A/\pi}$ where A is the total cloud surface area within the 5σ–contour level, ranges from 0.07 to 0.79 pc. The peak column density of molecular hydrogen, $N({\rm H_2})$, in each cloud derived by assuming a conversion factor of 1.0×10^{20} cm^{-2}/(K km s^{-1}) (Magnani et al. 2000) ranges from 8.0×10^{19} to 1.7×10^{21} cm^{-2} with the present detection limit, 7.7×10^{19} cm^{-2}, corresponding to mass detection limit of 0.014 $M_{\odot}$. We estimate the molecular mass, $M(^{12}{\rm CO})$, by using the following formula

$$M(^{12}{\rm CO}) = \mu m_{\rm H}\Sigma[D^2\Omega N({\rm H_2})], \tag{4.1}$$

where μ is the mean molecular weight, assumed to be 2.8 by taking into account a relative helium abundance of 25% in mass, $m_{\rm H}$ the mass of the atomic hydrogen, D the distance from the Sun to the molecular clouds, and Ω the solid angle subtended by a unit grid spacing of $(4')\times(4'\times\cos(b))$. $M(^{12}{\rm CO})$ ranges from ~ 0.04 to ~ 11 $M_{\odot}$ and the total mass of molecular clouds is ~ 64 $M_{\odot}$. These physical properties are listed in Table 4–1 and the histograms of ΔV, $\log(N({\rm H_2}))$, $\log(R)$ and $\log(M(^{12}{\rm CO}))$ of these clouds are shown in Figure 4–4. Histograms in Figure 4–4 are divided to three different categories, *Usual Cloud* (hereafter UC) whose mass is greater than 1 $M_{\odot}$, *Small Cloud* (hereafter SC) whose mass is between 0.1 and 1 $M_{\odot}$, and *Very Small Cloud* (hereafter VSC) whose mass is less than 0.1 $M_{\odot}$. It is remarkable that there are a number of molecular clouds having mass less than 1 $M_{\odot}$ and that the fraction of SC and VSC is $43/78 \sim 55\%$ and $22/78 \sim 28\%$ in the present region, respectively. In addition, the sizes of SC and VSC are equal to or less than 0.1 pc. We also note that the peak temperatures of SC and VSC are typically in a range from 0.5 K to 2.7 K, well below that of UC in the same region.

4.3.2 The Detection and Physical Properties of the ^{13}CO Molecular Clouds

Figure 4–5 shows the distribution of the velocity-integrated intensity map of the ^{13}CO emission superposed on the ^{12}CO distribution. The total area of the ^{13}CO

observations is $\sim$ 29 square degrees toward 38 of the 78 ^{12}CO clouds. We observed all of 13 UCs, 24 of 43 SCs, and 3 of 22 VSCs. We detected ^{13}CO emission at 11 of the 13 UCs, 8 of the 24 SCs, and none of the 3 VSCs, indicating a trend that the ^{13}CO intensity increases with ^{12}CO cloud mass.

A ^{13}CO cloud is defined in the same way as for a ^{12}CO cloud except for the lowest integrated intensity level, 0.3 K km s^{-1} (3σ). Based on the definition, we identified 33 ^{13}CO clouds. For the 33 ^{13}CO molecular clouds, ΔV derived from single Gaussian fitting is $\sim$ 1.5 km s^{-1} and $V_{\rm LSR}$ of them ranges from -13.1 to -1.9 km s^{-1}. Other physical properties, the maximum brightness temperature, $T_{\rm R}^{*}(^{13}{\rm CO})$, and R range from 0.3 to 2.3 K and from 0.04 to 0.21 pc, respectively. The physical parameters including the molecular column density and mass (hereafter $M_{\rm LTE}$) are derived on the assumption of local thermodynamic equilibrium (LTE). To derive the column density of molecular hydrogen, the optical depth of ^{13}CO is estimated by using the following equations,

$$\tau(^{13}{\rm CO}) = \ln\left[1 - \frac{T_{\rm R}^{*}(^{13}{\rm CO})}{5.29}\left\{\frac{1}{\exp(5.29/T_{\rm ex}) - 1} - 0.164\right\}^{-1}\right], \qquad (4.2)$$

where $T_{\rm ex}$ is the excitation temperature of the J = 1–0 transition of CO in K and was derived from

$$T_{\rm ex} = \frac{5.53}{\ln\{1 + 5.53/\left[T_{\rm R}^{*}(^{12}{\rm CO}) + 0.819\right]\}}. \qquad (4.3)$$

$T_{\rm ex}$ was estimated to be 9.4 K from our ^{12}CO data. The ^{13}CO column density, $N(^{13}{\rm CO})$, is estimated by

$$N(^{13}{\rm CO}) = 2.42 \times 10^{14} \times \frac{\tau(^{13}{\rm CO})T_{\rm ex}({\rm K})\Delta V({\rm km\ s^{-1}})}{1 - \exp[-5.29/T_{\rm ex}({\rm K})]}({\rm cm^{-2}}). \qquad (4.4)$$

The ratio of $N({\rm H_2})/N(^{13}{\rm CO})$ was assumed to be 7×10^5 (Dickman 1978). The $M_{\rm LTE}$ of a cloud from $N({\rm H_2})$ is derived by the same way as ^{12}CO (see equation (1)). The column density and $M_{\rm LTE}$ range from 2.3×10^{20} to 1.7×10^{21} cm^{-2} and 0.03 to 1.41 $M_\odot$, respectively, where the detection limit in the column density is 2.0×10^{20} cm^{-2}, coressponding to mass limit of 0.009 $M_\odot$, smaller than it of ^{12}CO because the observations of ^{13}CO were made by higher grid sampling and lower rms noise fluctuation than those of ^{12}CO. Figure 4–6 shows the histograms of each physical property. The virial mass, $M_{\rm vir}$, of a cloud was derived by using the following

equation, assuming isothermal, spherical, and uniform density distribution with no external magnetic pressure:

$$M_{\rm vir} = 209 \times R \times \Delta V^2_{\rm comp}, \tag{4.5}$$

where R and $\Delta V_{\rm comp}$ are the radius (pc) and line width (km s^{-1}) of the composite profile obtained by averaging all of the spectra within the cloud, respectively (for details of the line width of composite profiles, see Yonekura et al. 1997; Kawamura et al. 1998). From this equation, $M_{\rm vir}$ is estimated to be in a range from 4.7 to 197 $M_\odot$. These physical properties are also listed in Table 4–2.

4.4 Correlations Among Cloud Physical Parameters

4.4.1 Mass Spectrum and Size Linewdith Relation

Figure 4–7a and 4–7b show the mass spectrum of the present ^{12}CO and ^{13}CO clouds. The spectra have been fitted by the maximum-likelihood method (Crawford et al. 1970), and it is found that they are well fitted by a single power law as follows; $dN/dM \propto M^{-1.53\pm0.13}$ for the ^{12}CO clouds and $dN/dM \propto M^{-1.36\pm0.10}$ for the ^{13}CO clouds. These values of the spectral indices seem to be similar to those for the higher mass range (e.g., Yonekura et al. 1997).

Figure 4–8 shows a plot of size, R, versus line width, ΔV, of the ^{13}CO clouds in this region and for a comparison with other HLCs, MBM 53, 54, and 55 complex in Chapter 3. We can make fitting as follows by using a least-squares fitting, $\log(\Delta V) = (0.22\pm0.43) \times \log(R) + (0.37\pm0.52)$ (c.c.=0.23) for the present region and $\log(\Delta V) = (0.43\pm0.32) \times \log(R) + (0.53\pm0.28)$ (c.c.=0.37) for MBM 53, 54, and 55 complex. The low correlation coefficient (c.c.) indicates that there is no correlation between R and ΔV because of small range of R. Here we do not show the same relationship for ^{12}CO, because the mon-circular shape of the ^{12}CO clouds may not be appropriate to derive reliable R.

4.4.2 $M_{\rm LTE}$ vs. $M_{\rm vir}$

Figure 4–9 shows a plot of $M_{\rm LTE}$ versus $M_{\rm vir}$. The present ^{13}CO clouds are located far above the equilibrium line where $M_{\rm LTE}$ is equal to $M_{\rm vir}$, indicating that the clouds

are in the virial equilibrium. This indicates that none of the molecular clouds are gravitationally bound. These parameters can be fitted by using a least-squares fitting as follows, $\log(M_{\rm vir}) = (0.91\pm0.30) \times \log(M_{\rm LTE}) + (2.23\pm0.29)$ (c.c.=0.66) for present molecular clouds and $\log(M_{\rm vir}) = (0.77\pm0.13) \times \log(M_{\rm LTE}) + (0.16\pm0.08)$ (c.c.=0.74) for MBM53, 54, and 55 complex. As mentioned in Chapter 3, the present molecular clouds also tend to be more virialized as the mass increases. For the Gemini and Auriga, and Cepheus-Cassiopeia region, the indices of $M_{\rm LTE}$ for $M_{\rm vir}$ of ^{13}CO clouds were estimated to be 0.72±0.03 and 0.62±0.03 for the cloud mass range of $M_{\rm LTE} < 10^4\ M_\odot$ and $10^2\ M_\odot < M_{\rm LTE} < 10^5\ M_\odot$, respectively (Kawamura et al. 1998; Yonekura et al. 1997). Although the mass ranges of MBM 53, 54, and 55 complex and of this region are $10^{-1}\ M_\odot < M_{\rm LTE} < 10^2\ M_\odot$ and $10^{-2}\ M_\odot < M_{\rm LTE} < 1\ M_\odot$, respectively, difference in the power-law indices among these regions is small and a tendency that the SCs have large ratios of $M_{\rm vir}/M_{\rm LTE}$ is commonly seen.

4.5 Comparison with the Other Wavelength Data

4.5.1 No Sign of Star Formation

In order to look for sings of star formation associated with the present molecular clouds, we searched the IRAS point source catalog for candidates of protostellar objects satisfing the following criteria: (1) point sources having a data quality flag better than 2 in 4 bands, (2) flux ratios at 12, 25, 60 μm satisfying both $\log(F_{12}/F_{25}) < -0.3$ and $\log(F_{25}/F_{60}) < 0$, and not identified as galaxies or planetary nebulae and stars. We find that there are no cold IRAS point sources satisfying these criteria in the present molecular clouds. We also find that there are no IRAS point sources having a spectrum like a T-Tauri type star or no YSOs identified from Point Source Catalog of Two-Micron All-Sky Survey in this region. Here we select the 2MASS sources whose signal to noise ratio of valid measurements in all bands are greater than 10. These results suggest that the present molecular clouds are not the site of recent star-formation, or that the region is not remnants of past star formation. Such a low level of star formation is similar to the other HLCs including MBM 53, 54, and 55 complexes.

4.5.2 Comparison with HI

Figure 4–10 shows the integrated intensity map of H I taken from a Leiden-Dwingeloo H I survey (Hartmann & Burton 1997) superposed on the integrated intensity of CO. The integrated velocity range is from -16 to 0 km s^{-1}, corresponding to the velocity range of the ^{12}CO emission. Because the angular resolution of $\sim 30'$ is coarser than that of the present CO observations by a factor of ~ 10, we discuss here only the overall comparison between CO and H I distributions. The H I distribution is loop-like and the molecular clouds are distributed nearly along the H I loop.

Figure 4–11 shows the position-velocity diagram of H I integrated from $-40°.5$ to $-39°.5$ and $-52°.5$ to $-51°.5$ in Galactic latitude, respectively. The hole like structures can be seen in H I, indicating that these H I clouds are expanding. Two expanding shells in L-B map are shown in the thick dotted lines in Figure 4–10, where Figure 4–11(a) and 4–11(b) correspond to the Galactic northern and southern expanding shell in Figure 4–10, respectively. But the expanding motion is not in CO (See Figure 4–3). These two expanding shells are also identified by an infrared radiation (Kiss et al. 2004). From Figure 4–10, an H I cloud around (l, b) $\sim$ (109°, $-52°$) seems to be located at the left side of the Galactic southern expanding shell and the molecular cloud is associated with it. It is difficult to distinguish whether molecular clouds located around (l, b) $\sim$ (109°, $-52°$) are associated with two expanding shells because the H I velocities of the two shells are similar with each other. The shape of ^{12}CO and SFD100 μm radiation around (l, b) $\sim$ (109°, $-52°$) in Figure 4–2 is also similar to the left side of the expanding shell. If this is true, there may be two expanding structures in the present region. HD886 (109°.43, $-46°.68$) is located near the center of the Galactic northern expanding shell, indicating that HD886 may be affecting the Galactic northern expanding shell. The parallax of HD886 has been measured to be 9.79$\pm$0.81 mas (Perryman et al. 1997), corresponding to a distance from the Sun of 102^{+9}_{-8} pc. The proper motion has also been measured to be $\mu\alpha*$=0″.0047 yr^{-1}, $\mu\delta$=$-$0″.0082 yr^{-1} by Perryman et al. (1997). From this proper motion, the velocity of HD886 in L-B map is estimated to be $\sim 4.3\times10^{-6}$ pc yr^{-1} at $\sim$ 100 pc (see Figure 4–10). We use typical values of the stellar wind for B2(IV) star on dM/dt=10^{-9} $M_\odot$ yr^{-1} and V_∞ = 1000 km s^{-1} (e.g., Snow 1982). From these parameters, the energy injected to the Galactic northern expanding shell is estimated to be $\sim 10^{47}$ ergs in a few $\times10^6$ yr. The expanding energy of the Galactic northern expanding shell is estimated to be $\sim 10^{47}$ ergs from the atomic and molecular hydrogen, using that the masses of amomic and molecular hydrogen associated with the

Galactic northern expanding shell are $\sim$ 400 and 42 $M_{\odot}$, respectively, the expanding velocity is $\sim$ 7 km s^{-1} which is estimated from Figure 4–11 and the equation of $E_{\rm exp}$=1/2$MV_{\rm exp}^2$. Since the expanding energy of the atomic and molecular hydrogen is comparable to the energy from HD886, additional source of energy other than HD886 is needed to explain the expanding energy because a conversion efficiency of the energy of the stellar wind is $\lesssim$ 10%. The energy of the Galactic southern expanding shell is estimated to be $\sim 10^{47}$ ergs, using that the masses of atomic and molecular hydrogen are $\sim$ 1000 and 16 $M_{\odot}$,respectively, the expanding velocity is $\sim$ 9 km s^{-1} and the same equation above. We could not find possible candidates of the energy source for the expanding feature in the literature using SIMBAD and there are no counterparts in optical or X-ray wavelength. Although we could not identify the possible candidates, it is possible that these objects may have disappeared in a few $\times$ $10^{6\sim7}$ yr after forming these structures.

4.6 Discussion

4.6.1 Physical States of the Small Clouds

The present observations have revealed numerous molecular clouds having very small mass of less than 1 $M_{\odot}$. It is of considerable interest to pursue the physical states of these SCs from view points of cloud physics and chemistry as well as of the origin of molecular clouds.

We shall hereafter focus on the low mass ^{12}CO clouds whose mass is less than 1 $M_{\odot}$. The total number of such clouds is 65 among 78. The ^{13}CO emission has been searched for toward 24 of the 43 ^{12}CO low-mass clouds whose mass is in a range of 0.1–1.0 $M_{\odot}$ and has been detected from 8 of them. Figure 4–12 shows correltions of the molecular column density, estimated from ^{12}CO and ^{13}CO, of the clouds whose both ^{12}CO and ^{13}CO emission were observed. It is seen that almost all of ^{12}CO clouds having molecular column density greater than 5×10^{20} cm^{-2}, corresponding to the visual extinction of 0.55 mag if we use the relationship of $N(\rm H_2)$=$9.4\times10^{20}\times A$v cm^{-2} (Bohlin et al. 1978; Hayakawa et al. 1999), show significant ^{13}CO emission. We note that there are 22 ^{12}CO clouds whose mass is less than 0.1 $M_{\odot}$; for those it is doubtful that the ^{13}CO emission is so significant as those whose mass is a range of 0.1–1.0 $M_{\odot}$ although only 3 of them were searched for the ^{13}CO emission in the present study. We note that we ignore the contribution of atomic hydrogen in above relationship. If we take into account the distribution of atomic hydrogen in N(H I),

the visual extinction would increase 0.2 $\sim$ 0.3 mag. This may be explained as that the ^{13}CO emitting regions become significant when Av becomes larger than $\sim$ 1 mag, marginally enough to shield the ultraviolet radiation to protect ^{13}CO molecules (e.g., Warin et al. 1996).

The peak intensity ratio of ^{12}CO and ^{13}CO is around 5 much smaller than the terrestrial abundance ratio of 89, indicating that the ^{12}CO emission is optically thick in the clouds where the both emissions are detected. The maximum ^{12}CO peak temperature of the present brightest ^{12}CO emission is 6 K, and this suggests that the excitation temperature is consistent with the kinetic temperature of $\sim$ 10 K typical to the local dark clouds. The low mass clouds show lower ^{12}CO peak temperatures down to 1 K, significantly less than the brightest peak intensities. It is not clear if this is due to the lower excitation temperatures or due to smaller filling factors less than 1. In order to clarify this point we need further observations of the present low mass clouds at much higher angular resolutions.

4.6.2 Origin of the Very Small Clouds

Figure 4–13 shows the histograms of mass and sizes of ^{12}CO clouds. In the present region, we have detected a large number of molecular clouds of mass less than 0.1 $M_{\odot}$ and sizes less than 0.1 pc not detected so far in the other regions. We may ask why molecular clouds of mass less than 0.1 $M_{\odot}$ and size less than 0.1 pc such as the present clouds have not been detected so far. The main reason for this is perhaps the paucity of high-resolution observational studies of nearby molecular clouds. Most of the observations of the local high latitude clouds were made at lower resolutions of 10 arc-min or at a coarse grid spacing of 1 degree, both of which are unable to resolve the present low mass clouds. This suggests that the low mass clouds similar to the present ones may not be uncommon in the interstellar space and warrant more extensive searches for them in the other parts in the sky.

It is interesting to compare the physical parameters of the present VSCs with theoretical predictions. The typical size of these HLCs $\sim$ 0.1 pc is significantly less than the Jeans length of 1.3 pc – 7 pc for molecular gas with T=10 K and $n(H_2)$=10–100 cm^{-3}. If we take temperature higher than 10 K, the length becomes even larger. Figure 4–14 shows the radial distribution of mass surface density which is derived by dividing the mass in circular ring of a radius by the area of the circular ring. Mass surface density in the present region is fairly flat for radius because there is no massive molecular cloud in the center of the VSCs. On the other hand, mass surface density in the other regions has a gradient for radius, indicating that

there are small molecular clouds around a massive molecular cloud whose mass is several dozen $M_{\odot}$ or greater. In these regions, the gravity of the massive molecular cloud may contribure to the formation of these small clouds. These suggest that mechanisms other than gravitational instability might contribute to the formation of present VSCs. A theory of molcular cloud formation is discussed by Koyama & Inutsuka (2002). According to them, molecular clouds smaller than the Jeans-length can be formed in the shocked layer through the thermal instability.

Present VSCs are likely to be affected by HD886 in a few $\times 10^6$ yr (for details, see section 5.2). Although the mechanical luminosity from HD886 injected to the loop-like structure during a few $\times 10^6$ yr is low to expain the expanding of the interstellar matter, there is a possibility that the stellar wind of HD886 is the source of shock. Koyama & Inutsuka (2002) assumed shock velocity of 26 km s^{-1} and density of 0.6 cm^{-3} as an initial condition and they found that the region of density greater than 100 cm^{-3} grows in the size of $\sim 0.2 \times 0.1$ pc in 1.06×10^6 yr and the internal structure consists of some filaments. The velocity dispersion of CO derived by Koyama & Inutsuka (2002) is a few km s^{-1}. The size of the smallest molecular clouds and the velocity dispersion of CO are comparable to those derived from Koyama & Inutsuka (2002). We can not resolve the internal structure of the VSCs because present VSCs are detected with only a few points. The typical column density derived by Koyama & Inutsuka (2002) becomes 2×10^{20} cm^{-2}, while the column density of the VSCs is estimated to be $\sim 1.6 \times 10^{20}$ cm^{-2} (see Figure 4–4). The surface filling factor of the region of density greater than 100 cm^{-3} in Koyama & Inutsuka (2002) is roughly estimated to be 30–40%. In this surface filling factor the column density estimated from the observations is consistent with that derived from Koyama & Inutsuka (2002) and the low temperature of the VSCs is consistent with the result that their peak temperature is lower than that of the typical local dark clouds. These results may indicate that there is a possibility that the present VSCs are formed in the shock compressed layer through thermal instability. In order to compare the observational results with the theoretical simulation on internal temperature and density structure in more details, the observations of higher resolutions are needed.

4.7 Conclusions

We have made a large-scale survey of high Galactic latitude molecular clouds in the $J = 1$–0 lines of ^{12}CO and ^{13}CO toward a large scale structure located around $(l, b) \sim (109°, -45°)$ with NANTEN. This survey spatially resolved the distribution

of molecular gas associated with the large scale structure. The main conclusions of the present study are summarized as follows:

1. The ^{12}CO observation covered the entire large loop-like structure. The loop-like structure consits of very small clumpy clouds. The ^{12}CO clouds are concentrated on the north to north-west of the loop-like structure and toward the south of that. We identified 78 ^{12}CO clouds in the observed region. The total mass is estimated to be $\sim 64\ M_{\odot}$ if we assume the conversion factor from CO intensity to $N(H_2)$ as 1.0×10^{20} cm^{-2}/(K km s^{-1}).

2. We performed ^{13}CO observations in and around the whole area where the peak temperature of ^{12}CO is more than 2.0 K. We identified 33 ^{13}CO clouds and derived physical properties under the assumption of LTE.

3. The mass spectra are well fitted by a power law, $dN/dM \propto M^{-1.53\pm0.13}$ for the ^{12}CO clouds and $dN/dM \propto M^{-1.36\pm0.10}$ for the ^{13}CO clouds. These spectrum indices are similar to those derived in other regions.

4. The size and the line width relation of ^{13}CO clouds is fitted by a least-squares method, $\log(\Delta V) = (0.22\pm0.43) \times \log(R) + (0.37\pm0.52)$ (c.c.=0.23), but the correlation is not good.

5. Present ^{13}CO clouds are far from the virial equilibrium, indicating that ^{13}CO clouds are not gravitationally bound. $M_{\rm vir}$ and $M_{\rm LTE}$ relation can be fitted by a least-squares method as $\log(M_{\rm vir}) = (0.91\pm0.30) \times \log(M_{\rm LTE}) + (2.23\pm0.29)$ (c.c.=0.66). This index is slightly different from the indices in the other regions although the tendency that molecular clouds are more vilialized as the mass increases is consistent with the other regions.

6. There is no sign of star formation from the comparison of IRAS point sources and Point Source Catalog of Two-Micron All-Sky survey in the present region. This suggests that molecular clouds in this region are not the site of present star formation or the remnants of past star formation.

7. There may be two expanding shells in the present region as inferred from H I although we can not identify them from CO. The total mechanical luminosity of HD886 during a few $\times\ 10^6$ yr is comparable to the expanding energy of the Galactic northern expanding H I shell. This indicates that additional source of energy other than HD886 is needed to explain the expanding energy.

8. ^{13}CO emission is significantly detected in the ^{12}CO clouds having molecular column density greater than 5×10^{20} cm^{-2}. This may be explained as that the ^{13}CO emitting regions become significant when Av becomes larger than $\sim$ 1 mag, marginally enough to shield the ultraviolet radiation to protect ^{13}CO molecules.

9. There is a possibility that very small clouds have been formed in the shoked layer through the thermal instability. The stellar wind of HD886 may be the source to creat shocks, forming the loop-like structure where the very small clouds are embedded.

References

Bhatt, H. C. 2000, A&A, 362, 715

Blitz, L., Bazell, D., & Desert, F. X. 1990, ApJ, 352, 13

Bohlin, R. C., Savage, B. D.,& Drake, J. F. 1978, ApJ, 224, 132

Crawford, D. F., Jauncey, D. L., & Murdoch, H. S. 1970, ApJ, 162, 405

Dickman, R. L. 1978, ApJS, 37, 407

Gir, B. Y., Blitz, L., & Magnani, L. 1994, ApJ, 434, 162

Hartmann, D., & Burton, W. B. 1997, Atlas of Galactic Neutral Hydrogen. Cambridge Univ. Press, Cambridge

Hartmann, D., Magnani, L., & Thaddeus, P., 1998, ApJ, 492, 205

Hayakawa, T., Mizuno, A., Onishi, T., Yonekura, Y., Hara, A., Yamaguchi, R., & Fukui, Y. 1999, PASJ, 51, 919

Hearty, T., Magnani, L., & Caillault, J. P. 1999, A&A, 341, 163

Heithausen, A., & Thaddeus, P. 1990, ApJ, 353, L49

Kawamura, A., Ohnishi, T., Mizuno, A., Ogawa, H., & Fukui, Y., 1998, ApJS, 117, 387

Keto, E. R., & Myers, P. C. 1986, ApJ, 304, 466

Kiss, Cs., Moór, A., Tóth, L. V. 2004 A&A, 418, 131

Koyama, H., & Inutsuka, S. 2002, ApJ, 564, 97

Magnani, L., Blitz, L., & Mundy, L. 1985, ApJ, 295, 402 (MBM)

Magnani, L., Blitz, L., & Lada, E. A. 1986, ApJ, 301, 395

Magnani, L., Caillault, J. P., Buchalter, A., & Beichman, C. A. 1995, ApJS, 96, 159

Magnani, L., Hartmann, D., & Speck, B, G., 1996, ApJS, 106, 447

Magnani, L., Hartmann, D., Holcomb, S. L., Smith, L. E., & Thaddeus, P. 2000, ApJ, 535, 167

Ogawa, H., Mizuno, A., Hoko, H., & Fukui, Y. 1990, Int. J. Infrared Millimeter Waves, 11, 717

Onishi, T., Yoshikawa, N., Yamamoto, H., Kawamura, A., Mizuno, A., & Fukui, Y. 2001, PASJ, 53, 1017

Perryman, M.A.C., et al. 1997, A&A, 323, L49(Hipparcos Catalogue)

Pound, M. W. 1996, ApJ, 457, 35

Pound, M. W., & Goodman, A. A. 1997, ApJ, 482, 334

Reach, W. T., Koo, B. C., & Heiles, C. 1994, ApJ, 429, 672

Reach, W. T.,Wall, W. F., & Odegard, N. 1998, ApJ, 507, 507

Schlegel, D. J., Finkbeiner, D. P., & Davis, M. 1998, ApJ, 500, 525

Snow, T. P. Jr 1982, ApJ, 253, L39

van Dishoeck, E. F., & Black, J. H., 1988, ApJ, 334, 771

Warin, S., Benayounm, J. J., & Viala, Y. P. 1996, A&A, 308, 535

Yamamoto, H., Onishi, T., Mizuno, A., & Fukui, Y. 2003, ApJ, 592, 217

Yonekura, Y., Dobashi, K., Mizuno, A., Ogawa, H., & Fukui, Y., 1997, ApJS, 110, 21

Table 4–1. Physical Properties of ^{12}CO Clouds

No. (1)	l (2)	b (3)	T_R^* (4)	ΔV (5)	V_{LSR} (6)	R (7)	$N(H_2)$ (8)	M_{CO} (9)
1	95.52	−50.00	3.2	1.3	−10.7	0.31	4.7	1.07
2	96.11	−53.13	1.1	1.3	−9.4	0.09	0.8	0.07
3	101.43	−41.53	1.5	1.5	−9.5	0.17	1.9	0.27
4	101.91	−41.20	0.7	0.5	−9.5	0.08	0.9	0.04
5	102.09	−41.20	1.9	1.4	−8.9	0.10	3.4	0.12
6	102.19	−41.07	0.9	1.1	−8.9	0.08	1.0	0.04
7	102.80	−40.27	2.5	1.6	−8.4	0.16	4.5	0.30
8	103.32	−40.33	1.1	1.3	−8.3	0.11	1.6	0.11
9	103.47	−40.60	1.0	1.2	−7.3	0.08	1.0	0.04
10	103.74	−39.33	5.2	2.9	−10.1	0.59	12.3	7.02
11	104.20	−38.93	0.8	1.0	−15.7	0.10	2.0	0.09
12	104.48	−38.53	1.4	3.5	−8.6	0.16	4.5	0.44
13	104.81	−38.80	1.4	1.2	−5.0	0.10	1.5	0.08
14	105.07	−38.80	1.1	1.4	−5.7	0.08	1.8	0.06
15	105.08	−52.27	1.0	1.2	−0.1	0.07	1.2	0.04
16	105.10	−38.07	2.5	2.4	−12.7	0.26	5.7	1.19
17	105.22	−53.20	1.2	1.3	−3.7	0.09	1.1	0.05
18	105.40	−48.13	1.6	1.8	−9.0	0.12	3.0	0.20
19	105.77	−38.40	5.6	1.9	−5.0	0.47	10.5	5.60
20	105.80	−39.60	1.7	1.8	−9.8	0.24	3.1	0.70
21	105.82	−54.00	1.1	1.4	−4.8	0.07	1.3	0.04
22	106.76	−36.53	2.7	3.0	−9.8	0.53	8.3	4.29
23	106.97	−37.87	1.7	1.7	−1.2	0.12	3.4	0.17
24	107.32	−37.60	1.2	1.5	−2.3	0.12	1.6	0.11
25	107.38	−52.00	1.0	2.6	−7.5	0.12	2.1	0.13
26	107.87	−53.93	0.8	1.6	−4.9	0.11	1.8	0.11
27	108.21	−53.73	2.2	1.4	−5.1	0.16	2.9	0.25
28	108.33	−53.13	2.2	1.2	−0.2	0.07	3.5	0.08
29	108.78	−52.60	5.7	2.4	−6.6	0.79	16.6	11.13
30	109.00	−52.13	3.3	1.9	−1.5	0.31	5.1	1.43
31	109.00	−50.07	2.5	1.6	−4.7	0.13	5.1	0.26
32	109.11	−50.60	0.9	2.2	−5.9	0.09	1.6	0.06
33	109.17	−37.60	4.0	1.5	−4.4	0.36	5.6	1.83
34	109.55	−52.87	1.3	2.0	−7.1	0.14	2.5	0.16
35	109.68	−38.27	4.6	1.4	−8.1	0.17	5.4	0.52
36	109.76	−38.00	2.7	2.0	−4.9	0.21	4.7	0.63
37	109.78	−53.33	2.8	1.5	−6.4	0.18	2.6	0.30
38	109.84	−50.73	4.0	2.6	−7.8	0.18	5.0	0.40
39	109.85	−38.60	0.8	1.8	−8.1	0.12	2.1	0.13
40	110.05	−50.40	2.1	3.1	−7.4	0.10	3.6	0.14
41	110.06	−41.27	4.4	2.9	−6.1	0.47	10.2	4.21
42	110.32	−48.93	2.9	0.9	−4.2	0.12	2.6	0.17
43	110.94	−41.00	1.3	3.4	−6.3	0.17	5.7	0.67

Table 4–1. (Continued)

No. (1)	l (2)	b (3)	T_R^* (4)	ΔV (5)	V_{LSR} (6)	R (7)	$N(H_2)$ (8)	M_{CO} (9)
44	110.98	−39.13	1.2	2.2	−9.6	0.12	2.9	0.20
45	111.08	−50.13	1.6	1.0	−7.2	0.13	1.7	0.11
46	112.04	−39.87	3.4	2.3	−5.4	0.26	6.4	1.11
47	112.40	−40.07	1.3	2.6	−7.2	0.10	3.6	0.19
48	112.55	−39.60	1.2	1.9	−3.6	0.16	3.0	0.29
49	112.64	−50.07	0.7	1.5	−6.5	0.14	1.7	0.14
50	112.72	−41.13	1.2	1.9	−6.2	0.11	2.4	0.13
51	112.72	−41.13	1.2	1.9	−6.2	0.11	2.4	0.13
52	112.72	−39.67	1.2	2.6	−5.3	0.10	1.9	0.09
53	112.84	−40.27	1.3	1.7	−5.1	0.08	2.9	0.11
54	113.15	−39.47	1.5	1.2	−4.7	0.16	2.5	0.23
55	113.23	−52.07	4.4	1.3	−7.3	0.30	5.7	1.32
56	113.42	−42.33	3.4	2.4	−10.5	0.23	5.9	0.89
57	113.47	−39.20	0.5	1.9	−5.7	0.10	1.4	0.08
58	113.56	−49.93	1.3	0.9	−7.5	0.12	1.1	0.09
59	113.94	−51.67	1.4	1.6	−9.7	0.07	3.2	0.07
60	114.38	−51.73	3.9	1.6	−9.7	0.17	6.7	0.55
61	114.49	−50.80	1.5	1.8	−7.8	0.09	3.2	0.12
62	114.52	−41.53	2.2	1.1	−7.8	0.15	2.1	0.20
63	114.83	−51.07	0.8	1.8	−8.1	0.10	1.4	0.07
64	114.90	−41.73	1.5	1.2	−8.3	0.08	1.1	0.04
65	115.10	−43.80	1.6	1.0	−2.1	0.11	1.5	0.09
66	115.16	−45.33	1.2	1.6	−8.4	0.17	1.6	0.25
67	115.24	−43.40	1.8	2.0	−3.5	0.23	2.7	0.57
68	115.63	−43.60	0.8	1.0	−3.3	0.08	1.6	0.06
69	115.74	−46.20	1.5	1.0	−6.8	0.13	2.3	0.18
70	116.20	−43.73	3.2	1.5	−2.6	0.16	3.6	0.31
71	116.33	−44.80	4.2	2.3	−3.9	0.59	10.0	7.13
72	116.45	−50.53	2.3	1.1	−7.3	0.17	3.5	0.35
73	116.64	−52.33	0.9	1.5	−7.6	0.07	2.1	0.05
74	116.86	−43.87	0.8	3.7	−4.7	0.18	2.9	0.41
75	117.01	−50.73	2.7	0.8	−7.5	0.10	2.0	0.10
76	117.11	−44.33	2.3	1.1	−2.6	0.14	5.1	0.25
77	118.12	−52.13	1.1	1.1	−6.7	0.12	1.8	0.12
78	118.23	−52.67	4.2	2.0	−7.8	0.43	8.8	3.12

Note—Col. (1) : Cloud number, Col. (2)–(3) : Cloud peak (l, b) position in degree, Col. (4) : Peak temperature in K, Col. (5) : Line width of the composite spectrum in km s^{-1}, Col. (6) : Peak velocity of the composite spectrum in km s^{-1}, Col. (7) : Radius of the molecular cloud in pc, Col. (8) : Column density of peak position in 10^{20} cm^{-2}, Col. (9) : Mass of the molecular cloud in $M_\odot$. Col. (4) to (6) are derived by using a single Gaussiun fitting.

Table 4–2. Physical Properties of ^{13}CO Clouds

No. (1)	l (2)	b (3)	T_R^* (4)	ΔV (5)	V_{LSR} (6)	R (7)	$\tau(^{13}CO)$ (8)	$N(H_2)$ (9)	M_{LTE} (10)	M_{vir} (11)
1	103.70	−39.33	1.2	1.5	−9.7	0.13	0.22	10.0	0.56	57.9
2	105.11	−38.03	0.7	1.7	−11.4	0.06	0.11	4.0	0.08	34.6
3	105.12	−37.80	0.7	1.0	−13.1	0.07	0.12	3.6	0.09	13.5
4	105.54	−38.63	0.8	1.1	−5.5	0.09	0.14	2.5	0.17	23.2
5	105.77	−38.37	2.3	1.7	−4.0	0.21	0.46	16.6	1.41	129.8
6	106.93	−36.40	0.7	2.1	−9.4	0.05	0.13	3.7	0.06	45.2
7	107.82	−51.70	1.2	1.6	−5.0	0.08	0.21	7.0	0.21	40.7
8	107.87	−53.93	0.3	1.8	−7.7	0.07	0.13	2.3	0.09	46.4
9	108.10	−53.77	0.8	3.1	−6.2	0.09	0.13	3.7	0.21	176.1
10	108.78	−52.63	1.4	2.0	−4.6	0.14	0.26	11.1	0.87	120.6
11	108.84	−52.03	1.2	0.7	−6.2	0.11	0.21	5.9	0.29	10.6
12	108.89	−52.17	1.3	1.1	−6.9	0.08	0.23	3.8	0.13	18.4
13	109.00	−52.40	1.1	2.1	−7.8	0.12	0.20	6.0	0.41	110.6
14	109.00	−52.13	0.9	1.6	−1.9	0.04	0.15	5.8	0.05	22.5
15	109.16	−51.87	1.0	1.7	−5.8	0.10	0.17	2.3	0.25	57.6
16	109.17	−37.60	0.8	1.0	−4.4	0.05	0.13	2.4	0.05	10.7
17	109.21	−37.80	0.9	0.9	−4.1	0.06	0.16	4.7	0.08	10.6
18	109.34	−37.80	0.7	0.7	−4.5	0.05	0.13	3.2	0.05	4.7
19	109.53	−51.17	0.8	0.9	−6.5	0.05	0.15	2.9	0.04	8.7
20	109.64	−51.57	0.3	2.4	−7.0	0.05	0.12	3.2	0.04	59.7
21	109.72	−38.27	0.9	0.7	−8.1	0.05	0.16	3.2	0.05	5.1
22	109.80	−51.37	0.4	1.5	−6.7	0.05	0.14	2.5	0.04	22.3
23	109.90	−50.73	1.1	1.8	−7.7	0.11	0.19	10.5	0.48	75.3
24	110.11	−41.27	1.0	2.9	−5.6	0.11	0.23	10.1	0.41	197.4
25	110.19	−41.07	0.6	2.0	−7.6	0.04	0.10	2.3	0.03	33.1
26	111.12	−41.00	0.7	1.1	−5.6	0.04	0.12	4.3	0.03	9.4
27	112.08	−39.87	0.8	0.9	−5.1	0.06	0.14	3.7	0.07	9.3
28	113.17	−42.60	0.8	0.9	−10.9	0.04	0.14	3.7	0.04	6.5
29	113.17	−52.03	1.2	0.7	−7.2	0.11	0.22	4.3	0.24	10.6
30	114.32	−51.70	0.8	1.2	−9.7	0.08	0.15	4.8	0.19	24.9
31	115.49	−44.40	0.9	1.0	−3.5	0.10	0.16	3.7	0.20	22.2
32	116.21	−44.97	1.2	1.6	−3.9	0.18	0.22	9.1	1.04	93.9
33	118.19	−52.70	1.5	1.2	−8.1	0.12	0.28	9.6	0.53	36.7

Note—Col. (1) : Cloud number, Col. (2)–(3) : Cloud peak (l, b) position in degree, Col. (4) : Peak temperature in K, Col. (5) : Line width of the composite spectrum in km s^{-1}, Col. (6) : Peak velocity of the composite spectrum in km s^{-1}, Col. (7) : Radius of the molecular cloud in pc, Col. (8) : Optical depth of ^{13}CO, Col. (9) : Column density of peak position in 10^{20} cm^{-2}, Col. (10) : Mass of the molecular cloud assuming the LTE in $M_\odot$, Col. (11) : Virial mass of the molecular cloud in $M_\odot$. Col. (4) to (6) are derived by using a single Gaussiun fitting.

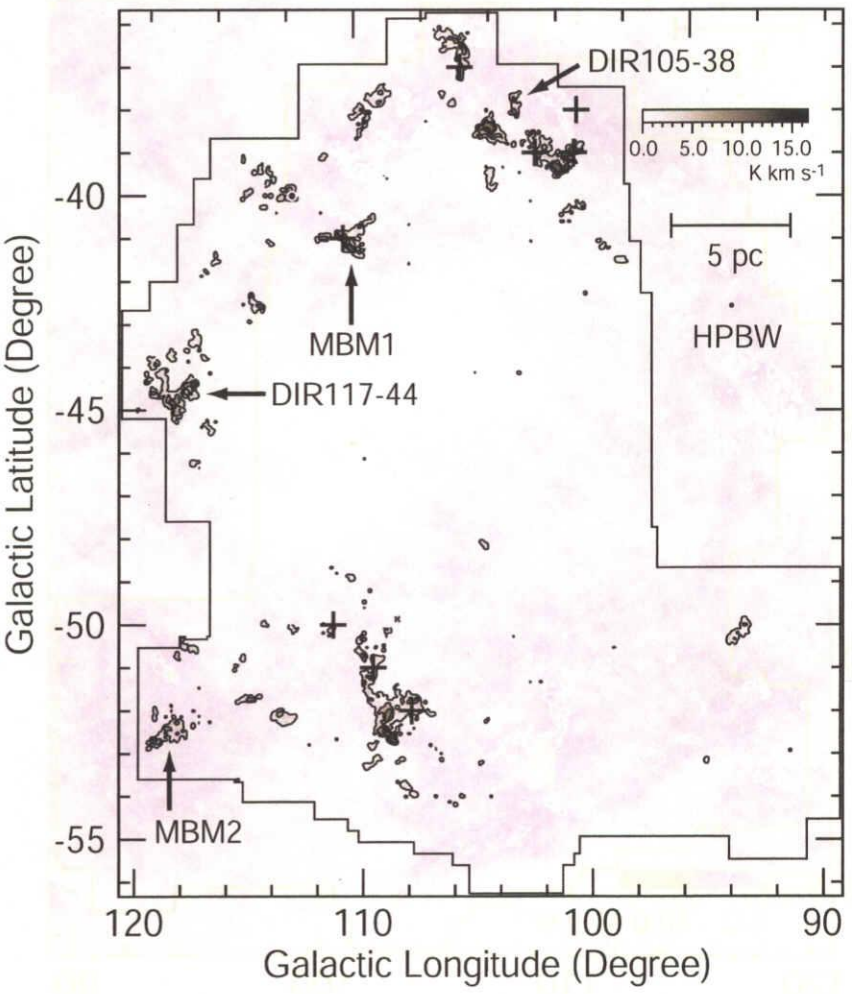

Figure 4–1. Total integrated intensity map of ^{12}CO (J = 1–0) shown in Galacticcoordinates. The lowest contour and the separation between contours are 0.77 and 3.08 K km s^{-1}, respectively. The solid line represents the observed area. The crosses and filled circle indicate the position where Magnani et al. (2000) and (1986) detected ^{12}CO, respectively. The locations of DIR clouds in Reach et al. (1998) and MBM clouds in Magnani et al. (1985) are shown in the figure.

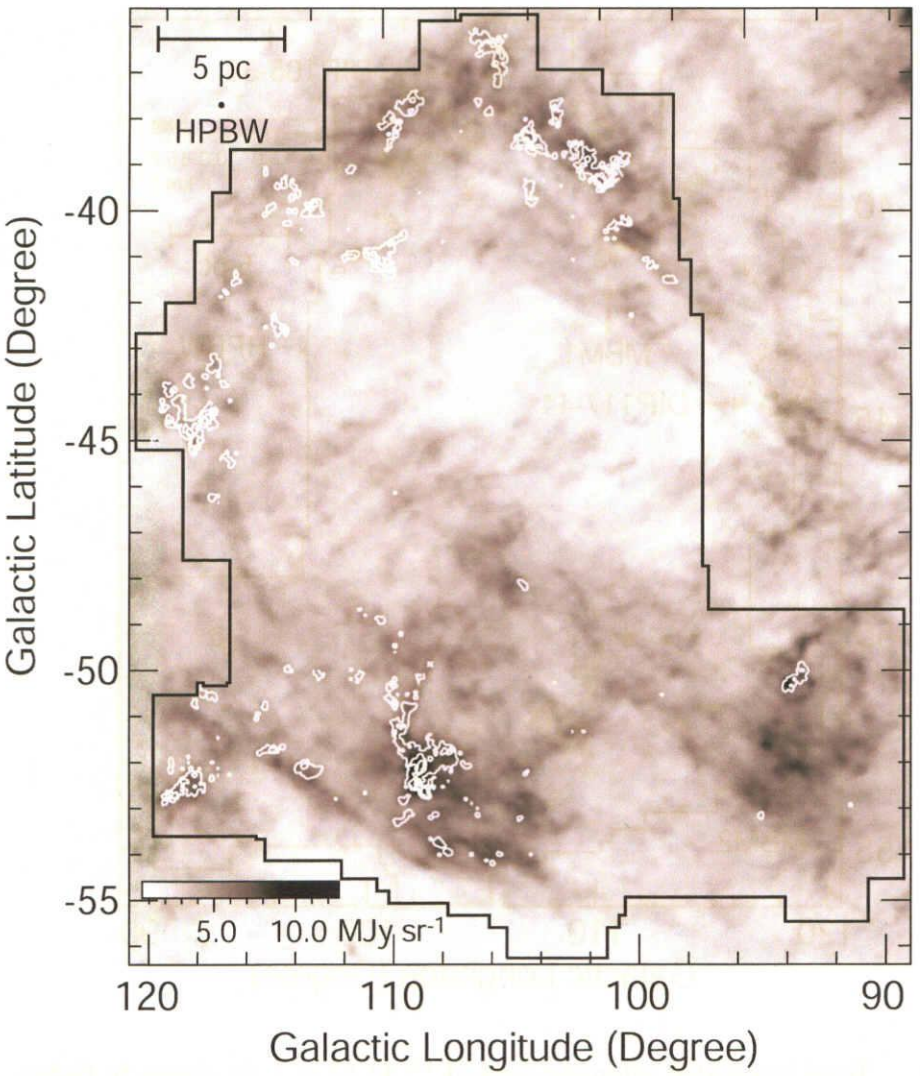

Figure 4–2. Total integrated intensity map of ^{12}CO (J = 1–0) superposed on the SFD 100 μm image derived by Schlegel et al. (1998). The gray scale shows the intensity of 100 μm and white lines represent the integrated intensity of ^{12}CO emission. The lowest contour and the separation between contours are the same as Figure 4–1.

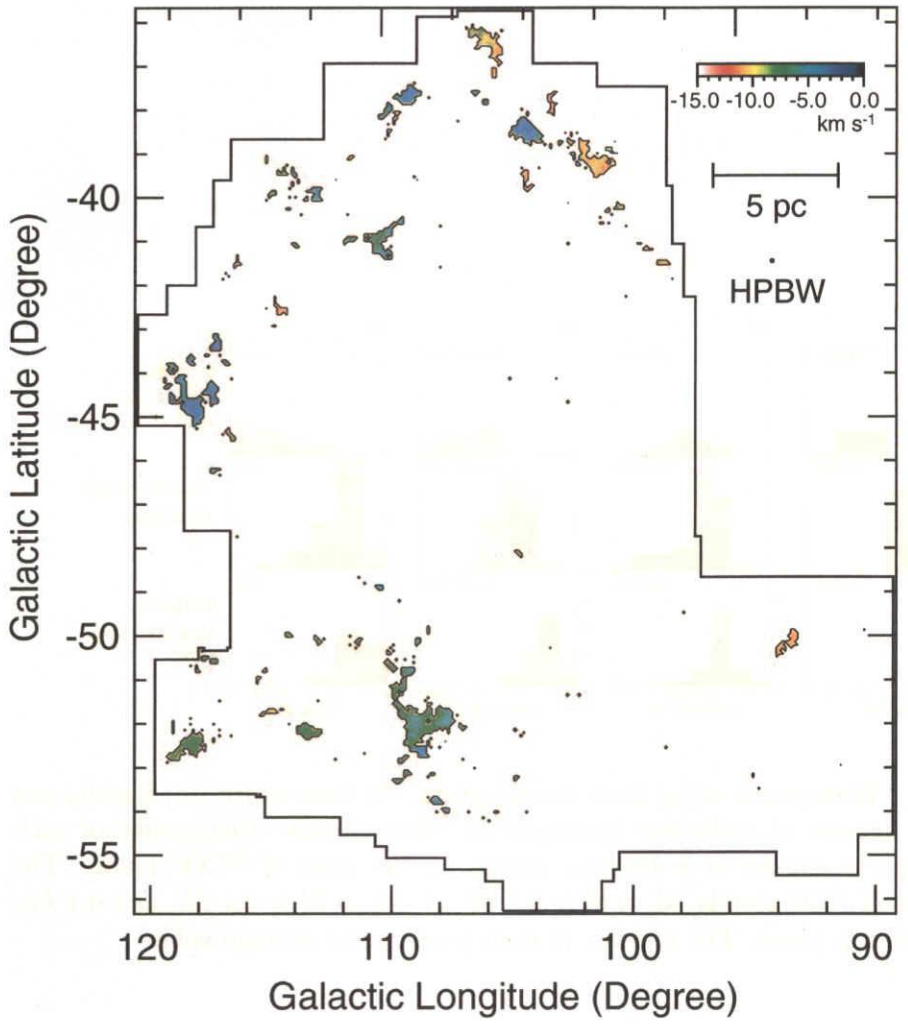

Figure 4–3. The peak radial velocity map of ^{12}CO (J = 1–0) emission. The velocity of ^{12}CO emission is derived from the single gaussian fitting. Solid lines in the observed area show the boundary of the ^{12}CO clouds.

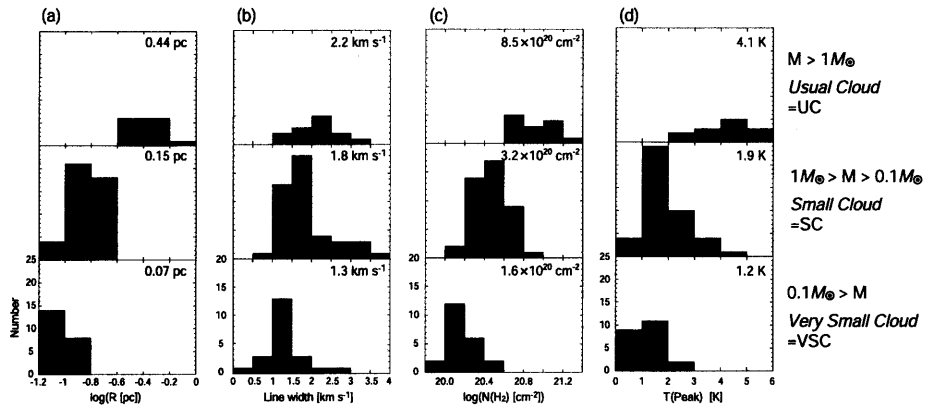

Figure 4–4. Histograms of (a) Peak temperature, (b) Line width, (c) Radius and (d) Column density of molecular hydrogen on ^{12}CO clouds. Histograms of each physical property consist of 3 different ranges on the mass of ^{12}CO clouds. The range of mass of ^{12}CO clouds, M, is M $> 0.1\ M_{\odot}$, $1\ M_{\odot} >$ M $> 0.1\ M_{\odot}$ and $0.1\ M_{\odot} >$ M from the top panel. The number in each panel is the average value.

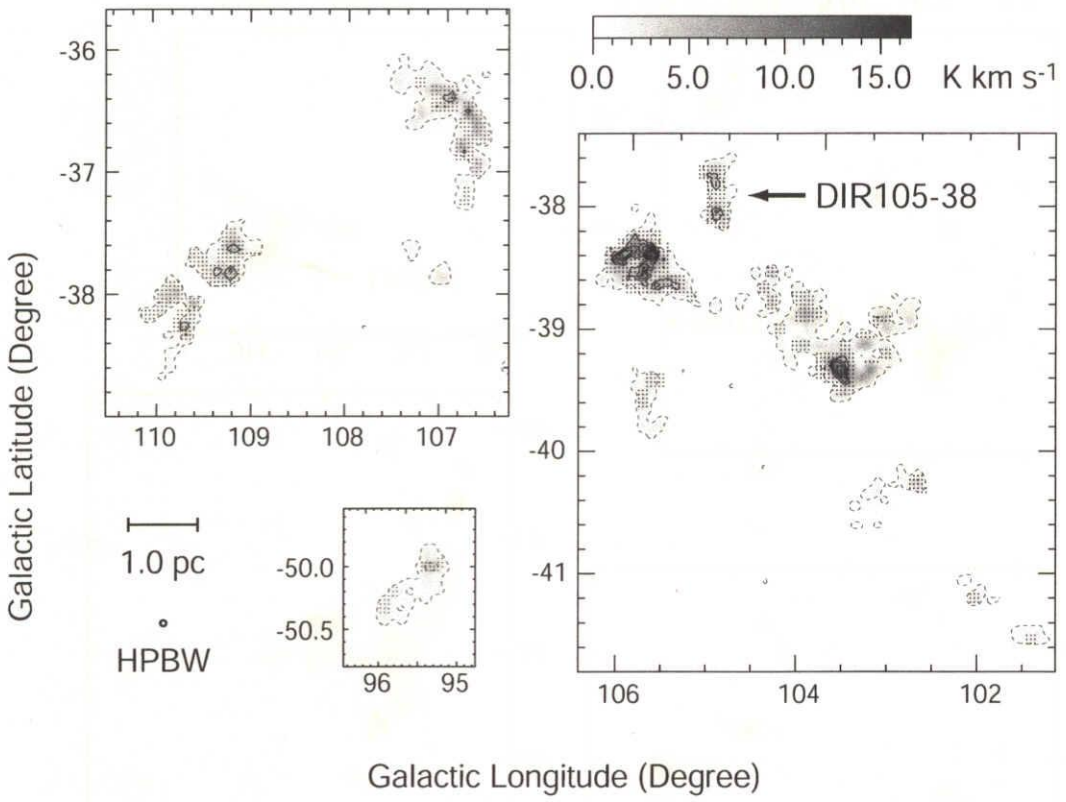

Figure 4–5. Total integrated intensity map of ^{13}CO (J = 1–0) shown in Galactic coordinates (bold lines). The lowest contour and the separation between contours are 0.3 K km s^{-1}. Gray scale shows the velocity integrated intensity map of ^{12}CO (J = 1–0). Dashed lines show the boundary of ^{12}CO clouds. Dots indicate the positions observed in ^{13}CO. The linear scale of all the figures are the same.

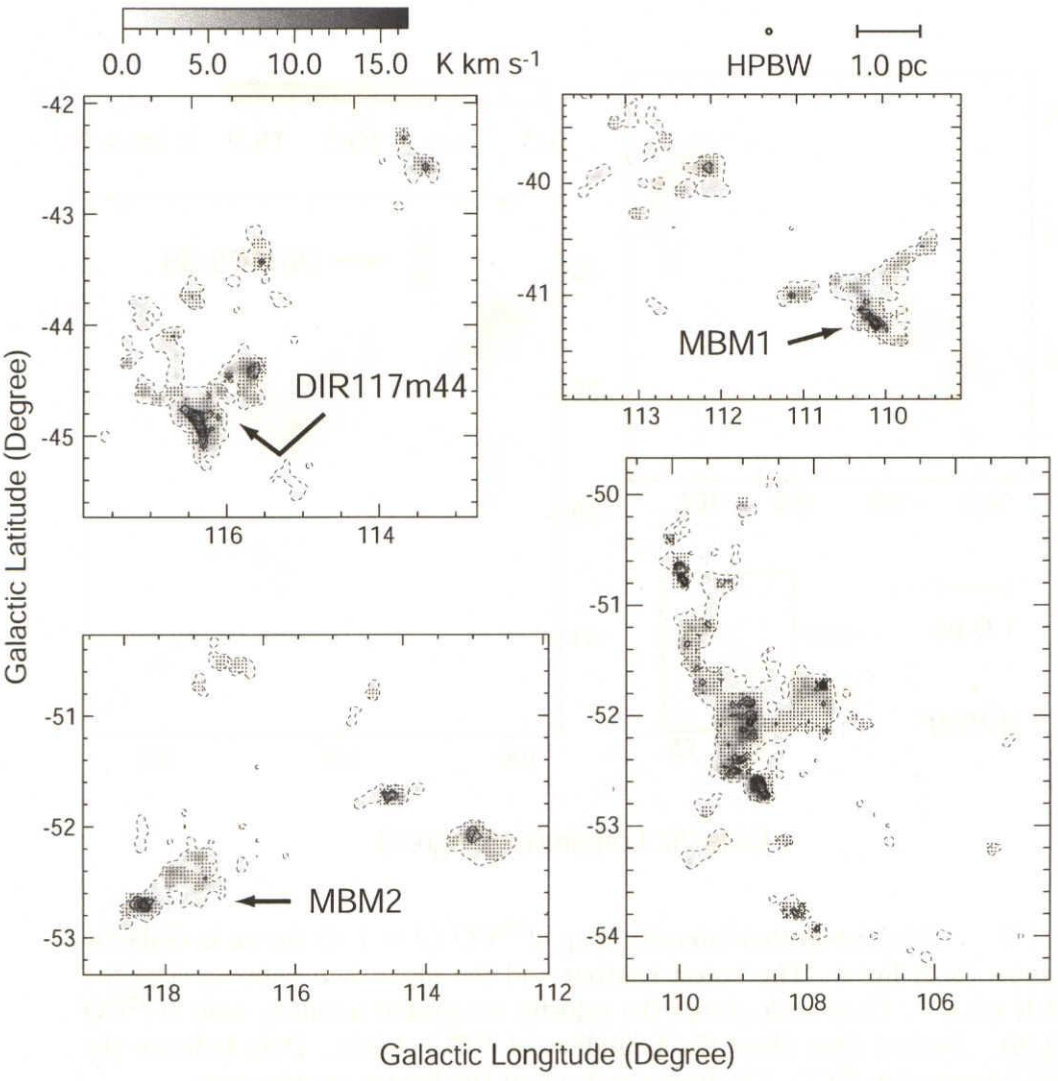

Figure 4–5. (Continued)

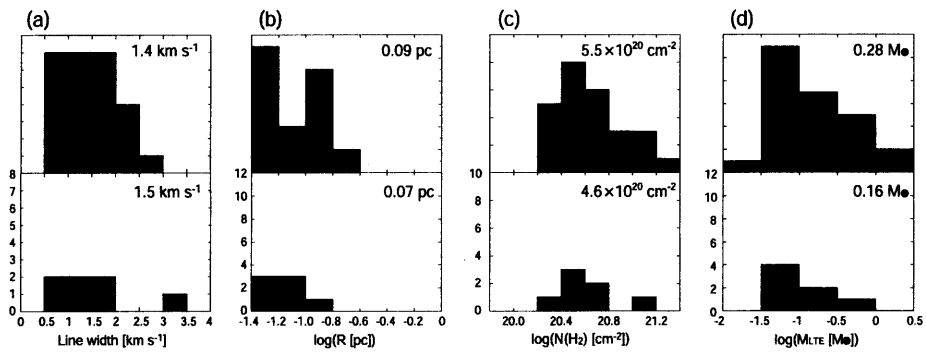

Figure 4–6. Histograms of (a) Line widht, (b) Radius, (c) Column density of molecular hydrogen and (d) LTE mass on the ^{13}CO clouds. The ^{13}CO clouds identified in the UC and SC are shown in the upper and lower histogram, respectively. The range and the interval of the histograms of (a), (b), and (c) are the same as Figure 4. The number in each panel is the average value.

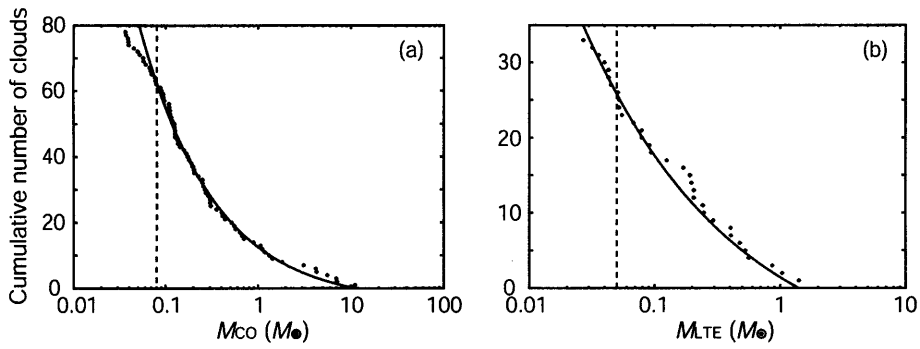

Figure 4–7. (a) Mass spectrum of the ^{12}CO clouds. The number of clouds, $N(<M_{CO})$, with mass grater than $M_{\rm CO}$ is plotted against $M_{\rm CO}$, along with the best-fitting power law (solid lines). The best fitting is expected as $N(\leq M_{\rm CO})$ $=17.33\times {M_{\rm CO}}^{-0.53}$ -4.78 for the mass range of $\geq$0.08 $M_{\odot}$ derived by using the maximum likelihood method (Crawford et al. 1970). (b) Same as (a), but for ^{13}CO clouds. The best fitting is expected as $N(\leq M_{\rm CO})$ $=12.54\times {M_{\rm LTE}}^{-0.36}-11.06$ for the mass range of $\geq$0.05 $M_{\odot}$.

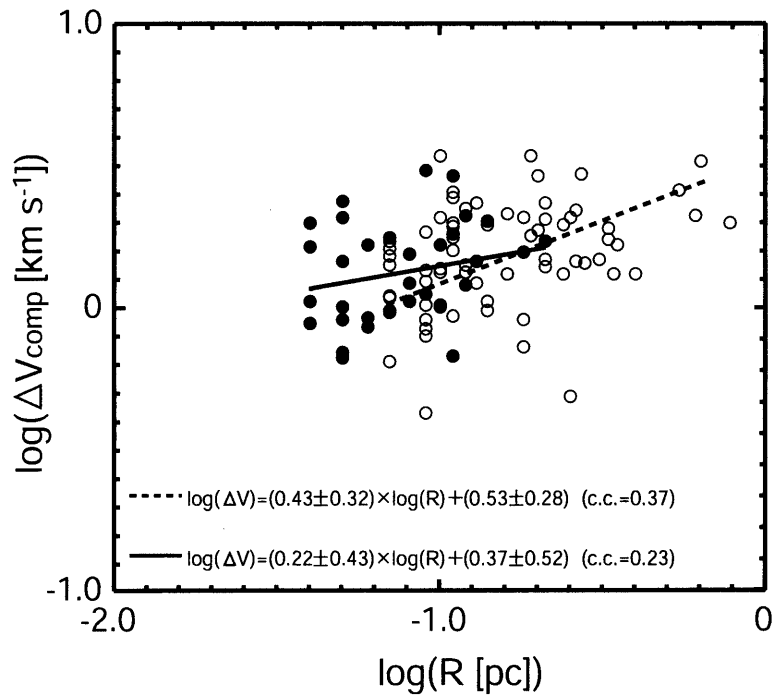

Figure 4–8. Plots of composite line width, $\Delta V_{\rm comp}$ versus radius of ^{13}CO clouds, R. The filled and open circles indicate the ^{13}CO clouds in present region and those in MBM 53, 54 and 55 complex, respectively. The solid and dashed line indicate the least-squares fit to these plots in present region and MBM 53, 54 and 55, respectively.

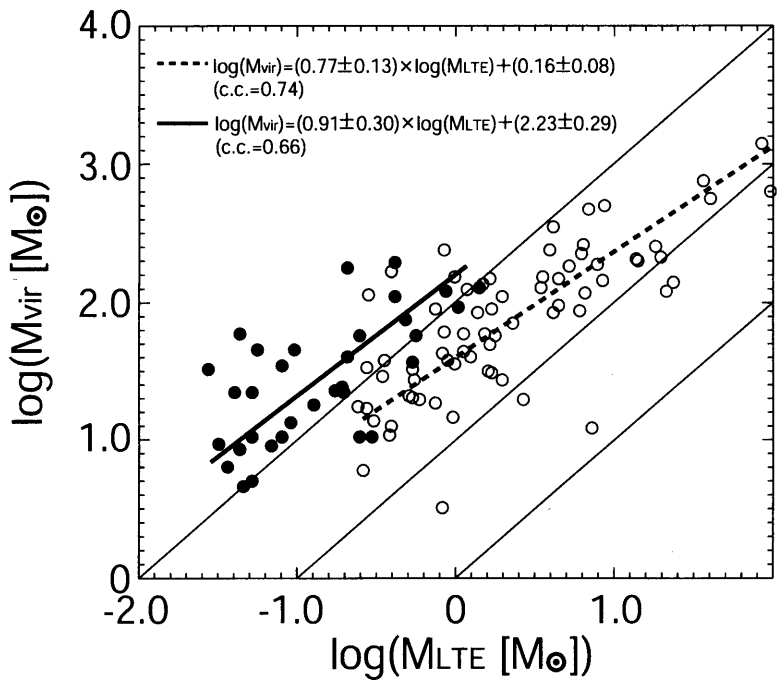

Figure 4–9. Plots of $M_{\rm vir}$ versus $M_{\rm LTE}$. The filled and open circles indicate the ^{13}CO cluods in present region and in MBM 53, 54, and 55 complex, respectively. The three thin solid lines represent $M_{\rm vir}=10^2\times M_{\rm LTE}$, $M_{\rm vir}=10\times M_{\rm LTE}$ and $M_{\rm vir}=M_{\rm LTE}$ from the top. The thick solid and dashed lines represent the least-squares fits to these plots in present region and those MBM 53, 54, and 55 complex, respectively.

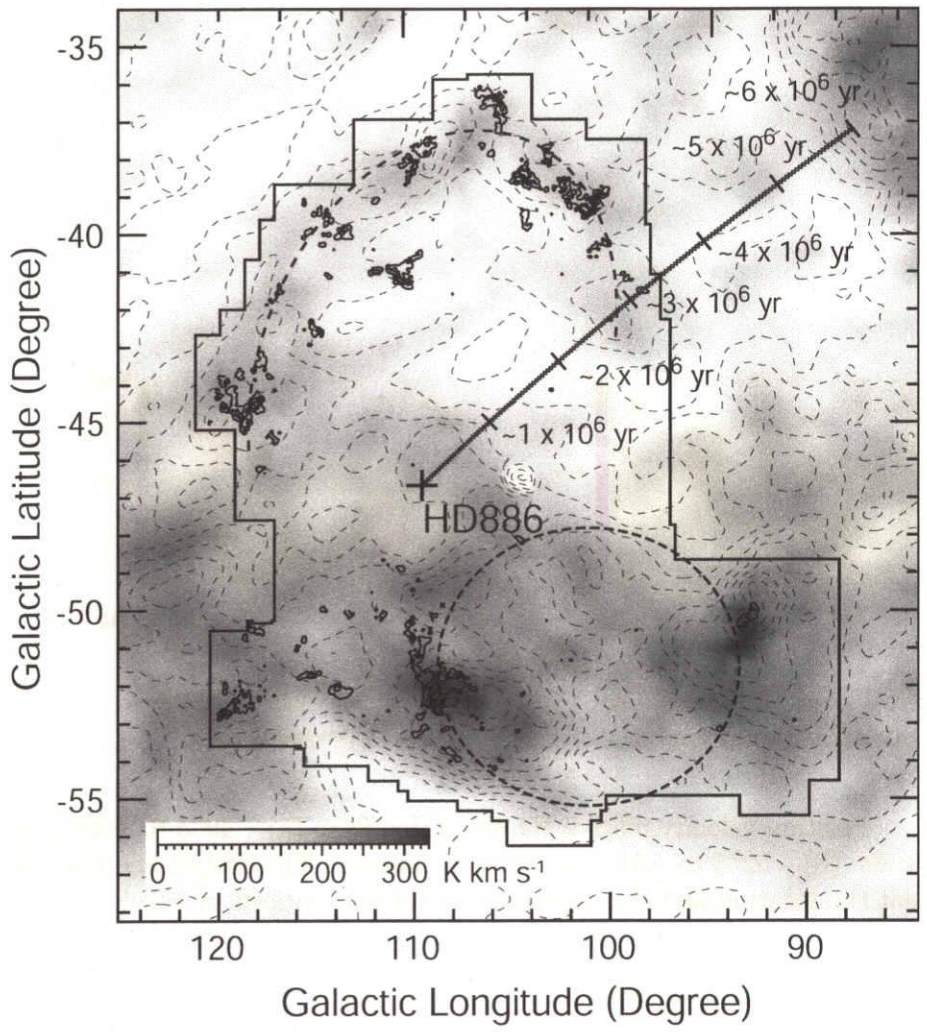

Figure 4–10. Total integrated intensity map of ^{12}CO ($J = 1$–0) superposed on that of H I. The solid contours represent the integrated intensity of ^{12}CO. The dashed thin contours and gray scale represent the integrated intensity of H I. The velocity coverage of H I is -16 to 0 km s^{-1}, corresponding to that of ^{12}CO. The lowest contour and the separation between contours of H I are 25 K km s^{-1} and those of CO are the same as Figure 1. The thick dashed contours represent the location of the expanding shells. The cross indicates the position of HD886. The path of the proper motion of HD886 is illustrated for the last $\sim 6{\times}10^6$ yr by the solid line.

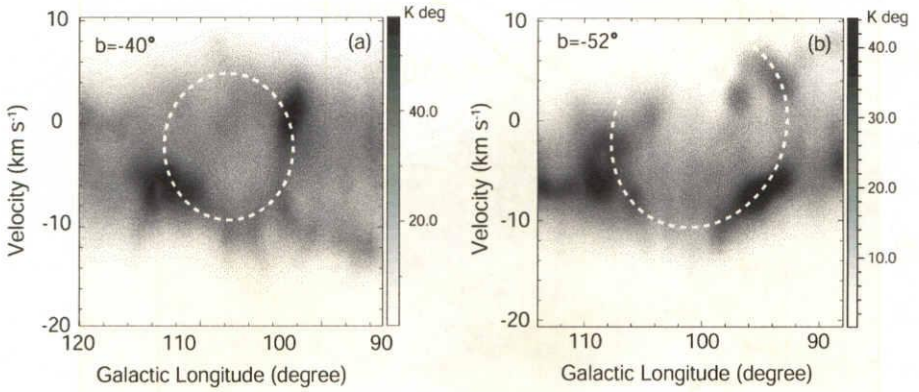

Figure 4–11. Position-velocity map of H I integrated from (a) $-40°.5$ to $-39°.5$ in Galactic latitude, (b) $-52°.5$ to $-51°.5$ in Galactic latitude. The dashed line in each panel represent the location and the extent of the H I holes drawn by hand.

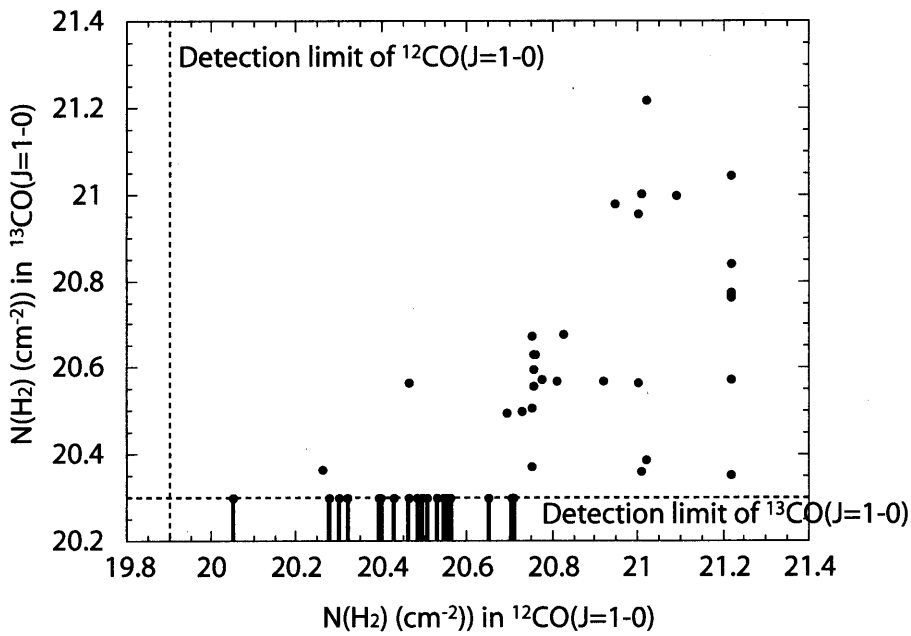

Figure 4–12. Plots of $N(H_2)$ derived from ^{12}CO versus it from ^{13}CO at the peak position of each cloud which were observed in ^{13}CO emission. The vertical and horizontal dashed lines indicate the detection limit of the observation of ^{12}CO and ^{13}CO, respectively.

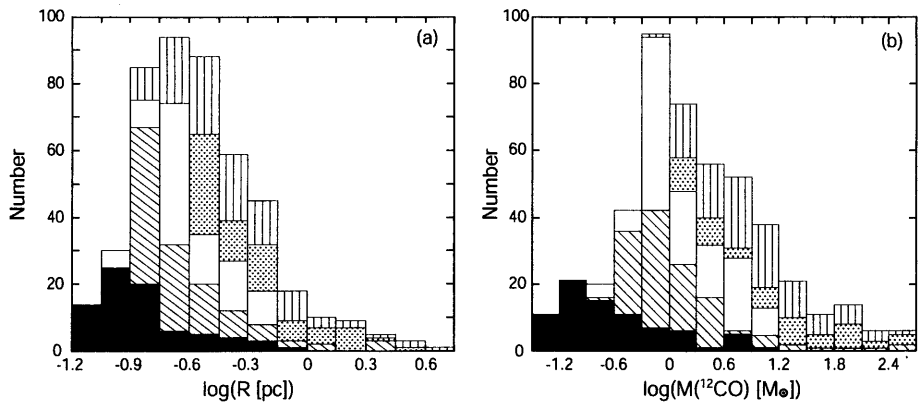

Figure 4–13. Histograms of (a) radii of ^{12}CO clouds and (b) mass of them. The dark shaded areas indicate the ^{12}CO clouds in present region. The vertical lined, the dotted lined, the light shaded and the diagonal lined areas indicate ^{12}CO clouds derived by Tachihara et al. (2001), Magnani et al. (1996), and in Chapter 2 and 3, respectively.

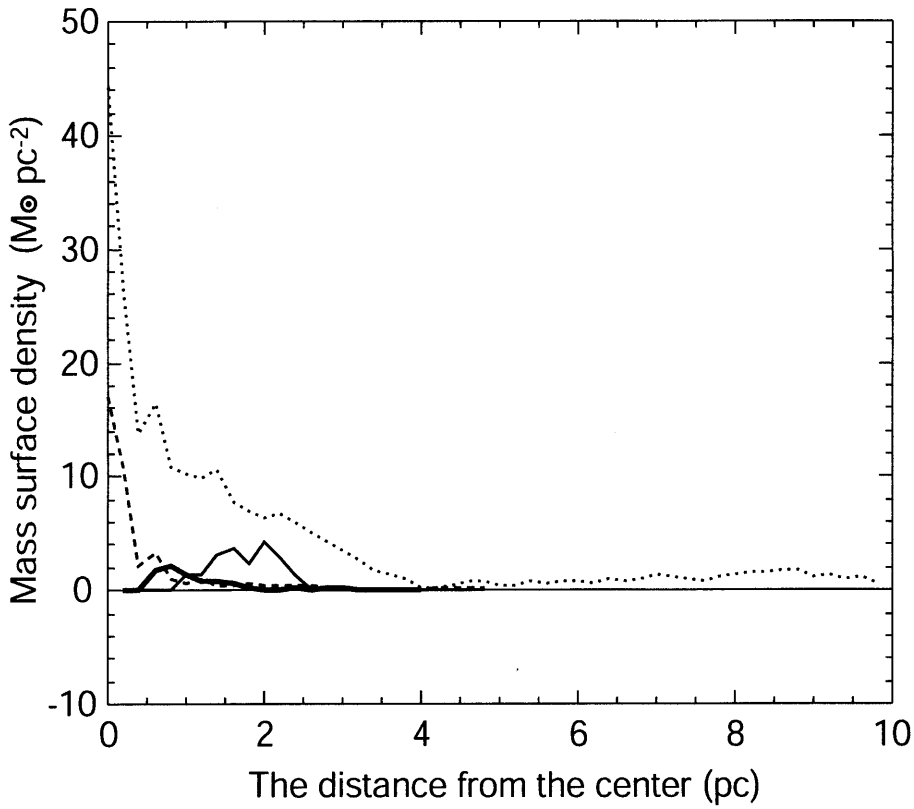

Figure 4–14. The radial distribution of mass surface density. The thick and thin lines indicate the regions around (113°, −51°) and (113°, −40°) in Galactic coordinates in present region, respectively. The dashed and dotted lines indicate the regions around HLCG92−35 and MBM 53 derived in Chapter 3, respectively.

Chapter 5

Summary of the Thesis

5.1 Summary of the Thesis

In this dissertation, the molecular clouds close to the Sun are studied on the basis of the CO observations in high Galactic latitude regions with 4m telescope, NANTEN, installed at Las Campanas Observatory, Chile. We carried out below three types of observations.

1. A survey for high Galactic latitude molecular clouds was carried out toward the 68 of the far-infrared-excess clouds derived by Reach et al. (1998) by using ^{12}CO (J=1–0) line. CO emission was detected from 32 infrared excess clouds. In 32 infrared excess clouds, we identified 137 CO clouds. Total mass of molecular clouds was estimated to be $\sim$250 $M_{\odot}$. The average radius, line width, peak temperature and mass of molecular clouds were 0.33 pc, 1.95 km s^{-1}, 2.9 K and 3.2 $M_{\odot}$, respectively. The CO detection rate was 47%. The CO detection rates for the cold and warm infrared excess cloud whose dust temperature is lower and higher than 17 K is 72% and 33%, respectively. This indicates that the cold clouds are well shielded from external UV radiation, resulting in a high CO abundance and a low temperature of the clouds. The infrared-excess clouds with no CO emission are most likely to be molecular hydrogen clouds because the temperature is similar to, or lower than, that of the surrounding H I gas. The molecular gas without CO emission seems to occupy more than 90% of the area of the infrared-excess clouds.

2. We have made a large-scale survey of molecular high galactic latitude clouds by using ^{12}CO (J=1–0), ^{13}CO (J=1–0), and C^{18}O (J=1–0) toward an H I filament which contains MBM 53, 54, and 55 complex with NANTEN telescope. The ^{12}CO

observation covered the entire H I filament with a grid spacing of 4′. The filament is found to consist of many small-sized molecular clouds and there identified 108 ^{12}CO clouds in the observed region. The total mass is estimated to be ∼1200 $M_{\odot}$. ^{13}CO observation toward the region of high ^{12}CO intensities was performed to measure the optical depth of molecular gas. We identified 70 ^{13}CO clouds and the radius and line width range from 0.07 to 0.74 pc and 0.7 to 4.7 km s^{-1}, respectively. The column density and $M_{\rm LTE}$ under the assumption of LTE range from 7.0×10^{20} cm^{-1} to 2.8×10^{21} cm^{-1} and 0.2 $M_{\odot}$ to 94.3 $M_{\odot}$, respectively. The mass spectra of ^{12}CO and ^{13}CO clouds are calculated to be $dN/dM \sim M^{-1.73\pm0.08}$ and $dN/dM \sim M^{-1.65\pm0.12}$, respectively. These spectrum indices are similar to that which has been derived in other regions. The Virial mass to $M_{\rm LTE}$ ratio is found to be $\gg$1 for all the clouds. Therefore, the clouds are not gravitationally bounded if we consider the mass traced only by ^{13}CO. There is no C^{18}O detection with a rms noise temperature of as low as ∼0.07 K. These imply that the star formation will not occur in the present ^{13}CO clouds in the near future. Comparison between the distributions of molecular gas and T Tauri stars suggests that there are at least two weak-line T Tauri stars around MBM 55. This indicates that there may be star formation ∼10^7 yr ago although the activity seemed to be quite low in spite of the large mass of the current molecular gas. We newly found a relatively massive cloud between MBM 53 and 54 around (l, b) ∼ (92°, 35°) of ∼330 $M_{\odot}$. The HLCG92−35 occupies a galactic western half of a circular-shaped H I gas in the H I filament, and the H I to CO mass ratio is estimated to be the largest in the observed region. The far-infrared excess over H I emission, which is a good index of the existence of molecular hydrogen, toward the HLCG92−35 is the largest in the observed region, implying that there is a good amount of molecular hydrogen in spite of the small optical depth of CO. These facts indicate that the HLCG92−35 is CO-forming one, which is younger than MBM clouds in terms of molecular cloud formation. The molecular gas is distributed preferentially along the western edge of the H I filament. The circular H I cloud that contains the HLCG92−35 seems to have a gradient of the evolutionary phase from east, younger, to west, evolved. These results suggest that the molecular gas may be formed by a compression of expanding H I shell.

3. Finally, we carried out large scale CO observations toward a loop-like structure in far infrared whose angular extent is about 20×20 degrees around (l, b) ∼ (109°, −45°) in Pegasus whose diameter corresponds to ∼26 pc at a distance of 100 pc, the same as that of a star HD886 (B2IV) at the center of the loop. We covered the loop-like structure in the ^{12}CO (J=1–0) emission at 4′–8′ grid spacing and in the ^{13}CO (J=1–0) emission at 2′ grid spacing for the ^{12}CO emitting regions.

The ^{12}CO distribution is found to consist of 78 small clumpy clouds whose mass ranges from 0.04 $M_{\odot}$ to 11 $M_{\odot}$. Interestingly, about 83% of the ^{12}CO clouds have very small masses less than 1.0 $M_{\odot}$. ^{13}CO observations revealed that 19 of the 78 ^{12}CO clouds show significant ^{13}CO emission. ^{13}CO emission was detected the region where the molecular column density of ^{12}CO clouds is greater than 5×10^{20} cm^{-2}, corresponding to Av of $\sim$1 mag. We find no indication of star formation in these clouds in IRAS Point Source Catalog and 2MASS Point Source Catalog. The very low mass clouds identified are unusual in the sense that they have very weak ^{12}CO Tpeak of 0.5 K–2.7 K and that they aggregate in a region of a few pc with no main massive clouds; contrarily to this, similar low mass clouds less than 1 $M_{\odot}$ are seen in the other regions previously observed including high Galactic latitude are all associated with more massive main clouds of $\sim$100 $M_{\odot}$. A comparison with a theoretical work on molecular cloud formation (Koyama & Inutsuka 2002) suggests that the very small clouds may have been formed in the shocked layer through the thermal instability. The star HD886 (B2IV) may be the source of the mechanical luminosity via stellar winds to create shocks, forming the loop-like structure where the very small clouds are embedded.

5.2 Remaining Questions and Future Prospects

In order to reveal the distribution and the physical properties of HLCs, we have carried out the HLCs survey toward far-infrared excess clouds and large scale structures. We got samples more than 300 ^{12}CO clouds and 100 ^{13}CO clouds and could discuss about their properties with statistical method. But the coverage of CO observations is still limited in the small area compared with the whole area of high Galactic latitude although many observations and some large surveys at high Galactic latitude have been performed. The datasets of far infrared and atomic hydrogen at high Galactic latitude have already existed. In order to reveal the whole distribution of HLCs with high spatial resolution, the more powerful system is essential. To compare whole CO data with them enables us to much reveal the physical properties of HLCs. In order to search for the past astronomical phenomena at high Galactic latitude, more widely observations are very important.

We detected a large number of very small clouds. As mentioned in 4.6.2, very small clouds have the size less than Jeans length of typical physical propaties of molecular clouds. Unfortunately, because of a detection of a few points, the internal structure of the very small clouds can not be elucidated. Our observations were

useful to identify many candidates just behind the formation of molecular cloud. To understand the detailed mechanism, the observations of higher spatial resolution and high transition lines for very small clouds are needed and these strucures shall be observed by larger telescopes such as NRO45m and ALMA in the future.

Our group is moving the 4m telescope from Las Campanas Observatory to Atacama desert. We will start the new observations in CO (J=1–0, 2–1, 3–2, 4–3, 7–6) and C I ($^3P_2$–$^3P_1$, $^3P_1$–$^3P_0$) by on the fly mapping mode. This is the special tool to search for the physical properties of molecular clouds and is expected to reveal the temperature and density of molecular clouds in more details.

Instruments of astronomical observations for all wave-length bands are evolved day by day. Spitzer Space Telescope (SST) has been already launched into space and has started the observations of infrared radiation. SST can provide the image from mid-infrared to far-infrared up to 160 μm at a grid spacing of lower than a few arc-min. Astro-F satellite will start the observation with near-infrared to far-infrared up to 200 μm in the near future and provide the image of those wavelength at a grid spacing of lower than 1′. Herschel space observatory will be launched in Feb 2007. The diameter is 3.5 m and it will perform photometry and spectroscopy in approximately the 57–670 μm range. It would be guessed that the pixel size is $\sim$10″ for the 200 μm and $\sim$40″ for the 670 μm. These results will change our intelligibility on dust properties. The grid separation of H I data of whole sky survey is 30′ for the beam width of 35′. ATCA (Australia Telescope Compact Array) can perform the high resolution observations of a few arc-min in H I. It is very important to understand the physical properties of H_2, dust, H I and the environment around the solar system. To achieve these, to compare CO data with these infrared and H I data at high Galactic latitude is needed.